Sheffield Hallam University

A Sheffield Hallam University thesis

A COMPUTER SIMULATION STUDY OF LIQUID CRYSTAL PHASE COEXISTENCE

STUART JAMES MILLS, BSc (Hons.), Grad. Inst. P., LRSC

A thesis submitted in partial fulfilment of the requirements

of Sheffield Hallam University for the degree of

Doctor of Philosophy

7 September, 1999
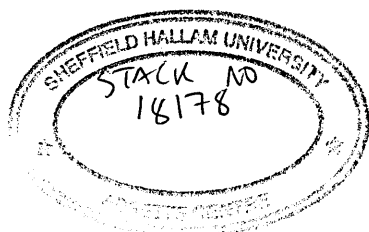
Abstract

Results are presented from a variety of molecular simulations of phase coexistence using the well established Gay-Berne (GB) liquid crystal model.

Firstly, the simulation of bulk phase coexistence using the Gibbs ensemble Monte Carlo technique is presented, both for one and two-component GB systems. The one-component results, using a novel parameterisation of the GB, show a rich phase behaviour, displaying both isotropic and nematic-vapour coexistence, in good comparison with previous studies. A method for arriving at the two-component parameterisation is then discussed, followed by a novel application of the Gibbs ensemble to the isotropic-nematic transition in two-component systems. Results in broad agreement with theoretical predictions, subject to a large finite size effect, are obtained.

Secondly, upon the basis of the one-component Gibbs results, results are presented from a series of molecular dynamics simulations of a free standing GB film in equilibrium with its own saturated vapour. The introduction of inhomogeneity is shown to induce a preferred molecular alignment in the nematic film perpendicular to the liquid-vapour interface. At slightly higher temperatures the nematic film is wet by the isotropic phase, displaying an intermediate ordering regime where the formation of short-lived nematic domains within the film is observed. This effect has been analysed using orientational correlation functions, and shown to result from a decoupling of the planar and perpendicular nematic ordering caused by the system inhomogeneity. A system-size analysis of this effect has also been undertaken, showing a definite increase in the range of decay of these orientational correlations with increasing system size.

To my family.

"In the context of eternity, all of this is meaningless."
Baruch Spinoza

Acknowledgments

Advanced Studies

As part of the course of study a number of postgraduate courses within the MRI at Sheffield Hallam University were attended. These included the topics Simulation and Phase Diagrams, as well as Polymers and Liquid Crystals, and Electronic and X-Ray Microscopy. A teaching course for postgraduate students was also attended.

A number of relevant external courses and conferences were participated in. These were, along with any work presented at them, in chronological order:

- CCP5 Spring School, Imperial College, London (March 1996)

- BLCS Annual Meeting, University of Central Lancashire, Preston (April 1996)

- CCP5 Annual Meeting, University of Bristol (September 1996)

- BLCS Annual Meeting, Southampton University (April 1997) - Poster Presentation - 'Computer Simulation of Fractionation in Bidisperse Liquid Crystals'

- Parallel Programming (MPI) Workshop, Edinburgh Parallel Computing Centre (August 1997)

- Structured Fluids Conference, Durham University (Sept 1997) - Poster Presentation - 'Computer Simulation of a Free Standing Liquid Crystal Film'

- Modelling of liquid crystals at interfaces - one day workshop, Sheffield Hallam University (Nov 1997)

- BLCS Annual Meeting, Leeds University (April 1998) - Oral Presentation - 'Computer Simulation of a Free Standing Liquid Crystal Film'

- International Liquid Crystal Conference 98, Strasbourg, France (July 1998) Poster Presentation - 'Computer Simulation of Fractionation in Bidisperse Liquid Crystals'

The following publication has also arisen as part of this work

- S. J. Mills, C. M. Care, M. P. Neal and D. J. Cleaver *'Computer Simulation of an unconfined liquid crystal film' Phys. Rev. E.* **58**, 3284.

Contents

Chapter 1

Introduction

Liquid crystalline phenomena are highly significant in a range of areas in the physical and biological sciences. Ranging from such obvious technological applications as the twisted nematic display, and the wide-spread use of surfactants in the cleaning industry, through to the importance of self-assembly in a large number of biological processes, mesogenic behaviour is clearly a worthy topic of investigation.

However, despite having been under investigation since their discovery more than 100 years ago [1], there is still much which is not known about the underlying physics [2, 3] behind many liquid crystalline effects. In the last 30 years or so there has been considerable experimental characterisation of various liquid crystals. This has been relatively successful in determining the underlying structures of the various liquid crystalline phases, and in locating the transitions and phase diagrams which characterise such systems [4]. It is by systematic investigation of these that the viability of new liquid crystals for various applications is tested, and also, occasionally, novel behaviour is uncovered opening up the possibility of new applications.

That said, it is important to realise that in the complicated statistical mechanical domain of phase transitions, experimental techniques can sometimes be of limited success in revealing the driving forces behind various phenomena. Also, the assumptions needed for theoretical treatments of these effects can mean that they are too far removed from the real situation to provide useful information. It is here that computer simulation [5, 6] can come into its own - essentially lying in between the realms of theory and experiment, simulation can be of great use in predicting trends which are difficult to access using the aforementioned techniques.

1.1 Aims

To date, the major application of thermotropic liquid crystals has been in the liquid crystal display (LCD), which takes advantage of the anisotropic optical and electrical properties of these molecules in low powered switching devices. In these, the use of mixtures of different liquid crystal compounds greatly improves the operational temperature range. Also of major importance is the pinning of the molecules at the device walls, since this affects the stable states available to the device and, to an extent, its power consumption.

The work described in this thesis relates to computer simulations performed with the aim of promoting greater understanding of these two aspects, namely polydispersity and interfacial symmetry breaking, and their effects upon phase behaviour. Specifically, attention has been focussed on the phase coexistence of a much studied liquid crystal model, the Gay-Berne [7], in a novel parameterisation with a relatively small

shape anisotropy. Initial simulations of the bulk monodisperse system indicated a potentially rich behaviour, and two different perturbations from this were therefore considered. Firstly, a relatively similar but different particle was introduced, making a bidisperse system whose behaviour around the isotropic-nematic transition was examined. Secondly, the effect of symmetry breaking upon the monodisperse coexistence was looked at, by direct simulation of an interfacial system.

The study of the isotropic-nematic transition for the bidisperse system was conducted mainly with a theoretical aim, that of observing fractionation, ie. preferential existence of one species in the ordered phase in the coexistence region, since this provides a useful check of the mean-field theories which have predicted this effect [8]. Its successful observation would also mean a significant step forward in applying the Gibbs ensemble method to dense anisotropic systems. To date this effect has only been seen in markedly more bidisperse simulations [9], where the difference between the species types is much greater.

Although the interfacial system considered did not include any interacting walls, only liquid vapour interfaces, it was considered that this would provide an insight into the effect of the interparticle interactions upon interfacial alignment, being a reference system for the more complicated confined system. Explicitly, the aim was to see qualitatively realistic behaviour, with perpendicular (homeotropic) alignment at the interfaces and nematic wetting (surface ordering). This was also considered to be of theoretical as well as technological interest, being an example of complex behaviour observed with a relatively simple model, and exhibiting effects on many different length scales.

3

1.2　Summary of Thesis

Aside from this introduction, the thesis is organised as follows.

In Chapter Two, an introduction to liquid crystals is given, concentrating on the types of molecules which display this intriguing phenomenon and the structures of the phases formed. Chapter Three considers previous attempts to model liquid crystalline behaviour, using a variety of theoretical and simulation techniques, together with a brief description of the simulation methods used both in the previous studies and later on in this body of work. Attention is focussed on work which is relevant to the results presented here, although some effort has been made to give a wider consideration of experimental liquid crystals.

Chapter Four consists of the results of a series of Gibbs ensemble simulations of bulk liquid crystal coexistence, both for mono- and bi-disperse systems, together with descriptions of the parameterisations and the regions of the phase diagram investigated. Based upon some of these coexistence results, simulations of a variety of different sized interfacial systems are presented in Chapter Five, using both standard Monte Carlo and molecular dynamics methods. As well as the usual considerations of the phase diagram, in depth analysis of the orientational correlations and their dependence upon system size is carried out, and comparisons are made with the bulk behaviour presented in Chapter Four.

Finally the implications of this work are considered in Chapter Six, from theoretical, experimental and simulation angles. The success of the program of work is assessed and suggestions are presented for future investigations.

Chapter 2

Experimental Liquid Crystal

Behaviour

In this chapter a brief introduction to the physical properties of liquid crystals is given. Firstly the bulk phase behaviour is described, including details of the microscopic structure of the main liquid crystalline phases. This is followed by a short discussion of the effect of bidispersity upon this phase behaviour (ie the properties and importance of liquid crystal mixtures) and finally the implications of interfaces are considered, both for confined and unconfined materials.

2.1 Bulk Liquid Crystals

Materials which exhibit intermediate phases between the isotropic liquid and crystalline solid states are termed *mesogens*. Mesogenic materials have been reported and investigated since their discovery in the late 19th century [1]. Their unique

properties have been exploited in many devices, notably in condensed matter systems such as liquid crystal displays (LCDs), as well as applications in data storage. However, many of their properties and the underlying physics which gives rise to them are still not fully understood, and there remains scope for improvement in their utilisation.

Mesogenic materials can be classified into two distinct categories [3]; disordered crystal mesophases and ordered fluid mesophases. The former have their constituent molecules fixed at lattice sites but with orientational freedom, and are termed plastic crystals because they deform easily under stress. The latter exhibit long range orientational order with or without some long range translational order and are termed liquid crystals (LCs). They are generally classified in two categories; thermotropic and lyotropic. Thermotropic LCs form different mesophases solely upon variation in temperature, whereas lyotropic LCs do so by changes in concentration as well.

Like other states of matter, thermotropic mesophases are indefinitely stable at defined temperatures and pressures. They are split into two groups as follows. One in which the molecules have rod-like shapes - called *calamitic liquid crystals* - the first type discovered, and the other where they have disk-like shapes - called *discotic liquid crystals* - which were discovered relatively recently [10]. The familiar phases of liquid and solid are represented below (Fig 2.1) for calamitic liquid crystals.

As can be seen, in the isotropic liquid the molecules are completely disordered, whereas in the crystalline solid their long axes are all parallel and they are confined to a regular lattice structure. The intermediate *mesogenic* phases are characterised by varying degrees of orientational and positional order.

Isotropic
Liquid

Crystalline
Solid
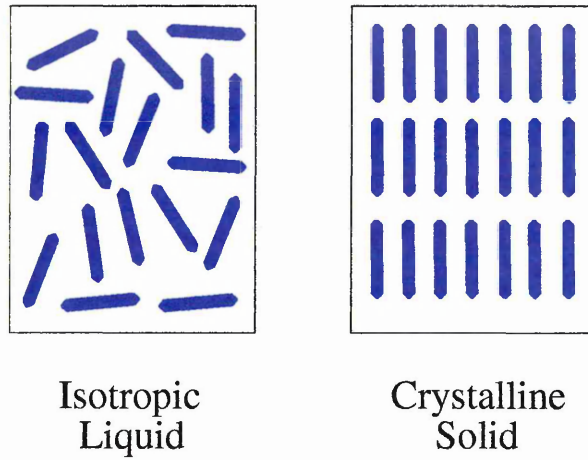
Figure 2.1: Liquid and solid schematics

Since this work is primarily concerned with thermotropic calamitics, a brief description of only these phases will be given. They can be split into two main types; nematic phases where the molecules are orientationally ordered so that their long axes are preferentially aligned along some direction; this being called the director, and the more ordered smectic phases in which the molecules in addition display some sort of layered structure. Brief schematics of these phases are given (Fig 2.2).

If the liquid crystalline molecules are chiral then the nematic director will adopt a twist throughout the system, in what is called the chiral nematic phase. The length scale of the twist is often comparable to the wavelength of visible light, and it is these substances that are used in liquid crystal thermometers; the twist length changes with temperature and thus causes a different optical colouring to be observed when light is reflected by it. However, chiral systems are not of importance in this thesis.

Various sorts of smectic phases exist; their classification being dependent upon the degree of ordering within the layers and the presence of any tilt with respect to the
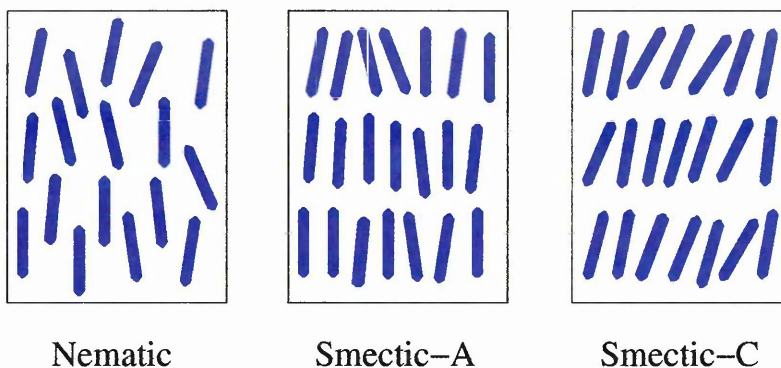
Figure 2.2: Liquid crystal schematics

layer normal. The simplest smectic phase, where each layer is a two dimensional liquid and there are no correlations between the layers is known as the smectic-A phase. The tilted analogue of this is the smectic-C phase, the nematic director being tilted with respect to the smectic layer normal. Both of these phases are shown above (Fig 2.2).

In the hexatic smectic-B phase there is long range order within the layers, the molecules being distributed locally on a triangular lattice; however the number of defects is such that the positional order does not extend over distances larger than a few 100Å, but the bond order extends over macroscopic distances [2]. However there are no inter-layer correlations, and hence the phase keeps its liquid character.

A number of different molecules have been shown to display calamitic LC phases. All of these share a geometrical anisotropy in shape. A schematic showing the key constituents for a mesogenic compound is presented below (Fig 2.3).

From the vast amount of experimental data available, the main parts seem to be a rigid core, which generally consists of two cyclic compounds, A and B, possibly

8
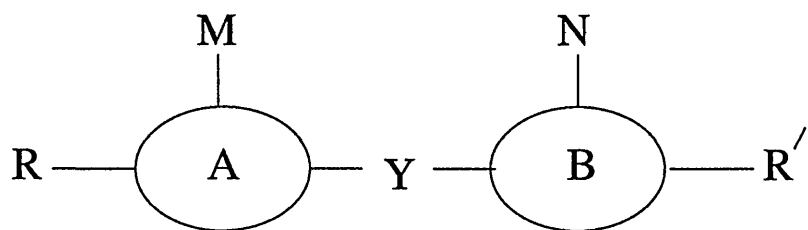
Figure 2.3: A generic mesogenic template

linked by a group Y which maintains the linear nature of the core. The end groups, R and R', are usually straight alkyl or alkyloxy chains and serve to introduce some degree of flexibility into the molecule; however one terminal unit is often a small polar substituent. The presence of lateral substituents, M and N, has been found to subtly alter the phase behaviour of many mesogenic materials, and can be of great use in optimising material performance. Two classic mesogenic compounds are p-azoxyanisole (PAA) and M-(p-methoxybenylidene)- p-butylaniline (MBBA), having the formulae shown (Figs 2.4,2.5).
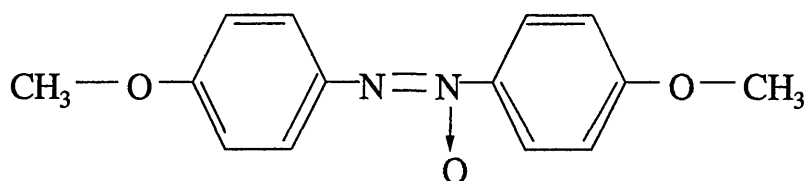
Figure 2.4: PAA
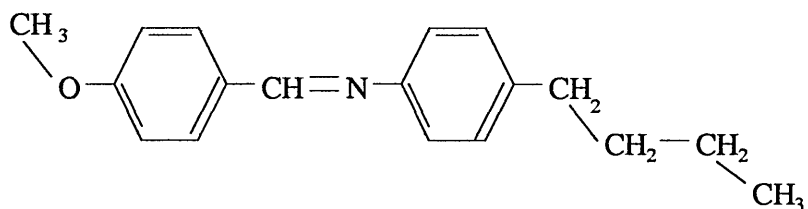
Figure 2.5: MBBA

These two historical examples have been extensively studied and there is a wide

9

R	K		S_A		N		I
C_5H_{11}	•	24.0	–		•	35.0	•
C_6H_{13}	•	14.5	–		•	29.0	•
C_7H_{15}	•	30.0	–		•	43.0	•
C_8H_{17}	•	21.5	•	33.5	•	40.5	•
C_9H_{19}	•	42.0	•	48.0	•	49.5	•
$C_{10}H_{21}$	•	44.0	•	50.5	–		•

Table 2.1: Cyanobiphenyl transition temperatures (°C)

variety of information in the literature detailing the different aspects of liquid crystalline behaviour they display. Just to give a rough idea of mesogenic dimensions, PAA is approximately 20Å long by 5Å wide, although obviously other mesogenic compounds can vary significantly from this. Unfortunately, PAA only displays a nematic phase at high temperatures and MBBA is not chemically stable, making them both rather unsuitable for modern day applications. It was the search for stable room temperature mesogens that led to the discovery of the cyanobiphenyls, a ubiquitous group of liquid crystals that were first synthesised in 1972. Consisting of a biphenyl core with a cyano substituent, and an aliphatic chain of variable length as the two end groups (Fig 2.6), these molecules were the first commercially viable nematic liquid crystals for use in display devices, combining low melting points with relatively high isotropic-nematic transition temperatures, T_{IN} (Tab 2.1).
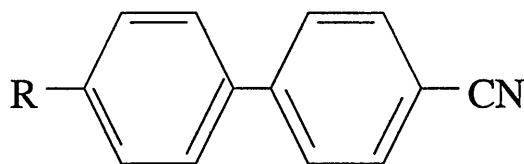
Figure 2.6: Generic structure for the cyanobiphenyls

It is clear that upon increasing the length of the alkyl chain the transition temper-

atures tend to increase, as the additional anisotropy leads to more order at a given temperature. The noticeable two step behaviour, with transition temperatures going alternatively down slightly and then up significantly, up to $R=C_9H_{19}$, is due to the well known odd-even effect. This arises because each successive addition of an alkyl chain will affect the anisotropy of the molecule in one of two different ways, depending on whether it is a linear addition or at an angle. As can be seen this happens in an alternate manner (Fig 2.7).
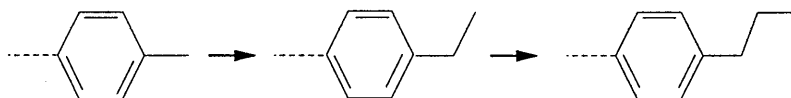
Figure 2.7: The odd-even effect

Upon further increasing the molecular length, the smectic phase is progressively stabilised, until eventually no nematic phase is observed (10CB). These molecules still find use today in digital watches and calculators, but generally in a mixture with other compounds (both mesogenic and non-mesogenic) which has been selected to give optimum device performance. It is on these mixtures that attention will now be focussed.

2.2 Liquid Crystal Mixtures

Perhaps the most relevant application of polydisperse liquid crystals is the widely practised use of mixtures in nematic devices, where the presence of two (or more) different molecule lengths delays the onset of smectic ordering, as would be expected intuitively [2]. This results in a nematic phase with a much larger stable temperature

11

range, increasing the utility of such devices. The importance of this is obvious when it is considered that the vast majority of LCDs use twisted nematic cells.

However, polydispersity not only affects the relative stability of the phases, it also opens up the possibility of novel phases, and coexistence between them. A transition between two uniaxial nematic phases has been observed experimentally [11] for a mixture of two relatively similar nematogens. Although no nematic-nematic coexistence has been observed for these molecules, it has been observed in mixtures of polymeric and low molecular weight nematogens [12], and also in mixtures of rod-like and disk-like nematogens [13].

Certainly, any improvement in the understanding of what drives these effects in liquid crystal mixtures would be of importance, and it is the aim of this work to make some progress in this direction. A simple generic phase diagram is shown (Fig 2.8), which illustrates the important effects of extended nematic range and phase coexistence (I,N and S represent isotropic, nematic and smectic phases respectively).
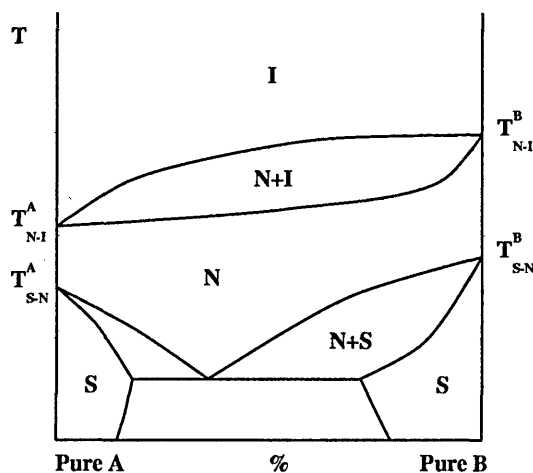
Figure 2.8: Binary mixture phase diagram

A number of other complicated phase behaviours have been predicted theoretically;

although more will be said of this in the next section, a practical application is worthy of mention here. The order parameters of the individual components of the mixture may differ appreciably [14] in binary nematics, which could prove useful in the design of dye displays. The dye molecules could be chosen to have a high anisotropy, and hence a high order parameter, one which would normally be indicative of a smectic phase for a one-component system. However the bi-dispersity will destabilise the smectic ordering and keep the system nematic, enabling a much better contrast ratio to be obtained due to the high order parameter [3].

Perhaps a better illustration of the degree of complexity bidispersity can confer on phase behaviour is given by the phase diagram shown (Fig 2.9), for a binary mixture of octyloxyphenyl-nitrobenzyloxy benzoate (DB_8ONO_2) and decycloxyphenyl-nitrobenzoyloxy benzoate ($DB_{10}ONO_2$) [15] (Fig 2.9). X denotes the mole percent of $DB_{10}ONO_2$.
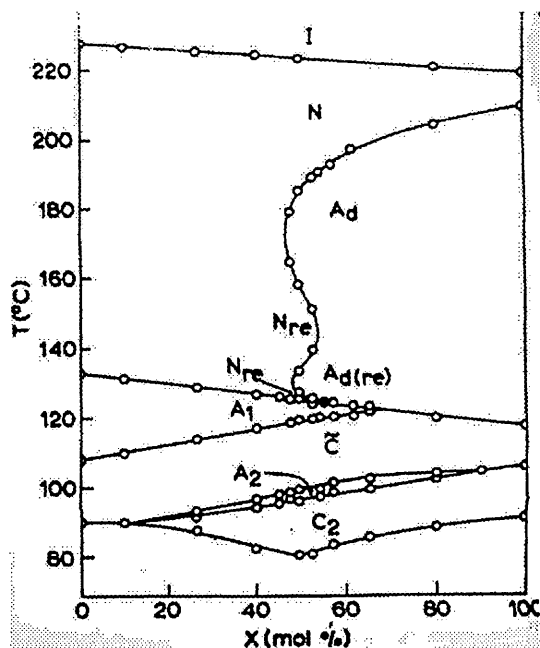
Figure 2.9: Phase diagram [15] - see text for details

13

A number of different phases are present in this diagram, including isotropic (I), nematic (N), smectic A monolayer (A_1), smectic A bilayer (A_2), smectic A partial bilayer (A_d), reentrant phases (re), tilted bilayer (C_2) and a fluid antiphase ($\tilde{C}$). The fact that both of these molecules are highly polar helps to explain to some degree the richness of the phase diagram, but it does still give an idea of the plethora of phases available in bidisperse systems.

2.3 Confined Liquid Crystals

Moving on from considerations of bulk systems, the single most important application of mesogens to date has been in the liquid crystal display (LCD). This makes use of the electric and optical anisotropic properties of liquid crystals to provide exceptionally low power displays. A very simple schematic of a twisted nematic device is shown (Fig 2.10).
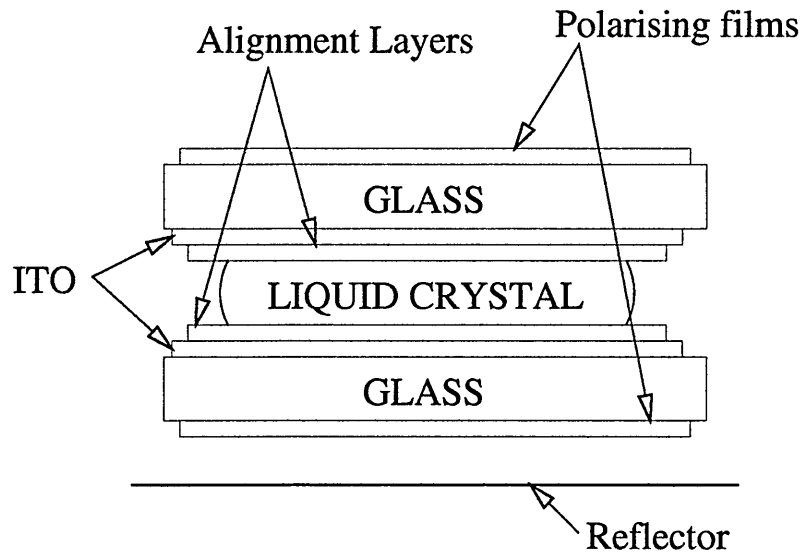
Figure 2.10: LCD schematic [4]

Light enters the cell from the top and is plane polarised by the uppermost film, before passing straight through the transparent glass, indium tin oxide (ITO) and alignment layers. Switching essentially occurs within the nematic liquid crystalline material. The alignment layers are set up during cell fabrication so that the topmost nematic layer is parallel to the incoming plane polarised light, and the bottom one is perpendicular. This forces the nematogen to adopt a twist across the cell and this twist rotates the polarisation vector of the light, allowing it to pass through the bottom plane polariser which is at right angles to the top one. The light is then reflected back through the cell and the display thus appears light. However, when an electric field is applied across the liquid crystal (delivered through the ITO) the liquid crystalline molecules align themselves parallel to it, and thus no longer twist the incoming light so that it can pass through the bottom polariser. The display therefore appears dark. The actual orientations of the molecules within these two states are shown below (2.11). Note - in real devices the cells are much thicker than the few molecular lengths shown here.

Off State (V=0)   On State (V≠0)
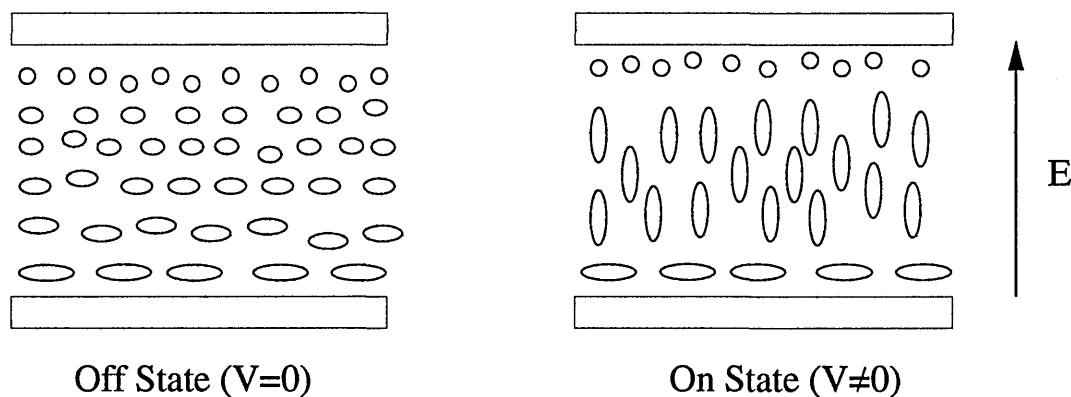
Figure 2.11: Orientations in the two states [4]

The liquid crystalline material in a device needs to possess a number of different properties to ensure its optimum operation. As mentioned earlier, a wide temper-

ature range of nematic stability is necessary for the device to be practical, as is a strong surface anchoring, which keeps the nematic in its twisted state. However, matters are complicated further by considerations of switching - a low viscosity and a large dielectric anisotropy will reduce the switching time and required voltage, in addition to which a high optical anisotropy is needed to improve the contrast of the device.

In general, mixtures of liquid crystalline compounds are used to achieve the desired properties. The optimisation of these mixtures to produce ever improving displays is an ongoing process, and it is obvious that comprehensive simulation of such a device is beyond current computational power. The role of simulation (and theory) instead is to look at various effects individually, and try to build up a picture of how they vary with certain trends, such as changing the length of the mesogen, or the strength of its interactions.

Clearly in a device such as the one above, the anchoring of the liquid crystal molecules to the alignment layer will be of major importance in ensuring successful operation. Ideally the molecules will need to be tightly anchored in the off state, to ensure the stability of the twist with temperature, shock etc. Before reviewing previous experimental studies of substrate-mesogen interfaces, a brief account of the theoretical distinction between weak and strong anchoring will be given.

Fig 2.12 shows how the angle the local nematic director makes with the anchoring direction at the wall, θ, varies across half of a typical device cell, where y is the distance from the wall. The bulk gradient represents the twist across the device; the free energy of the system is minimised if this gradient is constant, however in the
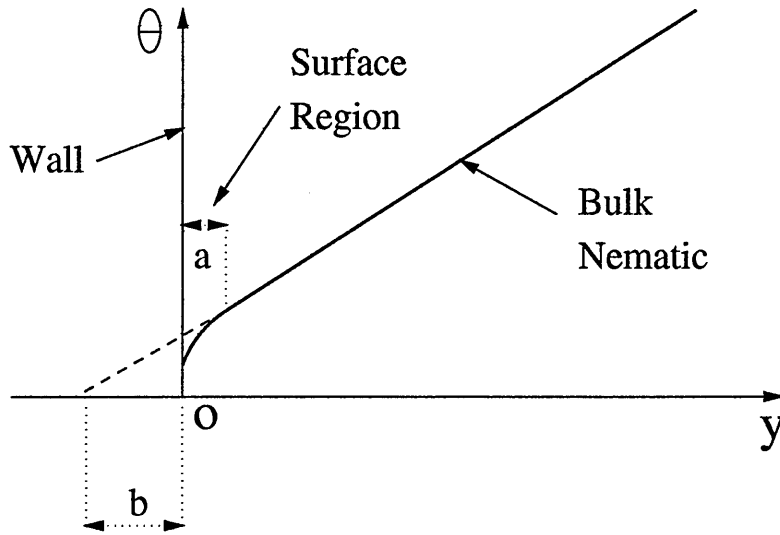
Figure 2.12: Anchoring of director at wall [2]

surface region considerations of anchoring energy minimisation lead to a deviation from this constant behaviour. In this region of molecular thickness a, the twist $\frac{\delta\theta}{\delta y}$ is dependent upon detailed molecular properties. The extrapolation length, b, is dependent upon the strength of the alignment and can be approximately estimated using

$$b = \frac{K_2}{A}$$

where A is a positive constant representing the anchoring strength and having dimensions of the surface tension, and K_2 is the bulk twist elastic constant; the stronger it is, the less the bulk nematic favours a twist deformation. Both of these quantities are dependent upon the materials used, and in practice there are two possible types of anchoring:

- *Strong anchoring*, where the nematic-substrate interaction is comparable to

17

the nematic-nematic, and the extrapolation length b is comparable to the molecular dimension a.

- *Weak anchoring*, where the nematic-substrate interaction is far weaker than the nematic-nematic, and the extrapolation length b may be much larger than the molecular dimension a.

Recent scanning tunnelling microscopy (STM) studies have probably been the most successful in showing the high degree of order promoted by the substrate interaction. For example, the interface between a droplet of liquid crystalline material, 8-cyanobiphenyl (8CB) and a planar substrate (cleaved pyrolytic graphite) has been shown to display a first adsorbed layer of mesogenic molecules forming a highly ordered, possibly 2-d crystal, structure stretching for thousands of angstroms [16]. The effect of changes in the bulk behaviour have also been studied, indicating that they can drastically change the surface region order. Specifically, the crystal structure of the adsorbed monolayer mentioned above is found to be destroyed at the bulk nematic-smectic transition [17].

Second harmonic generation (SHG) studies of similar systems have confirmed the existence of surface ordering but produced slightly contradictory results in that they indicate a tilted rather than planar ordering of the first monolayer at the substrate [18]. This could be attributed to the different substrate used in SHG (mica rather than graphite) however it should be noted that recent simulation results suggest the invasive nature of STM may promote a planar structure [19]. SHG studies have also observed phase transitions in confined systems - when ethylene glycol is added to 5OCB adsorbed on mica it is preferentially adsorbed at the substrate

and a concentration-dependent anchoring transition occurs, appearing to be surface driven [20].

Of marked importance in the consideration of interfacial phenomena and their effect upon optimum device performance is the interaction of different length scales - specifically the link between microscopic substrate anchoring and the macroscopic film (device) behaviour [21]. This can lead to some problems experimentally, since it is difficult to access the transition region across which this anchoring is conferred. Theoretical models, of which more will be said in the next section, have attempted to address this correlation, but only with limited success. Computer simulation is an ideal technique with which to study this effect, but unfortunately the large length-scales involved are at the limits of tractability. In an attempt to remedy this, a simpler reference system would make a far better target for the simulator. Aside from considerations of mesoscopic models, a suitable choice is an unconfined liquid crystal film, which still contains the symmetry breaking element which should induce some form of inhomogeneity, yet does not involve a complicated wall - molecule interaction. A brief survey of the experimental work in this area will be given as a preface to the theoretical and simulation review in the next chapter.

2.4 Unconfined Liquid Crystals

In a similar manner to confined liquid crystal films (such as in LCD's), the break in symmetry at the free surface of a liquid crystalline material can induce a preferred alignment and/or a change in the degree of ordering.

One of the first experimental investigations of free nematic surfaces looked at surface alignment using a light reflection technique. It was found that p-azoxyanisole (PAA) favours planar ordering, whereas 4-methoxybenylidene-4'-butylaniline (MBBA) prefers an oblique state, the surface director lying at an angle of 75 degrees from the surface [22]. Subsequent work confirmed this for PAA [23] and showed that MBBA in fact undergoes a transition from tilted to perpendicular (homeotropic) alignment at a temperature slightly below the triple point [24]. Studies of another common class of liquid crystal molecule, the cyanobiphenyls (CB), showed perpendicular alignment at the free surfaces of 5, 6, 7, 8 CB [25]. This type of behaviour was also seen for a closely related compound, 8-oxy-cyanobiphenyl (8OCB) [26].

Also of consideration is surface induced (dis)ordering, or *wetting* behaviour. Interfaces which induce enhanced ordering are said to display nematic wetting, whereas those which are surface disordering are termed isotropic wetting. Virtually all real confined systems show nematic wetting, but at the free surface, disordering is intuitively more likely to be possible (because of the lack of an order enhancing wall - substrate interaction).

A variety of experimental studies have established conclusively that orientationally ordered states, and in certain materials even density modulations, develop in the vicinity of the free surface [3]. Reflection ellipsometry work on the cyanobiphenyls [25] has shown nematic wetting of the isotropic free surface, with this wetting changing from partial to complete upon increasing the molecule length (5CB partial; 6,7,8 CB complete). This is in good agreement with theoretical predictions of increased nematic wetting ability upon increase of the degree of anisotropy (see Chapter 3).

Furthermore a study of the surface tension behaviour for these systems [27] showed the expected trend for nematic wetting, which will be discussed at a later point.

More recently, prewetting transitions and a prewetting critical point have been observed at the free surfaces of various benzoic acid oxyphenylester derivatives [28]. These ellipsometric studies have all shown enhanced orientational order at the surfaces.

The surface tension, γ, of an interface is commonly determined by measuring the exact shape of a drop of liquid crystalline material (several methods are applicable), and using a simple relationship between this shape, the density difference between the drop and its surrounding fluid, and γ [29]. The surface tension is important in that it gives an indication of the rigidity of the interfaces, and normally shows a certain qualitative behaviour with temperature depending upon the type of wetting displayed at the surface.

Generally speaking, the surface tension of an isotropic liquid with its own vapour shows a negative gradient with increasing temperature, decaying to zero at the critical temperature, where liquid-vapour coexistence ceases. In terms of decreasing temperature, if the isotropic liquid undergoes a transition to a nematic fluid, whilst staying in coexistence with its vapour, there is likely to be a discontinuity in the surface tension associated with the weakly first order transition. There is also a possibility of a change in sign of the gradient $\frac{\delta\gamma}{\delta T}$ around the transition, as wetting of some type occurs. Typical behaviours of the surface tension for isotropic (a) and nematic (b) wetting are shown below (Fig 2.13).

21
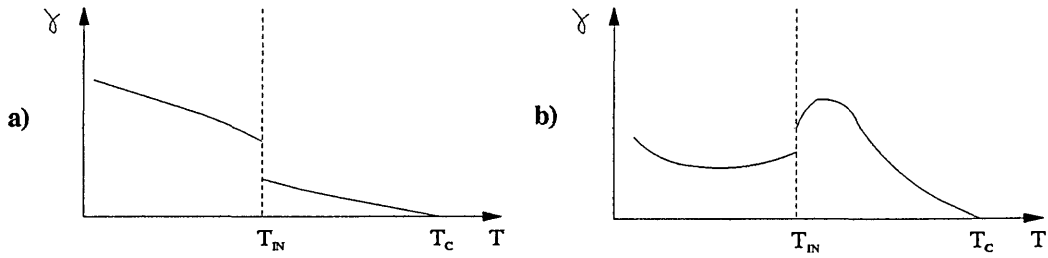
Figure 2.13: Behaviour of surface tension vs temperature [30] (a) Isotropic wetting; (b) Nematic wetting

In general, negative discontinuities occur for isotropic wetting whereas positive ones are usually observed in cases involving nematic wetting. This can be explained quite simply by considering the well known relationship [3]

$$\frac{d\gamma}{dT} = -(S_\sigma - S_\beta)$$

where S is entropy per unit area and the suffixes σ and β refer to the surface and bulk states. If there is any surface ordering then S_σ may be less than S_β and γ may show a positive slope. A large number of experimental studies have shown positive discontinuities (see refs in [3]), hardly surprisingly since the vast majority of liquid crystalline materials show nematic wetting at the free surface. However, some few examples of isotropic wetting can be deduced from appropriate surface tension behaviour. In particular, an early study of p-anisaldazine and MBBA [31] showed a negative discontinuity at the transition point, implying a surface disordering effect [32]. A region of positive gradient was observed below this; it is possible that this corresponds to enhanced layering at the surface at a temperature just below the bulk transition.

In conclusion, the behaviour of mesogens at free surfaces is surprisingly rich, even when considered at the simple level presented here. Various sorts of smectic surface ordering have also been observed (see eg. [33]), although these will not be expanded upon since they are beyond the scope of this thesis. The role of these free systems as references for the confined systems is in no doubt, since the complicated behaviour discussed here will need to be understood and modelled accurately before concise treatments of confined systems can successfully developed. It is with this modelling, both theoretically and using computer simulation, that attention will be concerned in the next chapter.

Chapter 3

Modelling Liquid Crystals

In this chapter an overview of the modelling techniques used for liquid phases is presented, together with a review of the current progress made with these methods in the liquid crystal field. Theoretical treatments are briefly dealt with first, then a more complete discussion of simulation work is given. The modelling methods used, both in previous investigations and this body of work are first considered, followed by studies of bulk ordering and concluding with the more complex interfacial systems.

3.1   Theoretical Models

The statistical mechanics of liquid crystals is exceptionally difficult, and even for the simplest physical models, no exact solution has been worked out [2].

A number of different analytical techniques are available to the theorist, which can be broadly classified into two fields. Phenomenological theories attempt to model an

observed behaviour empirically, but do not consider *a priori* molecular interactions. Conversely, molecular theories start from a consideration of inter-particle effects and predict the macroscopic behaviour in some way from these. Obviously assumptions and approximations have to be made in molecular theories to make them analytically tractable. One of the most important of these for mesogenic systems is the mean-field approximation, in which the molecular interactions are not considered individually but approximated collectively to give an average local effect - ie a mean field. This greatly simplifies the solution of these theories, but results in an incorrect treatment of local correlations; this can lead to erroneous predictions, especially in the vicinity of phase transitions where the correlation length scale is of primary importance.

Mesogenic theories have been applied to both bulk and confined systems as described below.

3.1.1 Bulk Systems

The vast majority of liquid crystals (mesogens) are rod-like in shape and in the 1940's, in his seminal work, Onsager [34] showed that a system of hard rods will display orientational order above a certain concentration. Onsager used a simple form of density functional theory, with a mean field type approximation, and made a number of assumptions. Firstly the rods were not able to interpenetrate each other, secondly, the volume fraction was much less than one (sparse system), and lastly the rods were very long.

Within these limits, it was successfully shown that such a system undergoes a first

order phase transition from the isotropic to nematic phase; this was the first proof that attractive forces are not necessary for a system to show spontaneous alignment. However, apart from the assumptions made above, this model differs from actual observations on thermotropic systems in many respects: the transition density is too low, the jump in density at the transition is too high, and the order parameter at the threshold is too big. Like all models involving only infinitely repulsive forces (so called hard models), the system is independent of temperature.

Maier and Saupe [35] developed a theory which takes into account the attractive intermolecular interactions, using a system of classical spin vectors located on the sites of a cubic lattice with nearest neighbour interactions. By solving this with a mean field approximation, they predicted a strongly first order transition to occur between the isotropic and nematic phases, at a transition temperature dependent upon the intermolecular potential. In particular the order parameter for the nematic phase was found to be much smaller than that predicted by Onsager and a lot closer to experimentally observed values.

However, later simulation results upon this spin system [36, 37] showed the isotropic-nematic transition to be weakly rather than strongly first order (similar to that observed experimentally), indicating that mean field theory is not a very good guide for such characterisation.

Recently, some attempts have been made to extend the mean field type approach to bidisperse systems, using first numerical [8] and later analytical [38] methods. This essentially Onsager-like approximation (ie. only steric interactions) revealed a number of interesting features; the longer rods are always more ordered than the

shorter ones; the presence of a strong fractionation effect (with the longer rods going preferentially to the nematic phase); a widened biphasic gap; and the possibility of nematic-nematic phase coexistence for sufficiently different sized rods. The prediction of so many features in such a simple system makes this an attractive area for study by computer simulation, which would have the advantage of treating more realistically the orientational correlations than the mean-field theory used here.

3.1.2 Interfacial Systems

Theoretical treatments of both confined and unconfined liquid crystal films have shown a rich phase behaviour. Phenomenological treatments [39, 40] based on a Landau-de Gennes [2] formalism have shown qualitative agreement with trends observed experimentally [21], such as shifting of the transition temperature relative to the bulk system. However, the number of different effects at work (ordering and disordering surface interactions, excluded volume effects etc) at a wide range of length-scales, coupled with the multitude of possible behaviours makes a complete understanding of these systems a considerable challenge. That said, the observation that subtle changes in intermolecular and molecule-substrate interactions can lead to considerable changes in the bulk behaviour suggests that this is a particularly suitable area for investigation by computer simulation.

The study of anchoring at the free liquid crystal - vapour interface is of importance both in its own right and as a reference for fully confined systems. The presence of an interface with no fixed barrier holding it in place allows particular attention to be focussed on the effect of bond-breaking symmetry upon the system. A surprisingly

rich phase behaviour has been suggested for the interface between a nematic liquid and its own saturated vapour, including various induced orientations at the surface as well as both partial and complete wetting regimes and anomalous surface tension dependency. Theoretical treatment of a lattice-based model [41] predicts cross-over between surface and bulk-region transitions for finite width systems. It is the competition between these effects that gives rise to such complicated behaviour in liquid crystal films.

In the last 15 years or so, molecular theories have made significant progress in this area. A number of papers [42–44] have been published in which a generalised van der Waals theory [45], based on spherical harmonic expansion of the anisotropic attractive component of the intermolecular interaction potential, has been used to analyse the wetting and alignment properties of the liquid-vapour interface, both above and below the bulk isotropic-nematic transition temperature. These show that appropriate choices of the various expansion terms can yield perpendicular, parallel or oblique alignment at the interface. Although direct mapping of these terms onto physical properties is difficult, the first second order term which couples the translational and rotational degrees of freedom, and thus gives rise to a non-trivial surface behaviour, has been shown to induce homeotropic alignment for prolate molecules, and planar for oblate ones. The next second order term, which has a weaker effect at the free interface, has been shown to have the opposite effect, with oblique alignment resulting when there is near-cancellation of these competing effects and higher order terms become relevant. Recently the assumption of a spherical hard core for these theories has been called into question [30], casting doubt over some of the predictions for highly anisotropic models. However the general trends predicted

are still thought to be valid.

A related paper [46] which employs explicit expansions of a range of parameterisations of the Gay-Berne potential [7, 47] has found that perpendicular alignment should arise in such systems. Conversely, studies based on perfectly ordered systems with ellipsoidally symmetric intermolecular interactions [48] predict parallel surface orientation. This apparent inconsistency is explained by noting [46] the considerable differences between the Gay-Berne form and its predecessor, the Berne-Pechukas potential [49], which is more consistent with the ellipsoidally symmetric potentials considered in the latter works.

Aside from considerations of induced orientation, the wetting effects of these systems upon approach to the vapour-isotropic-nematic triple point are also predicted to depend sensitively on the terms in the molecular model used. In summary, it has been found that increasing magnitude of the alignment inducing terms favours nematic wetting of the isotropic phase [44, 50], as would be expected intuitively. A change from partial to complete wetting occurs as these are increased above a certain value, and correspondingly, for sufficiently small values, the opposite is observed (isotropic wetting of the nematic phase or surface disordering).

The behaviour of the surface tension in this region has been linked with the differing wetting regimes. As was stated in Chapter 2, normally surface tension decreases with temperature, reaching a value of zero at the liquid-vapour critical point. Theoretical treatments of systems with disordering interfaces (ie. showing isotropic wetting) show this trend with the expected negative discontinuity at the nematic-isotropic transition. However for surface ordering systems an increase in the surface tension

with temperature (on either or both sides of the transition) has been predicted, along with either a positive or negative discontinuity at the transition [30, 43]. This is again in agreement with experimental observations described previously.

In conclusion, theoretical treatments of liquid crystalline systems have shown a reasonable degree of success in explaining experimental behaviour. The observation that repulsive interactions alone can give rise to mesogenic behaviour was an important early result. However, this hardly seems surprising now when it is known that most liquid behaviour is governed by hard core interactions, and that attractive effects can be regarded, with some reservations, as a simple perturbation away from this. Even in comparatively simple cases, though, theoretical techniques have not been wholly successful. For example they tend to overestimate the strengths of mesogenic transitions, and this is thought to be due to their inability to capture correctly the nature of orientational correlations. In more complicated interfacial and bi-disperse systems this problem will be even more acute, and it is here that computer simulation can provide a useful comparison between the effectiveness of a model and the theories being used to predict its behaviour.

3.2   Simulation Techniques

Computer simulations [5] aim to predict the properties of real systems and test theories based upon model systems by producing a correct behaviour for a relatively small idealised system of particles interacting through a given potential. The system is replicated periodically through space so as to avoid surface effects and enable a

reasonable approximation to bulk behaviour to be made. However, this can lead to problems, especially around phase transitions, due to suppression of long range fluctuations. There are two main techniques, Metropolis Monte Carlo (MC), which attempts to create a series of configurations for the system using random moves accepted with an appropriate probability, and molecular dynamics (MD), which solves Newton's equations of motion (to an acceptable degree of accuracy) for the system and can, therefore, be seen as representing the real evolution of the system through time. MD has the major advantage of allowing dynamical information to be obtained, however MC is conceptually the easier and was thus the first technique to be used. It has the advantage that many different sorts of move (not necessarily realistic) can be attempted, and through a prudent choice of these, certain systems can be brought to equilibrium with greater ease.

These techniques will now be further explained, starting in historical order with MC, which was also the first method used in this work.

3.2.1   Monte Carlo Theory

The term Monte Carlo [5] [51] has come into use to designate numerical methods in which specifically stochastic elements are introduced in contrast to the completely deterministic algebraic expressions of the MD approach. It was first used to describe a method developed at the end of the Second World War to study the diffusion of neutrons in fissionable material. The particular form used in liquid state physics was developed from this a few years later [52] and is generally known as Metropolis Monte Carlo (MC).

In the context of a liquid state simulation, the MC method involves generating a set of molecular configurations by making random displacements of the particles in a model. A new configuration is accepted or rejected according to a criterion which ensures that, in the limit of an infinite number of transitions, a given configuration occurs with a probability proportional to the Boltzmann factor for that configuration, whatever the initial condition of the model. A more detailed analysis is now given.

Consider the canonical ensemble ie. a system consisting of N particles in a fixed volume V and at a fixed temperature T (also referred to as constant NVT). The probability of a certain configuration m of the particles occuring is proportional to the Boltzmann factor of its potential energy, U_m, ie

$$p_{NVT}(m) \propto \exp\left(\frac{-U_m}{k_B T}\right).$$

(3.1)

To normalise this, the configuration integral is introduced. This is simply the sum of the Boltzmann factors for all the possible configurations of the system

$$Z_{NVT} = \int \exp\left(\frac{-U_m}{k_B T}\right) dm.$$

(3.2)

Using this, the probability of a certain configuration m occuring is now given by

$$p_{NVT}(m) = \frac{\exp\left(\frac{-U_m}{k_B T}\right)}{Z_{NVT}}.$$

(3.3)

32

The configuration integral can be thought of as being the configurational (potential) part of the partition function. The partition function is the fundamental property in statistical mechanics from which all other thermodynamic quantities, such as the appropriate free energy, can be obtained. However, its direct calculation for reasonably sized systems is practically impossible, and what is needed is a way to sample the system effectively so that other quantities can be obtained accurately. The average value of some function $f(m)$ in the canonical ensemble is given by

$$\langle f \rangle_{NVT} = \int p_{NVT}(m) f(m) \, dm \qquad (3.4)$$

and by sampling configurations at random, the integral can be estimated as

$$\langle f \rangle_{NVT} = \left\langle \frac{\sum_m^{trials} f(m) \exp\left(\frac{-U_m}{k_B T}\right)}{\sum_m^{trials} \exp\left(\frac{-U_m}{k_B T}\right)} \right\rangle . \qquad (3.5)$$

For an infinite number of trials, this random technique will give the correct result; however for the finite number of trials possible with computer simulation it tends to behave poorly, since it does not sample effectively the areas of phase space where the potential energy is such that significant contributions are made to the sum. In practice, most of the terms are virtually zero due, e.g., to a significant degree of molecular overlap, and as such the value required is incorrectly estimated.

The Metropolis technique instead uses an importance sampling technique where the configurations are chosen from a non-uniform distribution so that most of them make a significant contribution to the sums in Eqn 3.5. By sampling configurations

at random from a distribution p, the value of a function can be estimated as

$$\langle f \rangle_{NVT} = \left\langle f(m) \frac{p_{NVT}(m)}{p} \right\rangle_{trials}. \tag{3.6}$$

For most functions, the integrand will be significant where $p_{NVT}(m)$ is significant, and in these cases choosing $p = p_{NVT}(m)$ should give a good estimate of the integral:

$$\langle f \rangle_{NVT} = \langle f(m) \rangle_{trials}. \tag{3.7}$$

The difficult job is finding a method of generating a random sequence of states so that, by the end of the simulation, each state has occured with the appropriate probability. The solution is to set up a *Markov chain* of states of the liquid, which is constructed so that it has a limiting distribution of p_{NVT}. Each step in the Markov chain satisfies the requirements that it depends solely on the present state of the system (ie is independent of the previous states) and that the outcome of each step belongs to a finite set of states $[\Gamma_1, \Gamma_2, ...\Gamma_m, \Gamma_n, ...]$, called the state space. If π is defined as the transition matrix then the element π_{mn} is the probability of moving from state m to state n. The probability that the system is in a particular state is given by a state vector $p = [p_1, p_2, ..., p_m, p_n, ...]$. What is needed is a particular transition matrix such that the limiting distribution of the chain

$$p = \lim_{\tau \to \infty} p^1 \pi^\tau \tag{3.8}$$

34

is equal to the desired distribution ie p_{NVT}.

The limiting distribution of p is required to be independent of the starting guess, p^1. It must also satisfy the eigenvalue equation

$$p = p\pi.$$ (3.9)

A π needs to be found which satisfies the equation

$$\sum_m p_m \pi_{mn} = p_n.$$ (3.10)

This can be ensured using the condition of 'microscopic reversibility'

$$p_m \pi_{mn} = p_n \pi_{nm}.$$ (3.11)

The Metropolis solution is

$$\pi_{mn} = \alpha_{mn} \qquad\qquad p_n \geq p_m \quad m \neq n$$

$$\pi_{mn} = \alpha_{mn}\left(\frac{p_n}{p_m}\right) \qquad p_n < p_m \quad m \neq n$$

$$\pi_{mm} = 1 - \sum_{n \neq m} \pi_{mn}$$

where α is a symmetrical stochastic matrix ($\alpha_{mn} = \alpha_{nm}$), often called the underlying matrix of the Markov chain. The symmetric properties of α ensure that the Metropolis solution satisfies the condition of microscopic reversibility.

35

To implement the Metropolis solution, it is necessary to specify α. The commonly used technique for generating a new configuration n from an old one m is to choose an atom (i) at random and displace it from its old position $\mathbf{r}_i^m$ with equal probability to any point $\mathbf{r}_i^n$ within a sphere centred on $\mathbf{r}_i^m$. On a computer, there are a large but finite number of new positions N_R and in this case α_{mn} can simply be defined as $\frac{1}{N_R}$.

The appropriate element of the transition matrix, π, depends upon the relative probabilities of the initial state m and the final state n. There are two cases to consider. If the move is downhill in energy ie $\Delta U = U_n - U_m \leq 0$ then $p_n \geq p_m$ and $\pi_{mn} = \alpha_{mn}$. Since the probability α_{mn} has already been incorporated in choosing the move, it can now be accepted automatically. However, if the move is uphill in energy $\Delta U = U_n - U_m > 0$ then $p_n < p_m$ and $\pi_{mn} = \alpha_{mn} (p_n/p_m)$, so the move has to be accepted with a probability (p_n/p_m). This ratio can be expressed as the Boltzmann factor of the energy difference

$$\frac{p_n}{p_m} = \frac{Z_{NVT}^{-1} \exp\left(\frac{-U_n}{k_B T}\right)}{Z_{NVT}^{-1} \exp\left(\frac{-U_m}{k_B T}\right)} = \exp\left(\frac{-\Delta U}{k_B T}\right) \tag{3.12}$$

To accept a move with this probability, a random number ψ is generated uniformly on $(0,1)$ and compared with $\exp\left(\frac{-\Delta U}{k_B T}\right)$. If it is less than the exponential, the move is accepted. If the move is rejected then the system remains in its current state m, in accordance with the finite probability π_{mm}, and the old configuration is recounted as a new state in the chain.

A typical Monte Carlo scheme is implemented as follows:

1) Generate new configuration.

2) Calculate energy change ΔU.

3) Calculate $X_{mn} = min\left(1, \exp\left(\frac{-\Delta U}{k_B T}\right)\right)$

4) Generate random variable ψ on [0,1]

5) Accept move if $\psi \leq X_{mn}$

This procedure is relatively easy to implement on a computer and several different types of MC simulation have been carried out in the NVT ensemble.

For anisotropic systems, the underlying matrix of the Markov chain is altered to allow moves which usually consist of a combined translation and rotation of one molecule. This is quite straightforward to implement, simply involving a simultaneous displacement in both the translational coordinates (as before) and the orientational coordinates (usually in terms of Euler angles or space fixed axes). However it is important not to bias the rotational part of the move by sampling uniformly from the Euler angles as might seem intuitively correct. Rather, it should be done either by choosing random displacements in the cosine of one of the angles [5], or alternatively by use of the Barker Watts algorithm [53], which involves rotating the molecule by a random amount about one of the three space-fixed axes (chosen at random). Both of these methods can be shown to satisfy microscopic reversibility, and the latter was used in this work.

It is also possible to generalise the Metropolis solution to other statistical mechanical ensembles; all that is needed is an appropriate modification of the transition matrix

so that it gives the correct thermodynamic distribution of states. For instance, in the isothermal-isobaric (NPT) ensemble, the configuration integral is given by

$$Z_{NPT} = \int \exp\left(\frac{-PV}{k_BT}\right) dV \int \exp\left(\frac{-U_m}{k_BT}\right) dm. \qquad (3.13)$$

The Metropolis scheme is implemented by generating a Markov chain of states which has a limiting distribution proportional to

$$p_{NPT}(m) = \frac{\exp\left(\left(\frac{-U_m - PV}{k_BT}\right) + N\ln V\right)}{Z_{NPT}} \qquad (3.14)$$

by accepting trial moves with a probability

$$X_{mn} = min\left(1, \exp\left(\frac{-\Delta H_{mn}}{k_BT}\right)\right) \qquad (3.15)$$

where

$$\Delta H_{mn} = \Delta U_{mn} + P(V_n - V_m) - \frac{N}{k_BT}\ln\left(\frac{V_n}{V_m}\right) \qquad (3.16)$$

and is closely related to the enthalpy change in moving from state m to state n.

3.2.2 The Gibbs Ensemble

Since a major aim of this thesis was to investigate the phase behaviour of liquid crystal systems with a specific interest in coexistence regions, a method was required for the accurate location of the phase boundaries. Simulating coexisting phases

38

using traditional 'one box' techniques (as outlined above) is very expensive in that relatively large systems have to be used to calculate reliable coexistence properties, because of the predominating interfacial effects in smaller systems [54].

An alternative would be to simulate the two phases separately and to determine the temperature at which their pressures and chemical potentials equate. However, simulation does not yield quantities like the free energy and chemical potential directly, and more indirect and expensive methods need to be used. Techniques used previously have included determining the equation of state of the system and obtaining the free energy this way [55], and using the Widom particle insertion method [56] to calculate the chemical potential. However, frequently long and numerous runs are required in the vicinity of the phase transitions, and such procedures are obviously very expensive computationally.

Instead it was decided to make use of a relatively new technique proposed by Panagiotopoulos [57], the so called Gibbs ensemble, which has been shown to significantly reduce the computer time required for phase equilibrium calculations.

The Gibbs method uses two distinct simulation boxes, which are coupled using MC rules. These rules are chosen to ensure that the subsystems are in equilibrium. When a conventional one box simulation is performed in the two phase region, droplets of one phase are formed in a sea of the other. In the Gibbs ensemble, the system can lower its free energy by filling each box with one of the two coexisting phases. In this way the formation of interfaces, which increase the free energy because of the interfacial tension between the two phases, is avoided. The coexistence properties can be obtained directly from the two boxes and, since the method avoids interfaces,

it can be used with a relatively small number of particles.

A more detailed analysis of the Gibbs ensemble, together with a derivation of the appropriate acceptance criteria will now be given.

In his original article, Panagiotopoulos introduced the Gibbs ensemble as a combination of the constant-NVT, constant-NPT and constant-μVT ensembles. Here we take a different point of view, and consider the Gibbs ensemble as a new ensemble [54].

Consider a system at constant temperature (T), volume (V) and number of particles (N). The system is divided into two non-interacting subsystems 1 and 2. In a simulation, this implies that each box has periodic boundary conditions and that particles in one box do not interact directly with particles in the other. The particles are distributed over the two subsystems keeping the total number constant. The volume of each box may vary in such a way that the total volume remains constant.

In the configuration integral of this ensemble, we have to take into account the number of possible distributions of N particles over the two subsystems, to allow for the subsystems to change volume between 0 and V, and to consider all possible configurations in each subsystem. This gives a configuration integral

$$Z_{NVT} = \sum_{n_1=0}^{N} \binom{N}{n_1} \int_0^V dV_1 \int_{V_1} \exp\left(\frac{-U_m}{k_B T}\right) dm \times \int_{V-V_1} \exp\left(\frac{-U_m}{k_B T}\right) dm \quad (3.17)$$

where n_1 is the number of particles in box 1 and V_1 is the volume of box 1.

Using this, it can be shown that, in the thermodynamic limit, the free energy density for the Gibbs ensemble is identical to that of the canonical (NVT) ensemble, and will sample the same phase space. At state points where there is only one phase, the free energy of the Gibbs ensemble has its minimum value when both boxes have a density equal to the equilibrium density of the canonical ensemble. In the case of a first order transition, the surface free energy is the driving force which causes the system to separate into two homogeneous phases. This property makes the Gibbs ensemble a convenient ensemble to study phase coexistence.

The Gibbs ensemble technique can be implemented effectively using standard MC supplemented by moves which allow the whole of phase space to be sampled. From the configuration integral of the Gibbs ensemble, it follows that moves have to be made which displace the particles in the two boxes, change the volume of the subsystems, and exchange particles between the boxes. The acceptance rules for these moves can be obtained directly from the configuration integral assuming the condition of detailed balance in the same way as for conventional Metropolis MC.

For example, assuming that state n is obtained from state m via the displacement of a particle in box 1, the ratio of the statistical weights of the two configurations can be written as

$$\frac{N_n}{N_m} = \exp\left(-\frac{1}{k_B T}\left(U_n - U_m\right)\right).$$
(3.18)

Using the condition of detailed balance, we arrive at the following acceptance rule

41

$$X_{mn} = min\left(1, \exp\left(-\frac{1}{k_B T}\left(U_n - U_m\right)\right)\right). \qquad (3.19)$$

For an increase in volume of box 1 by an amount ΔV (and a simultaneous reduction in the volume of box 2), the ratio of the statistical weights leads to an acceptance rule

$$X_{mn} = min\left(1, \frac{(V_1 + \Delta V)^{n_1}\left(V - (V_1 + \Delta V)\right)^{N-n_1}}{V_1^{n_1}\left(V - V_1\right)^{N-n_1}} \exp\left(-\frac{1}{k_B T}\left(U_n - U_m\right)\right)\right).$$
$$\qquad (3.20)$$

If the configuration n is obtained from configuration m by removing a particle from box 1 and inserting it into box 2, the ratio of statistical weights gives an acceptance rule

$$X_{mn} = min\left(1, \frac{n_1\left(V - V_1\right)}{\left(N - n_1 + 1\right) V_1} \exp\left(-\frac{1}{k_B T}\left(U_n - U_m\right)\right)\right). \qquad (3.21)$$

The moves described above are enough to sample the Gibbs ensemble effectively. The only other factor to be taken account of with homogeneous systems is the frequency of the different types of move, and the order in which they are attempted.

For heterogeneous systems, such as the bidisperse mixtures studied in Chapter 4, the particle transfer step has to be modified slightly to ensure detailed balance [58]. The type of particle to be transfered has to be chosen with a fixed (but otherwise arbitrary) probability, usually one which results in equal probabilities of attempted

interchange of all species.

The major drawback of the Gibbs ensemble is that at high densities, the particle exchange moves are accepted with a low probability, slowing down the equilibration of the system and eventually making the method untenable. Special techniques can be used to overcome this, such as incorporating configurational and/or orientational bias into the insertion step, although this has not been attempted in this work.

An important speedup can however be achieved with a bidisperse mixture, due to the fact that smaller particles are obviously easier to insert than larger ones. In the modified method [59], direct transfers are attempted only for the smaller particle (say component two). For component one, the transfer step involves the following: in one of the two regions, a randomly selected particle of species two becomes a particle of species one, whilst at the same time in the other region the inverse procedure is applied. The move is accepted with a probability

$$X_{mn} = min\left(1, \frac{V^1 N_1^2 V^2 N_2^1}{V^2 \left(N_1^1 + 1\right) V^1 \left(N_1^2 + 1\right)} \exp\left(-\frac{1}{k_B T}\left(U_n - U_m\right)\right)\right). \qquad (3.22)$$

The advantage of the modification is that it is much more efficient to increase the size of an existing molecule than to attempt to place a molecule in a random position. Tests in the literature [59] have demonstrated that this new 'semi-grand' Gibbs method gives results statistically indistinguishable from the old.

3.2.3 Molecular Dynamics

3.2.3.1 Translational Motion

Molecular dynamics is a method [5] which solves the classical equations of motion for a system of N molecules interacting via a potential U. There are various ways of expressing these equations [60], perhaps the most fundamental being the Lagrangian equation of motion

$$\frac{d}{dt}\left(\frac{\partial L}{\partial \dot{q}_k}\right) - \left(\frac{\partial L}{\partial q_k}\right) = 0 \qquad (3.23)$$

where the Lagrangian function $L(q, \dot{q})$ is defined in terms of the kinetic and potential energies

$$L = K - U \qquad (3.24)$$

and is considered to be a function of the generalised coordinates q_k and their time derivatives $\dot{q}_k$. When considering a system of atoms with Cartesian coordinates, $\mathbf{r}_i$, and using the usual definitions of U and K, eqn. 3.23 becomes

$$m_i\ddot{\mathbf{r}}_i = \mathbf{f}_i \qquad (3.25)$$

where m_i is the mass of the atom i and

$$\mathbf{f}_i = \nabla_{\mathbf{r}_i} L = -\nabla_{\mathbf{r}_i} U \qquad\qquad (3.26)$$

is the force on that atom. These equations also apply to the centre of mass motion of a molecule, with $\mathbf{f}_i$ representing the total force acting upon molecule i. The equations of rotation take a similar form, and will be considered later. For anisotropic molecules, the form of the force is more complicated as the potential is not only a function of $\mathbf{r}_i$. Price et al [61] derived a method which gives explicitly the forces and torques necessary for the simulation of a fluid of linear molecules.

Computing the centre of mass trajectories requires solution of a system of $3N$ second order differential equations, eqn. (3.25). This is achieved using finite difference methods. The general scheme is to take the known molecular positions, velocities and other dynamic information at time t and attempt to obtain the positions, velocities, etc, at a later time $t + \delta t$, to a sufficient degree of accuracy. The choice of the time interval δt depends upon the method used, but δt should be significantly smaller than the typical time taken for a molecule to travel its own length. There are a number of different time evolution algorithms which fall into the general category of finite difference methods. The most commonly used, and conceptually the simplest, method is the $Verlet$ algorithm which will now be described.

This method was initially adopted by Verlet [62] and offers a direct solution to eqn. (3.25). The method is based upon the positions $\mathbf{r}(t)$, accelerations $\mathbf{a}(t)$, and positions $\mathbf{r}(t - \delta t)$ from the previous step. Taking Taylor expansions about $\mathbf{r}(t + \delta t)$ and $\mathbf{r}(t - \delta t)$ gives,

$$r(t + \delta t) = r(t) + \delta t v(t) + \tfrac{1}{2}\delta t^2 a(t) + \ldots .$$

$$r(t - \delta t) = r(t) - \delta t v(t) + \tfrac{1}{2}\delta t^2 a(t) - \ldots .$$

$$(3.27)$$

By adding these equations together, an equation for advancing the positions is obtained,

$$r(t + \delta t) = 2r(t) - r(t - \delta t) + \delta t^2 a(t). \qquad (3.28)$$

This method does not require the velocities to calculate the trajectories, though they are required to calculate kinetic energy. They may be obtained from the formula,

$$v(t) = \frac{r(t + \delta t) - r(t - \delta t)}{2\delta t}. \qquad (3.29)$$

The eqn. (3.28) is correct except for errors of the order δt^4, the local error. The velocities from eqn. (3.29) are subject to errors of order δt^2. More accurate estimates of $v(t)$ can be made if more variables are stored, but this adds to the inconvenience that $v(t)$ can only be calculated once $r(t + \delta t)$ is known.

The algorithm is simple to program, exactly reversible in time and, given conservative forces, is guaranteed to conserve linear momentum. It has also shown excellent energy conserving properties. However, the handling of the velocities is awkward, and the form of eqn. (3.28) may needlessly introduce some numerical imprecision, because it includes the difference of two similar quantities.

Modifications to the basic Verlet scheme have been proposed to improve the algorithm. One such modification is known as the *leap-frog* scheme [63]. The algorithm is now expressed as

$$\mathbf{r}(t + \delta t) = \mathbf{r}(t) + \delta t \mathbf{v}(t + \tfrac{1}{2}\delta t)$$
$$\mathbf{v}(t + \tfrac{1}{2}\delta t) = \mathbf{v}(t - \tfrac{1}{2}\delta t) + \delta t \mathbf{a}(t). \tag{3.30}$$

This algorithm stores the current positions $\mathbf{r}(t)$, accelerations $\mathbf{a}(t)$ and mid-step velocities $\mathbf{v}(t - \tfrac{1}{2}\delta t)$. The velocity equation is applied first, such that the velocities leap over the positions to give the next mid-step values $\mathbf{v}(t + \tfrac{1}{2}\delta t)$. Subsequently, the position equation is applied to advance the positions, and the new accelerations are calculated for the next step. The on step velocities can be calculated using the formula

$$\mathbf{v}(t) = \frac{\mathbf{v}(t + \tfrac{1}{2}\delta t) + \mathbf{v}(t - \tfrac{1}{2}\delta t)}{2}. \tag{3.31}$$

Elimination of the velocities from these equations shows that the method is algebraically equivalent to Verlet's algorithm. The velocities now appear explicitly within the scheme, which is advantageous because, for example, control of simulation temperature is achieved by appropriately scaling velocities.

3.2.3.2 Rotational Motion

In classical mechanics, it is natural to divide molecular motion into translation of the centre of mass and rotation about the centre of mass [60]. The rotational motion is governed by the torque, τ_i, about the centre of mass. This torque enters the rotational equations of motion in the same way that the force enters the translational equations. However, the nature of orientation space guarantees that the equations of re-orientational motion need not be as simple as the translational equations.

For a linear molecule, only the angular velocity and the torque perpendicular to the molecular axis need be considered. Taking $\mathbf{u}$ as the unit vector defining the axis, the torque can be expressed as,

$$\tau = \mathbf{u} \times \mathbf{g} \tag{3.32}$$

where $\mathbf{g}$, the gorque, is simply an angular derivative of the intermolecular potential. For a uniaxial particle, the vector $\mathbf{g}$ can always be replaced by its component perpendicular to the molecular axis, such that,

$$\tau = \mathbf{u} \times \mathbf{g}^\perp \tag{3.33}$$

where,

$$\mathbf{g}^\perp = \mathbf{g} - (\mathbf{g}.\mathbf{u})\mathbf{u}. \tag{3.34}$$

The equation of rotational motion can then be expressed using the second order differential equation [64]

$$\ddot{\mathbf{u}} = \frac{\mathbf{g}^\perp}{I} + \lambda\mathbf{u} \qquad (3.35)$$

where I is the moment of inertia perpendicular to $\mathbf{u}$ and λ is a Lagrange multiplier, which constrains $|\mathbf{u}|$ to be a constant of motion. A proposed solution to this equation uses a leap-frog algorithm [65]. Firstly, an expression for λ is obtained by considering the advancement of coordinates over a half time step

$$\dot{\mathbf{u}}(t) = \dot{\mathbf{u}}(t - \frac{1}{2}\delta t) + \frac{1}{2}\delta t \left[\frac{\mathbf{g}^\perp(t)}{I} + \lambda(t)\mathbf{u}(t)\right] \qquad (3.36)$$

Taking the scalar product of both sides with the vector $\mathbf{u}(t)$, and using $\mathbf{u}(t).\dot{\mathbf{u}}(t) = 0$ and $\mathbf{u}(t).\mathbf{g}^\perp(t) = 0$ gives,

$$\lambda(t)\delta t = -2\dot{\mathbf{u}}(t - \frac{1}{2}\delta t).\mathbf{u}(t) \qquad (3.37)$$

and so

$$\delta t\ddot{\mathbf{u}}(t) = \delta t\frac{\mathbf{g}^\perp(t)}{I} - 2\left[\dot{\mathbf{u}}(t - \frac{1}{2}\delta t).\mathbf{u}(t)\right]\mathbf{u}(t). \qquad (3.38)$$

This is then used to advance a full step in the integration algorithm

49

$$\dot{\mathbf{u}}(t + \frac{1}{2}\delta t) = \dot{\mathbf{u}}(t - \frac{1}{2}\delta t) + \delta t \ddot{\mathbf{u}}(t) \qquad (3.39)$$

and the step is completed using,

$$\mathbf{u}(t + \delta t) = \mathbf{u}(t) + \delta t \dot{\mathbf{u}}(t + \frac{1}{2}\delta t). \qquad (3.40)$$

This algorithm has been used in liquid crystal simulations and produces stable and accurate trajectories.

3.2.3.3 Constant-Temperature Molecular Dynamics

The methods described above allow simulation in the *NVE* ensemble. In order to simulate other ensembles, modifications to these methods need to be made. The following section gives an overview of the constraint method which has been used to conduct fixed temperature simulations in this programme of work.

The constraint method simply re-scales the velocities at each time step by a factor of $(T/\mathcal{T})^{1/2}$, where $\mathcal{T}$ is the current kinetic temperature and T is the desired thermodynamic temperature. The equations of motion are expressed as [5, 66],

$$\dot{\mathbf{r}} = \mathbf{p}/m$$

$$\dot{\mathbf{p}} = \mathbf{f} - \xi(\mathbf{r}, \mathbf{p})\mathbf{p} \qquad (3.41)$$

where $\xi(\mathbf{r}, \mathbf{p})$ can be considered as a friction coefficient which varies so as to constrain $\mathcal{T}$ to a constant value. A variant of the leap-frog algorithm has been devised [67] which takes the form,

$$\mathbf{v}\left(t + \frac{1}{2}\delta t\right) = \mathbf{v}\left(t - \frac{1}{2}\delta t\right) + (\mathbf{a}(t) - \xi \mathbf{v}(t))\,\delta t. \qquad (3.42)$$

To implement this solution, an unconstrained half step is made,

$$\mathbf{v}'(t) = \mathbf{v}\left(t - \frac{1}{2}\delta t\right) + \frac{1}{2}\mathbf{a}(t)\delta t. \qquad (3.43)$$

Using these, the constrained velocities can be calculated using,

$$\mathbf{v}\left(t + \frac{1}{2}\delta t\right) = (2\chi - 1)\mathbf{v}\left(t - \frac{1}{2}\delta t\right) + \chi \mathbf{a}(t)\delta t \qquad (3.44)$$

where $\chi = \left(1 + \frac{1}{2}\xi \delta t\right)^{-1} = (T/\mathcal{T})^{1/2}$.

Similar arguments may be used to convert to rotational algorithms, such that the rotational and translational kinetic energies may be constrained separately [68].

3.2.4 Periodic Boundary Conditions

It is common for a real system to have of the order 10^{23} particles, whereas a typical MC or MD simulation can only deal with 10^2 to 10^4 particles due to the computational overhead involved when considering large systems. Confining the particles

within a geometric shape will cause problems with surface effects for such a small system. Periodic boundary conditions are used to overcome this problem and involve effectively replicating the system box in all directions throughout space. If a particle leaves the system through one side then it will re-enter on the opposite side thus keeping the number of particles considered constant.

It is important to ask whether the properties of a small, infinitely periodic system and the macroscopic system which it represents are the same. This depends both on the range of the intermolecular potential and the phenomenon under investigation. If the range of the potential is large enough in comparison to the box size, then there will be a significant interaction between a particle and its own periodic image, imposing a degree of symmetry upon a structure which should in reality be isotropic. There can also be problems in the vicinity of phase transitions, since these can involve the creation of long range fluctuations which are suppressed by periodic conditions. This can lead to a rounding and shifting of the phase transition, and transitions which are known to be first order often exhibit the characteristics of higher order transitions when modelled in a small box due to the suppression of fluctuations. The implications of this periodicity will be further discussed along with the relevant results in Chapters 4 and 5.

3.2.5 Interaction Potentials

In a system of N interacting particles, the potential energy can be divided into terms depending on the positions (and orientations) of the individual atoms, pairs, triplets

etc

$$U = \sum_i e_1\left(\mathbf{r}_i\right) + \sum_i \sum_{j>i} e_2\left(\mathbf{r}_i, \mathbf{r}_j\right) + \sum_i \sum_{j>i} \sum_{k>j>i} e_3\left(\mathbf{r}_i, \mathbf{r}_j, \mathbf{r}_k\right) + \ldots \qquad (3.45)$$

where e_1 represents the effect of an external field, e_2 represents a two body pair-wise potential, e_3 represents a three body triplet-wise potential etc. The majority of the potential energy comes from the pair interaction term, however the triplet term is reasonably significant at liquid densities, accounting for up to ten percent of the total. It and higher terms are rarely used in computer simulations though, because they are extremely time consuming to calculate. Fortunately this pairwise approximation still gives a remarkably good description of liquid properties [69], though it should be noted that the potentials commonly used in computer simulation are effective pair potentials that represent all the many body effects, and are not necessarily the same as (or even that similar to) the actual pair potentials in real systems [5].

3.2.6   Analysis

Within the field of molecular simulation, the variables to be analysed can be split into two groups

a) Thermodynamic quantities - such as pressure, temperature, energy.

b) Structural quantities - order parameters, distribution functions.

Generally, a number of thermodynamic quantities are fixed at the beginning of a

simulation, depending upon which ensemble is being used.

3.2.6.1 Pressure

The pressure can calculated in the course of a simulation by using the virial theorem

$$P = P_{ideal} + \langle P_{excess} \rangle = \rho k_B T + \left\langle \frac{W}{V} \right\rangle \qquad (3.46)$$

where the angular brackets denote an ensemble average. The virial, W, is given by

$$W = -\frac{1}{3} \sum_{i=1}^{N-1} \sum_{j>i}^{N} \mathbf{r}_{ij} \cdot \mathbf{F}_{ij}. \qquad (3.47)$$

This can also be used in a simulation for which the pressure is specified to provide a useful check of the program.

3.2.6.2 Nematic Order Parameter

The nematic order parameter, P_2, measures the degree of orientational order in a system. It is given by the run average of

$$P_2 = \frac{1}{N} \sum_{i=1}^{N} \left[\frac{3}{2} (\hat{\mathbf{u}}_i \cdot \hat{\mathbf{d}})^2 - \frac{1}{2} \right] \qquad (3.48)$$

where $\hat{\mathbf{u}}_i$ is the orientation vector of molecule i, and $\hat{\mathbf{d}}$ is the system director (defined as the orientation that maximises the right hand side of eqn. (3.48)). Its value

54

ranges from 1 for a perfectly aligned crystal to $\sim N^{-\frac{1}{2}}$ for an isotropic system (ie no orientational order).

In practice, the director need not be determined, since the order parameter is usually calculated from the Q-tensor,

$$Q = \frac{1}{N} \sum_{i=1}^{N} \begin{pmatrix} q_i\left(x,x\right) & q_i\left(x,y\right) & q_i\left(x,z\right) \\ q_i\left(y,x\right) & q_i\left(y,y\right) & q_i\left(y,z\right) \\ q_i\left(z,x\right) & q_i\left(z,y\right) & q_i\left(z,z\right) \end{pmatrix} \qquad (3.49)$$

where $q_i(x,y)$ is the product of the x and y component direction cosines of molecule i.

By diagonalising Q three eigenvalues are obtained, the largest of which, λ_1, is used to evaluate the nematic order parameter via

$$P_2 = \lambda_1 - \frac{1}{2}\left(\lambda_2 + \lambda_3\right) = \frac{1}{2}\left(3\lambda_1 - 1\right) \qquad (3.50)$$

where $\lambda_1 + \lambda_2 + \lambda_3 = 1$

3.2.6.3 Radial Distribution Function

The radial distribution function $g\left(r\right)$ provides structural information about the system. It is defined as the probability of finding a pair of particles a distance r apart, relative to the probability expected for a completely random distribution at the same density.

It is usually calculated in computer simulations by compiling a histogram. The volume around each particle is divided into concentric spherical shells, and the number of particles in each shell is counted and divided by the shell volume (given by the difference between two spherical volumes), to obtain the local density. The densities at each distance are then averaged over all particles, and normalised with the overall density to obtain $g(r)$.

$$g(r) = \frac{1}{\rho^* \frac{4}{3}\pi \left((r+dr)^3 - (r-dr)^3\right)} \frac{1}{N} \sum_{i=1}^{N} N_j \tag{3.51}$$

where N_j is the number of particles j such that $r + dr >\mid r_i - r_j \mid> r - dr$.

The function $g(r)$ can be split up into its two components parallel and perpendicular to the nematic director, $g_{\parallel}$ and $g_{\perp}$. These are calculated in a similar fashion except using the parallel and perpendicular components of the intermolecular distance instead of the scalar distance $\mid r_i - r_j \mid$; these are given by

$$r_{\parallel} = \mathbf{r}_{ij} \cdot \hat{\mathbf{d}} \tag{3.52}$$

$$r_{\perp} = \sqrt{\left((r_i - r_j)^2 - r_{\parallel}^2\right)} \tag{3.53}$$

where $\hat{\mathbf{d}}$ is the nematic director obtained for the P_2 calculation. In these two cases the normalising volume needs to be modified appropriately; instead of considering two spheres and using their difference as the volume, a sub-space of each of these spheres is used, such that in each space the resolved distance is of the appropriate length or less (being $(r + dr)$ and $(r - dr)$). The difference in volume of the

two sub-spaces is then again used as the normalising volume (replacing the factor $\frac{4}{3}\pi\left((r+dr)^3-(r-dr)^3\right)$ in Eqn 3.51).

3.2.7 Reduced Units

In computer simulations it is normal to use the mass of the molecule as a fundamental unit, ie. set $m_i = 1$. As a consequence the particle momenta and velocities become identical, as do the forces and acceleration. For molecules interacting by pair potentials of a relatively simple form this approach can be extended further. In the Lennard-Jones potential the molecular interactions are completely specified by the parameters ϵ and σ, and from these further fundamental units of energy, temperature etc may be defined

$$\text{Density} \qquad \rho^* = \rho\sigma^3 \qquad (3.54)$$

$$\text{Temperature} \qquad T^* = k_B T/\epsilon \qquad (3.55)$$

$$\text{Energy} \qquad E^* = E/\epsilon \qquad (3.56)$$

$$\text{Pressure} \qquad P^* = P\sigma^3/\epsilon \qquad (3.57)$$

$$\text{SurfaceTension} \qquad \gamma^* = \gamma\sigma^2/\epsilon \qquad (3.58)$$

Since the Gay-Berne potential is essentially an anisotropic form of the Lennard-Jones, the reduced units used in this work are all defined in the same way.

The main advantage of using reduced units is that it avoids the possible embarrass-

ment of conducting identical simulations. There are also technical advantages in that when paramters such as ϵ and σ are given a value of unity, they do not need to appear in a program at all, and thus some time will be saved on the calculation of potential energy, forces etc.

3.3 Liquid Crystal Simulations

The types of model used to simulate liquid crystals off lattice can be broadly split into two main types - hard and soft particle models, each of which have been studied extensively. Both of these are discussed in this review, concentrating firstly on bulk systems and the history of liquid crystal simulation, with particular emphasis on previous studies using the Gay-Berne model, which has been used exclusively in the work in this thesis. Relevant work on bidisperse bulk systems is also discussed. Attention is then switched to interfacial systems, considering both those with free surfaces, as in the work conducted here, and with some sort of interacting wall. Passing consideration is given to lattice systems where they have shown effects of interest in bidisperse and interfacial systems. However, in general they were not thought to be as important as the off-lattice studies which have been conducted.

3.3.1 Hard Particle Models

Hard particle models consist simply of an infinitely repulsive core within which no penetration is possible. They contain no attractive region, and it is their simplicity which makes them so useful to the computer simulator. The first simulations used

hard particles, and over the years they have proved surprisingly effective at reproducing features of the liquid state, showing that the main driving forces behind liquid structure are excluded volume effects (although liquid crystalline behaviour has been observed using models with no hard core and anisotropic attractive interactions [70]).

It is therefore not surprising that the first successful simulations of mesogens used anisotropic hard particle models. As described on page 25, Onsager showed in 1948 that orientational ordering will be seen in a system of needle-like hard bodies when the density increases above a certain (shape-dependent) value, so it was known that these particles were capable of forming mesophases.

3.3.1.1 Ellipsoids

Onsager's theory was first verified by Frenkel and Eppenga [71] when they used MC simulations to show that a system of infinitely thin hard disks undergoes an isotropic-nematic transition. However, due to the platelets having zero volume, this system cannot crystallise and thus was guaranteed to display a nematic phase at sufficiently high densities.

Frenkel and co-workers [72] went on to explore the phase diagram for the hard ellipsoid system, considering a whole range of axial ratios from infinitely thin platelets through hard spheres up to various lengths of rod-like molecules. It was found that the stability of the nematic phase depends upon the degree of anisotropy in the molecule, and that although a nematic phase is seen for axial ratios of $e=1/2.75$ and 3 ($e=1$ is equivalent to a hard sphere), no nematic phase exists for less extreme

ratios.

More extreme cases of $e=1/10,1/5,1/3,3,5,10$ have since been investigated [73] and in all cases displayed a spontaneous ordering to the nematic phase as the system underwent uniform compression. It was also noted that upon transformation from prolate to oblate (e to $1/e$) the phase diagram is almost symmetrical, the oblate molecules being slightly more aligned at a given density than the corresponding prolate molecules.

The coexistence behaviour of the hard ellipsoid system at the isotropic-nematic transition has subsequently been investigated [74] using the Gibbs ensemble and standard Monte Carlo simulations with the Gibbs-Duhem integration technique. This enables navigation along the coexistence line from a known reference point. The Gibbs ensemble technique was found to be tractable only for an extreme axial ratio, $e=20$, where the low density at the transition makes insertion of particles easier. The transition was seen to weaken with decreasing elongation, and comparison was made between the simulation results and a modified form of Onsager theory. A reasonable comparison was seen for the modified version, whereas the original Onsager theory, although good in the limit of infinite rods, quickly became inaccurate as the rods were shortened.

Studies have also been made of bidisperse ellipsoid systems, albeit rods and plates [9]. Using the Gibbs ensemble technique, theoretically predicted demixing was observed, with coexistence typically occuring between a rod rich calamitic nematic system and a plate rich discotic nematic system. A biaxial phase was also seen, although its region of stability was severely limited by the system tending to demix into two co-

existing uniaxial phases. The use of the Gibbs ensemble technique to observe liquid-liquid coexistence, in this relatively dense system, is encouraging for the bidisperse work in the thesis, although it was noted that the particle insertion move was particularly difficult. The number of attempted insertions, however, was not adjusted so as to give 1-3% of the particles transferring for each step, as has been recommended for atomic systems [57, 58], since the orientational fluctuations here were observed to occur on a much longer timescale than the positional fluctuations in such systems.

3.3.1.2 Spherocylinders

Another computationally inexpensive hard core model for mesogens is the spherocylinder, which consists of a cylinder of length L, diameter D with hemispherical caps of diameter D. The first simulations using this model [75] considered systems of parallel spherocylinders with $5 \geq L/D \geq 0.25$, thus even at the lowest densities the system has nematic order. Certainly the most striking result of this work was that for $L/D > 0.5$ the system displayed a stable smectic phase, the range of which increased with the non-sphericity of the particles. Subsequent work [76] revealed the existence of stable columnar phases (where the particles are confined in liquid like columns) for $L/D > 4$ at densities intermediate between the smectic and crystalline phases.

The effect of the orientational degrees of freedom on the system (ie removing the parallel constraint) was first investigated for $L/D = 5$ [77] and was later extended to other aspects [78]. It was found that for $L/D < 3$ only isotropic liquid and crystalline phases can occur. For larger L/D values, stable smectic and nematic

phases were found.

Recently, an attempt was made to trace out the whole of the density vs axial ratio phase diagram for hard spherocylinders using a combination of simulation and theoretical techniques [79]. It was found that stable smectic and nematic phases only exist for $L/D \geq 3.1$ and $L/D \geq 3.7$ respectively. Moreover, the size of the density jump was seen to diminish at the N-Sm transition with increasing particle length, whereas it increased for the I-N.

Finally, simulations have been carried out on binary mixtures of spherocylinders with different aspect ratios [80], although these have been confined to parallel systems. It was found that the nematic-smectic transition, which is postponed by increasing the length of the longer rod, is eventually preempted by a nematic-columnar transition when the length of the longer rod is increased by a certain amount, showing that in these mixtures bidispersity favours columnar over smectic order.

3.3.1.3 Conclusions

Despite the inherent problems of simulating mesogens, a large number of features have been reproduced using just hard core models. Of particular note is the establishment of a stable smectic phase for systems of sufficiently long spherocylinders, proof that hard core effects are sufficient for the establishment of a variety of mesophases. The next logical step is the consideration of anisotropic particles with more realistic interactions ie soft potentials.

3.3.2 Soft Particle Models

That a realistic interaction has both attractive and repulsive components is evident from the fact that on one hand solids and liquids have the property of cohesion, but at the same time do not collapse indefinitely to a point singularity under the action of these forces. Soft potentials attempt to model this by comprising both a repulsive inner and an attractive outer region. Unlike hard particles, they do not generally have an infinitely repulsive hard core, but rather a steeply rising potential within a certain distance, hence the term soft particle. By far the most commonly used model interaction for atomic systems is the Lennard-Jones potential, given by

$$U_{ij} = 4\epsilon_0 \left[\left(\frac{\sigma_0}{r_{ij}} \right)^{12} - \left(\frac{\sigma_0}{r_{ij}} \right)^6 \right] \tag{3.59}$$

where ϵ_0 is the well depth (ie the strength of the strongest attractive interaction) and σ_0 the collision diameter (the distance at which the potential between two particles is zero). The repulsive $\left(\frac{\sigma_0}{r_{ij}} \right)^{12}$ term comes from the overlap of the electron shells, and should really be exponential. However the former is more convenient to use and gives approximately the same interaction. The attractive $\left(\frac{\sigma_0}{r_{ij}} \right)^6$ term arises from, amongst other factors, the induced dipole-dipole interactions. This potential has proved exceedingly successful at reproducing real behaviour for a number of atomic systems, given an appropriate choice of the two parameters. In computer simulations of anisotropic molecules, an atomistic model would involve designating several Lennard-Jones potentials to each molecule in an attempt to accurately reproduce the intermolecular interactions. Although this technique has been used [81] with

some success recently in the liquid crystal field, it will not be discussed here since this work is concerned solely with the use of single site anisotropic potentials.

The need to make efficient use of computational power has resulted in a number of attempts, since the beginnings of computer simulation, to effectively model a site-site potential with a single site interaction. This alternative type of potential was first introduced in 1948 by Corner [82], who proposed a numerical fit to a multi site Lennard-Jones potential with orientationally dependent range and energy parameters. Other potentials have been since been proposed [83] - here we will be concentrating on the Gay-Berne potential used in this work, and first, its predecessor, the Berne-Pechukas potential.

3.3.2.1 Berne-Pechukas Potential

The Berne-Pechukas potential [49] is essentially an axially symmetric Gaussian overlap model generalised to a Lennard-Jones form. The basic potential acting between the two molecules is given by the Lennard-Jones interaction(3.59), with the angular dependence of σ determined by the overlap of two axially symmetric Gaussian functions,

$$\sigma(\hat{\mathbf{u}}_i, \hat{\mathbf{u}}_j, \hat{\mathbf{r}}_{ij}) = \sigma_0 \left[1 - \frac{1}{2}\chi \left\{ \frac{(\hat{\mathbf{r}}_{ij} \cdot \hat{\mathbf{u}}_i + \hat{\mathbf{r}}_{ij} \cdot \hat{\mathbf{u}}_j)^2}{1 + \chi(\hat{\mathbf{u}}_i \cdot \hat{\mathbf{u}}_j)} + \frac{(\hat{\mathbf{r}}_{ij} \cdot \hat{\mathbf{u}}_i - \hat{\mathbf{r}}_{ij} \cdot \hat{\mathbf{u}}_j)^2}{1 - \chi(\hat{\mathbf{u}}_i \cdot \hat{\mathbf{u}}_j)} \right\} \right]^{-\frac{1}{2}} \quad (3.60)$$

where χ is a parameter determined by the length of the major and minor axes of the anisotropic particle ie the shape anisotropy $\frac{\sigma_s}{\sigma_e}$:

64

$$\chi = \frac{(\sigma_e/\sigma_s)^2 - 1}{(\sigma_e/\sigma_s)^2 + 1}.$$ (3.61)

The energy parameter is also dependent upon χ, and is given by

$$\epsilon(\hat{\mathbf{u}}_i, \hat{\mathbf{u}}_j) = \epsilon_0 \left[1 - \chi^2 (\hat{\mathbf{u}}_i \cdot \hat{\mathbf{u}}_j)^2 \right]^{-\frac{1}{2}}.$$ (3.62)

σ_0 and ϵ_0 are constants and $\hat{\mathbf{u}}_i$ and $\hat{\mathbf{u}}_j$ are unit vectors describing the orientation of the molecules. When the above orientation-dependent parameters are inserted in the Lennard-Jones potential, one obtains the Berne-Pechukas potential.

$$U(\hat{\mathbf{u}}_i, \hat{\mathbf{u}}_j, \hat{\mathbf{r}}_{ij}) = 4\epsilon(\hat{\mathbf{u}}_i, \hat{\mathbf{u}}_j) \left[\left(\frac{\sigma(\hat{\mathbf{u}}_i, \hat{\mathbf{u}}_j, \hat{\mathbf{r}}_{ij})}{r_{ij}} \right)^{12} - \left(\frac{\sigma(\hat{\mathbf{u}}_i, \hat{\mathbf{u}}_j, \hat{\mathbf{r}}_{ij})}{r_{ij}} \right)^6 \right].$$ (3.63)

This model was first studied by Kushick and Berne [84] using constant temperature MD in both two and three dimensions. They applied an electric field to the isotropic phase, promoting orientational order, and then monitored the system after the field had been switched off. It proved easy to generate order by imposing an external field. However the establishment of stable orientational order in the absence of a field proved to be difficult, and any observed order was lost after sufficiently long simulations.

The Berne-Pechukas potential suffers from some unrealistic features. Firstly, the strength parameter does not depend on the intermolecular vector $\hat{\mathbf{r}}$, resulting in an equal interaction for configurations in which molecules are placed side-by-side

and end-to-end, whereas one would expect a stronger interaction for the former. Secondly, the r -dependence scales as σ, which results in an overestimation of the width of the attractive well for those configurations in which σ is large [85].

3.3.2.2 Gay-Berne Potential

Gay and Berne [7] addressed the problems of the Berne-Pechukas potential by comparing it with the interaction between two molecules each composed of a line of four Lennard-Jones atoms. To enable meaningful comparison, the potentials were normalised so that the well depth of the side-by-side configurations were unity. Under these conditions, they confirmed that the two unrealistic features mentioned above are indeed the main discrepancies between the Berne-Pechukas and the site-site potential. For the Lennard-Jones array, the side-by-side well depth is much deeper (approx 5 times) than the end-to-end well depth, whereas the Berne-Pechukas potential has the two equal. Also, the site-site potential has well widths approximately independent of orientation, while in the Berne-Pechukas potential it is closely proportional to σ.

In order to rectify these unusual features, Gay and Berne proposed two modifications. First, a new strength parameter depending explicitly on $\hat{r}$ is defined:

$$\epsilon(\hat{\mathbf{u}}_i, \hat{\mathbf{u}}_j, \hat{\mathbf{r}}_{ij}) = \epsilon_0 \epsilon_1^\nu(\hat{\mathbf{u}}_i, \hat{\mathbf{u}}_j) \epsilon_2^\mu(\hat{\mathbf{u}}_i, \hat{\mathbf{u}}_j, \hat{\mathbf{r}}_{ij}) \tag{3.64}$$

where $\epsilon_1(\hat{\mathbf{u}}_i, \hat{\mathbf{u}}_j)$ is the strength parameter given in the Berne-Pechukas potential (3.62) and $\epsilon_2(\hat{\mathbf{u}}_i, \hat{\mathbf{u}}_j, \hat{\mathbf{r}}_{ij})$ is a function taking the same form as the Berne-Pechukas

$\sigma(\hat{\mathbf{u}}_i, \hat{\mathbf{u}}_j, \hat{\mathbf{r}}_{ij})$ term (Eqn 3.60),

$$\epsilon_2(\hat{\mathbf{u}}_i, \hat{\mathbf{u}}_j, \hat{\mathbf{r}}_{ij}) = 1 - \frac{1}{2}\chi' \left\{ \frac{(\hat{\mathbf{r}}_{ij} \cdot \hat{\mathbf{u}}_i + \hat{\mathbf{r}}_{ij} \cdot \hat{\mathbf{u}}_j)^2}{1 + \chi'(\hat{\mathbf{u}}_i \cdot \hat{\mathbf{u}}_j)} + \frac{(\hat{\mathbf{r}}_{ij} \cdot \hat{\mathbf{u}}_i - \hat{\mathbf{r}}_{ij} \cdot \hat{\mathbf{u}}_j)^2}{1 - \chi'(\hat{\mathbf{u}}_i \cdot \hat{\mathbf{u}}_j)} \right\} \qquad (3.65)$$

where

$$\chi' = \frac{(\epsilon_s/\epsilon_e)^{1/\mu} - 1}{(\epsilon_s/\epsilon_e)^{1/\mu} + 1} \qquad (3.66)$$

Here $\frac{\epsilon_s}{\epsilon_e}$ is the relative strength of the side-side to the end-end attractive interaction. Thus the anisotropy in the well depth is explicitly included in a phenomenological way. The exponents μ and ν can be varied to give a wide range of anisotropic potentials. In their work Gay and Berne found good agreement to the Lennard-Jones array by using $\mu = 2$ and $\nu = 1$.

The second modification involves a new dependence on the Berne-Pechukas $\sigma(\hat{\mathbf{u}}_i, \hat{\mathbf{u}}_j, \hat{\mathbf{r}}_{ij})$ (Eqn 3.60), which ensures that the potential is now being displaced rather than dilated. The final form reads as follows

$$U(\hat{\mathbf{u}}_i, \hat{\mathbf{u}}_j, \hat{\mathbf{r}}_{ij}) = 4\epsilon(\hat{\mathbf{u}}_i, \hat{\mathbf{u}}_j, \hat{\mathbf{r}}_{ij}) \left[\left(\frac{\sigma_0}{r_{ij} - \sigma(\hat{\mathbf{u}}_i, \hat{\mathbf{u}}_j, \hat{\mathbf{r}}_{ij}) + \sigma_0} \right)^{12} - \left(\frac{\sigma_0}{r_{ij} - \sigma(\hat{\mathbf{u}}_i, \hat{\mathbf{u}}_j, \hat{\mathbf{r}}_{ij}) + \sigma_0} \right)^6 \right]$$
$$(3.67)$$

Evidently, the Gay-Berne model is still computationally much cheaper than its site-site counterpart. It should be noted that in the limit $\kappa = \kappa' = 1$ ($\kappa = \sigma_s/\sigma_e$, the shape anisotropy parameter; $\kappa' = \epsilon_s/\epsilon_e$, the well depth anisotropy parameter) the

spherical Lennard-Jones potential is recovered. In this sense the potential can be regarded as a generalisation of the Lennard-Jones interaction to anisotropic systems.

The Gay-Berne model has been widely studied in a number of parameterisations and can be justifiably regarded as one of the most important anisotropic potentials in use at present. The first parameterisation suggested for the model was in the original work by Gay and Berne [7], who found satisfactory agreement to the 4 site linear Lennard-Jones array using the parameters $\kappa = 3.0, \kappa' = 5.0, \mu = 2, \nu = 1$. The dependence of this potential on intermolecular separation in the four main limiting configurations (Fig 3.1) is given in Fig 3.2; the potential varies smoothly between these limiting behaviours for the intermediate configurations which occur in real simulations. The graph clearly shows that the side-side interaction is the most attractive; along with the end-end interaction it is this which promotes mesophase formation.

| Side-Side | End-End | Tee | Cross |
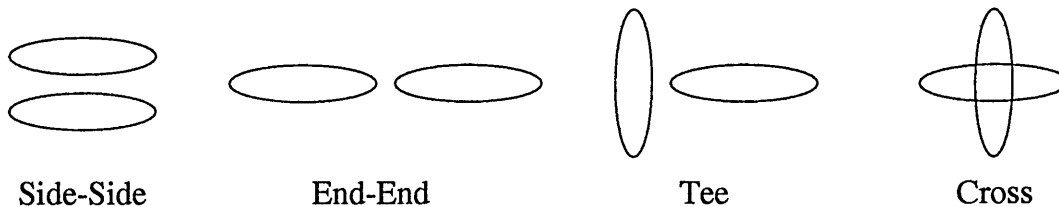
Figure 3.1: The four main relative molecular configurations for the GB model.

Using this parameterisation, Adams et al [86] successfully demonstrated a spontaneous isotropic-nematic transition for $\rho^* = 0.32$ and $1.7 \leq T^* \leq 1.8$, using MD in the NVT ensemble. They did this by observing the second rank order pair correlation function and the radial distribution function.

Further simulations [87] were carried out using different exponents ($\mu = 1, \nu =$
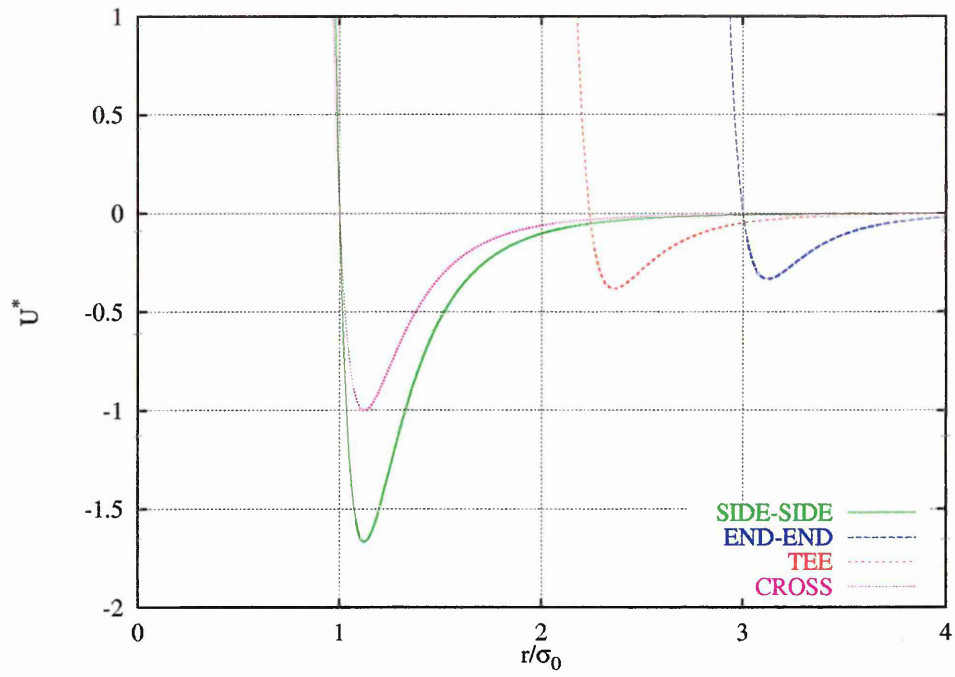
Figure 3.2: GB well depths - $(\kappa = 3.0, \kappa^{'} = 5.0, \mu = 2.0, \nu = 1.0)$
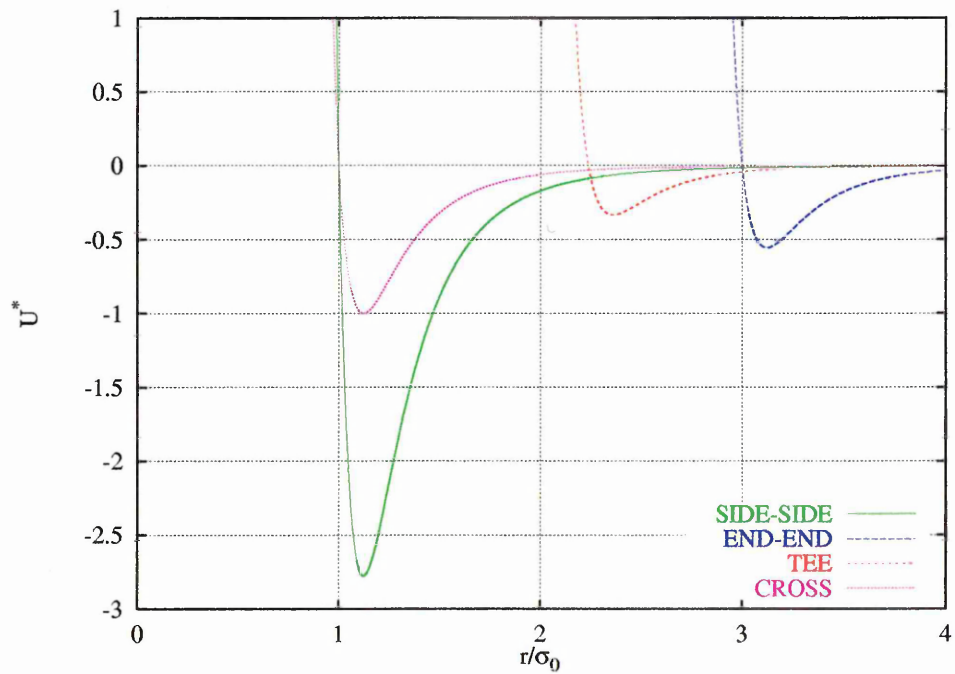
Figure 3.3: GB well depths - $(\kappa = 3.0, \kappa^{'} = 5.0, \mu = 1.0, \nu = 2.0)$

69

2), to promote mesophase formation. This parameterisation has deeper (ie more attractive) parallel well-depths (ie. side-side and end-end) (See Fig 3.3) than the original GB, and using it isotropic, nematic, smectic-A, smectic-B and crystal phases were observed. The phases were identified using computer graphics to visualise configurations taken from the production stage of the simulations and by monitoring the orientational order parameter. In this paper an important point was made about the shape of the Gay Berne model. By looking at the contour corresponding to a change of potential energy from positive to negative, the potential was found to be essentially ellipsoidal in shape, and thus incapable of forming a smectic phase according to earlier hard particle simulations. However, as would be expected, the strong side-by-side interactions stabilise the smectic phase allowing one to be observed.

An attempt [47] has been made to model a real system with the Gay Berne potential, namely the mesogen p-terphenyl, which was chosen because of its rigidity and non polar characteristics. The total pair potential of the real molecule was constructed from a summation of Lennard-Jones site-site terms, each molecule having 32 sites and the central aromatic ring being twisted by 36 degrees with respect to the coplanar end rings. As with the original Gay Berne fitting (to arrays of 4 LJ sites), the new parameters were chosen from comparisons with various biaxially averaged contours and the movement of one molecule around another. The final Gay Berne parameters obtained by this mapping were: $\kappa = 4.4, \kappa' = 39.6, \epsilon_0 = 4302K, \mu = 0.8, \nu = 0.74$. The resulting repulsive core is more elongated in shape and the well depth anisotropy is significantly greater than the original Gay Berne value of 5.

Preliminary investigations of this parameterisation successfully identified isotropic, nematic and smectic-A phases. The authors then proceeded to investigate the effect of reducing the well depth anisotropy (κ') using a smectic-A phase as the initial configuration. It was found that the smectic-A order was lost and the system reverted to the nematic phase for a sufficiently small κ'. However, without a full phase diagram, a true evaluation of the newly parameterised Gay Berne potential could not be given.

De Miguel *et al* carried out extensive simulations with the original Gay Berne parameterisation in an attempt to construct an approximate phase diagram for the system. The liquid-vapour region was located using the Gibbs Ensemble MC method [88], the isotropic-nematic transitions by thermodynamic integration [89], and the remaining transitions were determined by observation of specific order parameters along various isotherms [90, 91].

Chalam *et al* [90] studied the system size dependence of the Gay Berne model with regard to the isotropic-nematic region and found there was a slight shift ($\sim 1\%$) in the transition density and pressure as the number of molecules was increased by a factor of approximately 2 ($N = 256$ to $N = 500$).

It should be noted that all of the above simulations (with the exception of the Gibbs Ensemble MC) were performed using the molecular dynamics technique, which seems to have been more successful with anisotropic systems. However some work [92] has been done using MC on the Gay Berne model with a parameterisation devised so as to enhance the parallel interactions (ie those involved in mesophase formation) $\mu = 1, \nu = 3$. Systems of both 512 and 1000 particles were studied, and it was found that

exceptionally long runs were required to achieve reliable results, especially around the transition regions, due to the very long range fluctuations inherent in these systems. Isotropic, nematic and smectic phases were observed, and the isotropic-nematic transition was found to be more strongly first order as compared with the standard ($\mu = 2, \nu = 1$) potential. A noticeable shift (a few percent) in the isotropic-nematic transition temperature with change in system size was also seen.

Recently, more comprehensive studies of the phase diagram for the original Gay Berne parameterisation and systematic perturbations from it have been conducted. These have concentrated upon the effect that changes in the molecular elongation [93] and well depth parameters [94] have upon the overall phase behaviour of the system. Particular attention was paid to the Vapour-Isotropic (V-I) region (as observed earlier by De Miguel *et al*) and the effect of different parameterisations upon this. A slight discrepancy was found with these earlier results and a modified phase diagram for the original parameterisation determined (Fig: 3.4).

Considering changes to the original parameterisation, it was found that on increasing the molecular elongation parameter κ, the V-I region disappears since the smectic phase is stabilised (ie occurs at a lower density) and thus is preferred to the isotropic region. The nematic phase still occurs at too high a temperature for any vapour nematic (V-N) coexistence to occur, although it too is shifted to lower densities. This stabilisation of the ordered phases is to be expected since increasing κ results in deeper well depths for parallel configurations of molecules (Fig 3.5), making them energetically more favourable.

The well depth anisotropy parameter κ' was also found to have a significant effect.
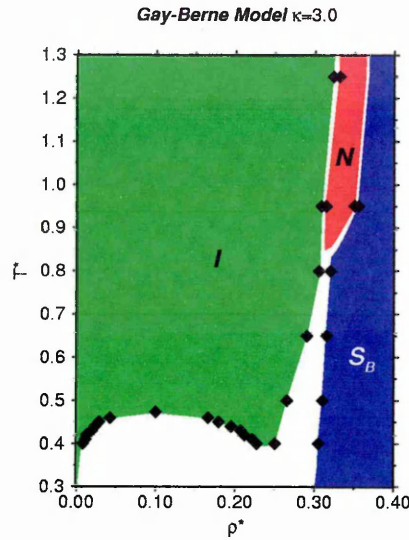
Figure 3.4: Temperature-density phase diagram for GB model [93]
$\left(\kappa = 3.0, \kappa^{'} = 5.0, \mu = 2, \nu = 1\right)$

Increasing values destabilise the nematic phase with respect to the smectic phase at a given temperature, and shift the density at which the smectic phase occurs down slightly. This is because $\kappa^{'}$ governs the relative strength of the side-side and end-end well depths, which control the degree of layering in orientationally ordered systems. Concentrating on the low $\kappa^{'}$ case, it was found that decreasing values shift the I-V coexistence region upwards. This is to be expected since lower values involve stronger overall attractive interactions, due to the increasing end-end well-depth. Combined with the stabilisation of the nematic phase as described above, this leads to a window of stable V-N coexistence for $1.25 \geq \kappa^{'} \geq 1.0$. The well-depths for the $\kappa^{'} = 1.0$ case are shown in Fig 3.6.

In summary, the GB potential has shown a reasonable degree of success in displaying a variety of mesophases. Unfortunately it does not capture the fine detail inherent in real molecules and thus cannot display some of the more subtle liquid crystal
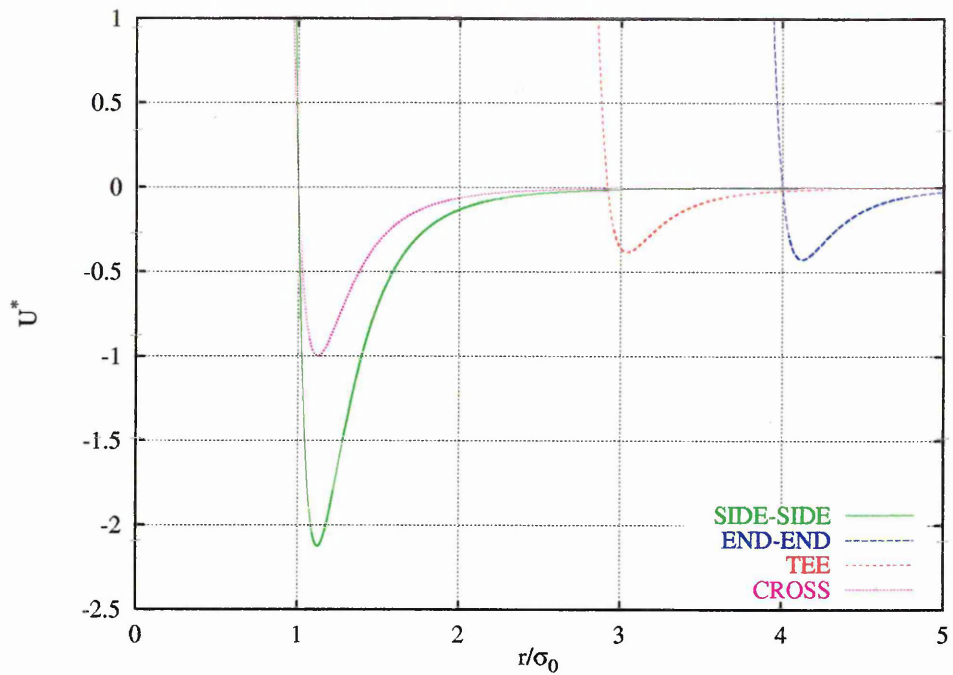
Figure 3.5: GB well depths - $(\kappa = 4.0, \kappa' = 5.0, \mu = 2.0, \nu = 1.0)$
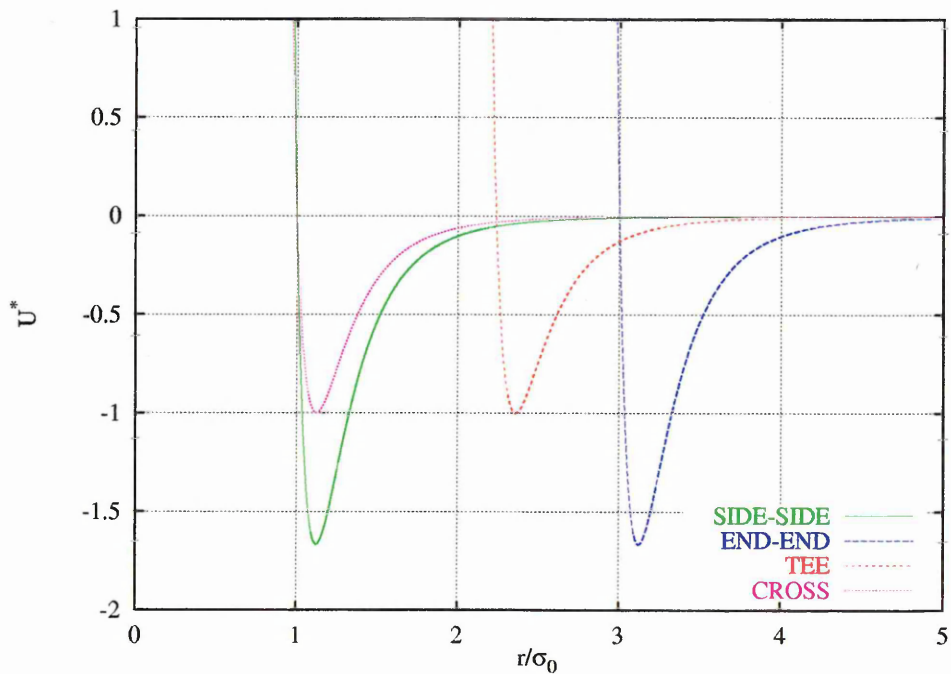
Figure 3.6: GB well depths - $(\kappa = 3.0, \kappa' = 1.0, \mu = 2.0, \nu = 1.0)$

features, such as conformational changes within the molecules themselves, or bulk tilted ordering. However its computational simplicity and large parameter space make it particularly attractive to the simulator, since it can access the time and length scales required for mesophase ordering, and can be readily adjusted to model a particular type of behaviour. In recent years, this simplicity, combined with rapidly increasing computational power, has enabled the simulation of more complicated Gay Berne systems, such as mixtures and at interfaces. Studies of these will now be considered.

3.3.2.3 Soft Particle Mixtures

To date, computer simulations of liquid crystal mixtures with attractive interactions have been very limited. Some lattice based simulations have been attempted, such as the MC investigation of a binary mixture of cylindrically symmetric nematogens by Hashim *et al* [95]. Using a simple anisotropic interaction between nearest neighbours and a low concentration of longer rods to facilitate equilibration they attempted a comparison with an earlier developed molecular field approximation (The Humphries-James-Luckhurst theory) [96]. It was found that the addition of the longer rods stabilised the nematic phase, as predicted. However the theory overestimated the actual transition temperatures, as with other molecular field theories for one component systems.

Apart from lattice simulations, however, there have been very few simulations of liquid crystal mixtures with attractive interactions. Part of the problem is the requirement of a realistic potential to properly mimic the interactions between two

different anisotropic molecules. An attempt has recently been made to use the Gay-Berne potential to simulate an LC mixture [97], using different parameters for each molecule and a set of parameters derived using the Lorentz-Berthelot mixing rule for the unlike interactions. This study used the standard MC technique and the monitoring of various structural and orientational functions to determine the existence of any mesophases. The authors reported a smectic phase and suggested some demixing for certain parameters. However the validity of their results must be called into question, since the unmodified Gay-Berne potential is unsuitable for mixtures due to its inability to distinguish between the two different T-configurations (Fig 3.7) possible for unlike molecules; ignoring this broken symmetry results in a potentially significant break with reality.
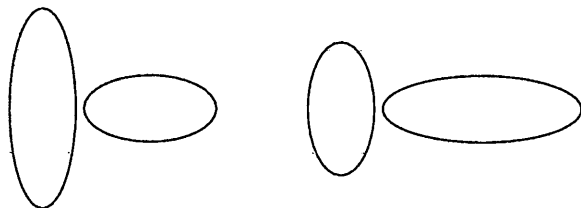
Figure 3.7: Tee Configurations for two unlike GB particles.

A recent paper by Cleaver *et al* [98] has proposed a generalised form of the Gay-Berne potential for the interaction between unlike mesogens which does distinguish between the two different T-configurations. This is achieved by extending the range parameter function, on which the shape of the Gay-Berne potential is based, to incorporate mixed interactions, and then importing it into the standard Gay-Berne form to provide an explicit interaction potential. The new range parameter function is given by

$$\sigma(\hat{\mathbf{u}}_i, \hat{\mathbf{u}}_j, \hat{\mathbf{r}}_{ij}) = \sigma_0 \left[1 - \frac{1}{2}\chi \left\{ \frac{(\alpha\hat{\mathbf{r}}_{ij} \cdot \hat{\mathbf{u}}_i + \alpha^{-1}\hat{\mathbf{r}}_{ij} \cdot \hat{\mathbf{u}}_j)^2}{1 + \chi(\hat{\mathbf{u}}_i \cdot \hat{\mathbf{u}}_j)} + \frac{(\alpha\hat{\mathbf{r}}_{ij} \cdot \hat{\mathbf{u}}_i - \alpha^{-1}\hat{\mathbf{r}}_{ij} \cdot \hat{\mathbf{u}}_j)^2}{1 - \chi(\hat{\mathbf{u}}_i \cdot \hat{\mathbf{u}}_j)} \right\} \right]^{-\frac{1}{2}}$$

$$(3.68)$$

where

$$\chi = \sqrt{\frac{(l_i^2 - d_i^2)(l_j^2 - d_j^2)}{(l_j^2 + d_i^2)(l_i^2 + d_j^2)}} \tag{3.69}$$

and

$$\alpha^2 = \sqrt{\frac{(l_i^2 - d_i^2)(l_j^2 + d_i^2)}{(l_j^2 - d_j^2)(l_i^2 + d_j^2)}} \tag{3.70}$$

where i and j are the two different anisotropic particles.

A modified strength anisotropy term also needs to be introduced else the well depths for the two T-configurations would be equal. By reference to the shape parameter result the functional form

$$\epsilon_2(\hat{\mathbf{u}}_i, \hat{\mathbf{u}}_j, \hat{\mathbf{r}}_{ij}) = 1 - \frac{1}{2}\chi' \left\{ \frac{(\alpha'\hat{\mathbf{r}}_{ij} \cdot \hat{\mathbf{u}}_i + \alpha'^{-1}\hat{\mathbf{r}}_{ij} \cdot \hat{\mathbf{u}}_j)^2}{1 + \chi'(\hat{\mathbf{u}}_i \cdot \hat{\mathbf{u}}_j)} + \frac{(\alpha'\hat{\mathbf{r}}_{ij} \cdot \hat{\mathbf{u}}_i - \alpha'^{-1}\hat{\mathbf{r}}_{ij} \cdot \hat{\mathbf{u}}_j)^2}{1 - \chi'(\hat{\mathbf{u}}_i \cdot \hat{\mathbf{u}}_j)} \right\}$$

$$(3.71)$$

is suggested which is combined with the other standard Gay-Berne expressions

$$\epsilon_1(\hat{\mathbf{u}}_i, \hat{\mathbf{u}}_j) = \left[1 - \chi^2(\hat{\mathbf{u}}_i \cdot \hat{\mathbf{u}}_j)^2\right]^{-\frac{1}{2}} \tag{3.72}$$

$$\epsilon(\hat{\mathbf{u}}_i, \hat{\mathbf{u}}_j, \hat{\mathbf{r}}_{ij}) = \epsilon_0 \epsilon_1^\nu(\hat{\mathbf{u}}_i, \hat{\mathbf{u}}_j) \epsilon_2^\mu(\hat{\mathbf{u}}_i, \hat{\mathbf{u}}_j, \hat{\mathbf{r}}_{ij}) \tag{3.73}$$

to give the generalised Gay-Berne interaction,

$$U(\hat{\mathbf{u}}_i, \hat{\mathbf{u}}_j, \hat{\mathbf{r}}_{ij}) = 4\epsilon(\hat{\mathbf{u}}_i, \hat{\mathbf{u}}_j, \hat{\mathbf{r}}_{ij}) \left[\left(\frac{\sigma_0}{r_{ij} - \sigma(\hat{\mathbf{u}}_i, \hat{\mathbf{u}}_j, \hat{\mathbf{r}}_{ij}) + \sigma_0} \right)^{12} - \left(\frac{\sigma_0}{r_{ij} - \sigma(\hat{\mathbf{u}}_i, \hat{\mathbf{u}}_j, \hat{\mathbf{r}}_{ij}) + \sigma_0} \right)^{6} \right] \tag{3.74}$$

The question of relating the parameters $\epsilon_0, \mu, \nu, \chi'$ and α' to the system of interest is rather less clear cut than it is for the parameters associated with the shape parameter, and the authors suggest it should be considered afresh for each system used.

This potential has already been used to investigate the phase behaviour of a bidisperse system (50:50 mixture) of rod-like mesogens with axial ratios $l/d = 3.5$ and $l/d = 3.0$ [99]. Using the molecular dynamics technique in the NVE ensemble, it was found that this slight bidispersity (from the difference in rod lengths) significantly stabilises the nematic region with respect to that of the corresponding pure systems, and that, as predicted by mean field theory, the longer rods are always more ordered than the shorter ones.

78

3.3.2.4 Conclusions

In summary, the simulation of realistic anisotropic systems is clearly still in its infancy, and a lot of progress is yet to be made. Although the development of analytical expressions for the interaction between mesogens has been a significant step forward, there still remains the problem of relating these model interactions to real molecules, where there are a number of different factors having an effect (eg polarisability, flexibility) which are still very difficult to simulate effectively.

Where computer simulation has been successful is in determining the effects of small perturbations away from ideal behaviour, such as in investigating the effect of adding attractive interactions to hard particles. Although, strictly speaking, soft particles do not have a hard core, they still have a central region into which it is very difficult for other molecules to penetrate, and as such are comparable to a hard core with attractive interactions. The immediate future of simulation is in investigating the effects of changes in these models systematically, and with regard to this the development of the Generalised Gay-Berne potential has been important in that it now allows the study of deviations from pure systems ie mixtures. It also opens up the possibility of multi-anisotropic-site systems, which should lead to closer approximation to real molecules. Certainly the scope of soft particle anisotropic systems is huge, and there are many different aspects still to be studied.

3.3.3   Interfacial Simulations

Although the principal techniques for simulating an interface are the same as for simulating homogeneous phases, the time required to calculate key interfacial properties, such as the density profile and the surface tension, is significantly longer than for a bulk fluid. It is for this reason that simulations of inhomogeneous systems have lagged behind those of bulk systems.

There is however a plethora of work in the literature on the liquid-vapour interface of the simple Lennard-Jones model, dating back some 20 years [100]. These simulations have used the MC and MD techniques on systems consisting of either a central liquid slab flanked by two vapour regions, or a liquid region abutting a homogeneous wall on one side and in coexistence with a vapour region on the other. They have shown studying coexistence with interfaces to be tractable and have produced good agreement with the coexisting densities and energies predicted by other simulation techniques. However, there are numerous discrepancies in the values of key interfacial properties, in particular the surface tension. A recent review [100] of this body of work concluded that interfacial systems are much more sensitive to the effects of simulation parameters, especially the potential cut-off, and that particular care must be taken in ensuring that the simulations are properly equilibrated. Studies of multi-site LJ models at the free interface in an attempt to model the surface tension of chlorine and hexane [101] have shown good agreement with experimental results, indicating the direct simulation method to be capable of producing accurate phase equilibria for molecular liquids providing sufficient care is taken.

The literature contains relatively few simulation studies of interfacial liquid crys-

talline systems. This is to be expected, since the presence of orientational ordering will introduce the need for even longer run times. The lattice based Lebwohl-Lasher (L-L) model has been used to investigate the suppression of the nematic-isotropic transition. Luckhurst and coworkers [102] have studied the surface properties of a thin liquid crystal film by Monte Carlo simulations. They used a L-L system of $10 \times 10 \times 10$ sites and applied periodic boundary conditions in just two dimensions, thus forming two free surfaces orthogonal to the third dimension. They found a very small downward shift in the nematic-isotropic transition temperature (T_{NI}) over the bulk value (due to the effect of free surfaces and perhaps a smaller system size), and also an isotropic phase adsorbed on the surface when there is a bulk nematic phase in the centre of the pore. Cleaver and Allen [103] then considered the nature of the shifted bulk transition in a L-L slab with N parallel planes, subject to a non-zero surface field, using MC simulation. They reported a critical thickness, $8 < N_c < 16$, below which there was no bulk transition for the case of zero surface field i.e. a free surface. It was concluded that the cause of this critical point was related to the pretransitional divergence in orientational correlations at the bulk transition, explaining the failure of mean field theories - which underestimate the effects of correlations - to predict this critical point.

The work described above offered a useful comparison with the early theoretical work on confined liquid crystals, but the system's simplicity (no density variation or spatial disorder is incorporated) renders it unable to model details of the interfacial structure. Specifically, the competing effects of surface packing density and orientation are not incorporated, and so there is no possibility of observing tilted interfacial layers. To enable these requires an off lattice model, such as the Gay-Berne, at ei-

81

ther a free surface or interacting with a wall with an appropriate particle-substrate interaction.

Recently there have been a number of such more realistic simulations. The free-surface types will be considered first, followed by simulations of interfaces between two liquid phases, and finally substrate systems will be discussed.

The first free-surface work looked at an isotropic GB fluid in coexistence with its own vapour [104], based upon the results of some earlier Gibbs ensemble simulations [88]. It was found that, as the temperature was lowered towards the vapour-isotropic-smectic triple point, the molecules at the interfaces tended to orientate themselves homeotropically, whilst the bulk of the fluid remained isotropic. This nematic wetting was important, but unfortunately this particular GB parameterisation did not exhibit nematic-vapour coexistence, and further cooling was not conducted due to the intractable run times needed to properly study any smectic coexistence.

Lately, two independent groups [105, 106] have simulated a stable nematic-vapour system, using a different parameterisation of the GB potential, which had again previously been shown to display bulk nematic-vapour coexistence using the Gibbs ensemble technique [94]. Both groups found that, for this system, the free interfaces enhance orientational order and induce a director lying in a plane parallel to the interface. Upon cooling through the isotropic-nematic transition, a surface tension trend consistent with theoretical and experimental observations for nematic wetting was observed, and the adoption of nematic ordering parallel to the interface across the whole of the film was observed. However, it was suggested that this order did not grow in from the interfaces, as might be expected, but arose from orientational

82

fluctuations within the middle of the film.

Two brief investigations into the interfacial ordering between an isotropic GB fluid and, respectively, its nematic [107] and smectic [108] phases have been published. Two different parameterisations were used, the first having been studied previously in a published bulk study [92] discussed earlier and the second being a modified version of a parameterisation obtained from comparison to a realistic mesogenic fragment [47]. These investigations used a questionable thermostating technique to maintain the stability of the two phases, by setting the temperature to be different in two regions of the simulation box. Although this might cast some doubt over the observed thermodynamic quantities, due to the unrealistic temperature discontinuity at the interface, the induced orientation should be correct. Using again a different parameterisation of the GB potential, it was found that planar ordering was induced at both liquid-crystal-isotropic interfaces, with orientational correlations extending a small way into the isotropic phase. In contrast, for the smectic interface, there was no such effect observed for the translational correlations.

Considering substrate systems, until recently only a brief investigation had been performed [90]. Moreover this employed a molecule-substrate potential which was separable into its angular and spatial parts (i.e. the location of the minimum in this potential was independent of the orientation of the molecule relative to the substrate). This oversimplification precluded the observation of either parallel or tilted layers arising due to competing effects at the interface.

Recently presented simulations of a confined Gay-Berne system, with a *nonseparable* particle substrate interaction potential [109], have confirmed theoretical predictions

83

that suitable tuning of the molecule-surface interaction can lead to a range of different pretilt orientations [110]. However, these simulations concentrated almost exclusively on the effects of particle-substrate coupling on the surface region structure and did not explore any temperature dependent effects arising due to the various degrees of orientational freedom available to the system.

Subsequently, a brief investigation of a similar system has been published [111]. A surface induced smectic-C layering was observed, the intermediate region between this and the bulk being characterised by a high degree of biaxiality. Correspondingly, the director orientation underwent a strong distortion close to the surface. However, this work employed a separable particle-substrate interaction potential and was restricted to a single state point.

A more meticulous study of a confined liquid crystal film has been conducted [112], using a relatively small ($N = 256$) system of GB particles confined between two substrates with a non-separable particle-substrate interaction. It was noted that very long molecular dynamics runs ($\sim$ 500,000 timesteps) were required to bring the system to equilibrium, due to the formation of metastable domains which persisted over several tens of thousands of timesteps. However, by very carefully cooling the system from an isotropic state, both moderate and weak coupling strengths were successfully investigated. It was found that a tilted molecular layer developed at each wall, with the pretilt angle and layer density only very weakly dependent on the temperature as the bulk region was cooled through isotropic and nematic regions. Only at relatively low temperatures, when the bulk region adopted a layered structure, was much effect on the surface layer observed, with the change in pretilt

84

angle being linked to the coupling strength, as would be expected.

This same decoupling between the surface and bulk regions has been observed in Monte Carlo simulations of GB particles, adsorbed on a relatively structured surface parameterised to model graphite [113]. Here it was found that the first layer of molecules align parallel to the substrate, with the second layer perpendicular, poking through the holes in the first layer to 'touch' the graphite. The imposition of a bulk director perpendicular to the second layer (ie parallel to the surface) had no effect upon the orientation of the two surface layers, the intermediate region simply adopting a smooth change in director to link the two limiting orientations. This is in agreement with standard continuum theory often used to model nematics at surfaces, where the director is assumed to smoothly vary throughout a sample. However, the abrupt change between the orientation of the first and second layers clearly contradicts this, a change in director of 90 degrees being observed for one molecular length.

Very recently molecularly thin, confined planar and homeotropically anchored GB films have been studied [114], using grand canonical ensemble Monte Carlo (GCMC) techniques in which the thermodynamic state of the film is determined by the temperature T and the chemical potential μ; chosen so that the corresponding bulk fluid is isotropic. A substrate-particle interaction potential of the GB 12-6 form was developed by considering the interaction between an ellipsoidal film molecule and a spherical wall atom. When planar alignment occured at the surfaces, tilted, perpendicular and finally parallel alignment of molecules in the central region was observed as the wall separation was increased. It was concluded that the molecules in the

contact strata are capable of inducing their own parallel orientation in the central region only if the wall separation is sufficiently large; this effect, not observed in simple fluids was thought to be caused by competition between wall induced orientation and lack of space due to confinement. When the interaction potential was adjusted to support homeotropic surface alignment, a highly ordered, solid-like structure was observed in the contact strata; the inner portion of the film remained isotropic and nearly homogeneous, indicating that the walls were apparently unable to induce a high degree of order in the inner portions of the film beyond the contact layers.

Finally, it is worth considering the pitfalls to avoid when conducting such simulations. These have been highlighted quite successfully, if unintentionally, by another investigation of a confined GB system [115]. Firstly, a rather strange substrate-particle interaction was used where a particle interacts with its own mirror image projected into the plane of the substrate, with a possible fixed orientation. This has two drawbacks, in that the structure of the wall will be continuously changing and that no two molecules in the bulk will see the same structure. Secondly, woefully short MD runs were used (20,000 timesteps) along with very large changes in temperature between each state point, and the consequences of this quenching are all too apparent in the configurations presented, clearly identifiable metastable domains being observed in a number of them. Perhaps the one exception was the set of simulations using perpendicular anchoring, where the structures presented look reasonably free of defects. Here again the surface alignment was seen to propagate into the bulk for the nematic phase, with the smectic director adopting a slight tilt away from this, probably due to the number of layers formed being incommensurate with the box directions originally chosen.

3.3.3.1 Conclusion

The most important point to note from these studies is that subtle changes in the intermolecular potential used can lead to quite noticeable effects in interfacial systems, certainly more so than has been witnessed for bulk systems. This is to be expected since the break in symmetry introduced by a surface means the dependence of the intermolecular interactions upon the relative orientations of the molecules will be even more important. However there is still much to be understood about these effects, and this is before even considering the consequences of molecule substrate interactions, which appear to dominate bulk effects. The work presented in Chapter 5 has focussed on unconfined films in an attempt to contribute further to this understanding.

Chapter 4

Bulk Coexistence

In this chapter, the determination of liquid crystal two-phase coexistence using the Gibbs ensemble technique is presented, concentrating on certain parameterisations of the Gay-Berne model and its generalised form. First will be discussed, in brief, how the parameterisation of the Gay-Berne affects the phase diagram, followed by results from a mono-disperse simulation using a novel parameter set which shows both isotropic and nematic-vapour coexistence. A two component perturbation of this is then considered, results being presented for simulations of the isotropic nematic coexistence region, following description of the generalised Gay-Berne parameterisation derivation for the system studied.

4.1   Single Component Gay-Berne Results

As was discussed in the previous chapter, the Gay-Berne model has been shown to display a wide variety of liquid crystalline phases, and, in a few cases, stable

coexistence between them. These have included isotropic liquid-vapour coexistence with the standard Gay-Berne potential [88, 94], $\kappa = 3.0$, $\kappa' = 5$, $\mu = 2.0$, $\nu = 1.0$, and more recently both liquid and nematic-vapour coexistence [94] using a modified parameterisation $\kappa = 3.0$, $\kappa' = 1.0$, $\mu = 2.0$, $\nu = 1.0$. Upon considering the interactions for various configurations of the two molecules it is found that this parameterisation results in a much weaker side-side interaction. This is thought to destabilise the smectic phase and allow nematic-vapour coexistence to occur. This is consistent with other studies [93] which have shown that upon increasing the length of the Gay-Berne molecule (κ), which makes the side-side interaction even stronger, the smectic phase is further stabilised and eventually occurs at a low enough density to destroy the isotropic-vapour coexistence.

Simulations have been conducted using an alternative version of the Gay-Berne potential, where the exponents have the alternative values $\mu = 1.0$, $\nu = 2.0$ [87]. For a given κ and κ' these give much stronger well depths for parallel configurations ie side-side and end-end, which are thought to stabilise mesophase formation. Although this stronger version of the GB has been shown to be capable of displaying a rich liquid crystalline phase behaviour, it has only been the subject of brief study, and to date no two phase coexistence using exponents other than the standard GB values, $\mu = 2.0$, $\nu = 1.0$, has been seen.

In this work the Gibbs ensemble technique has been used to pinpoint a region of phase coexistence for this stronger version of the Gay-Berne.

4.1.1 Simulation Details

Attempts to find the region of liquid-vapour coexistence were made using the Gibbs ensemble MC technique in a fairly standard way. The simulations were started using two isotropic configurations at low densities running as normal MC in each box. Both were then compressed to a density of 0.1, a value known to be in the coexistence region for other GB systems [94]. The additional Gibbs moves were then switched on and the density in each box monitored to see if phase separation occured. Initially this was done at broadly spaced temperature intervals, the intention being to obtain a more detailed diagram once one temperature at which coexistence was stable had been found.

However, using the standard GB length of 3:1 (full parameterisation being $\kappa = 3.0$, $\kappa' = 5.0$, $\mu = 1$, $\nu = 2$), an unexpectedly strong phase separation was observed below a certain temperature, $T^* \approx 0.7$, leading to the formation of a very dense phase into which it became practically impossible to insert particles. Examination of configuration snapshots for this unequilibrated dense phase showed the presence of layering, and it was reasonable to assume that coexistence between vapour and either a smectic or crystal phase was the stable regime here, although this was impossible to clarify using the Gibbs method. At slightly higher temperatures no coexistence could be established at all, and upon comparison with the results of Brown *et al* [93], it was concluded that the smectic phase was stable at too low a density, destroying any possible simple liquid-vapour coexistence. This can be explained by looking at the relative well-depths in the four limiting configurations of the GB. In the parameterisation used, the side-side interaction is very strong compared to that for

the normal GB, which displays I-V coexistence. Similarly in Brown *et al*'s results, it is an elongated GB again with a strong side-side interaction which shows no I-V coexistence; it seems that this well-depth is particularly important in determining the stability of the smectic phase.

With this in mind, the well-depths of various shortened forms of the stronger GB ($\mu = 1$, $\nu = 2$) were looked at. From these calculations it was found that a shape anisotropy (κ) of 2.0 gave a similar strength of side-side interaction both to that of the standard GB, and the parameterisation $\kappa = 3.0$, $\kappa' = 1.0$, $\mu = 2.0$, $\nu = 1.0$ which has also been shown to display liquid-vapour coexistence. This new potential could thus be reasonably expected to show I-V coexistence. The well depths for this parameterisation are shown in Figure 4.1
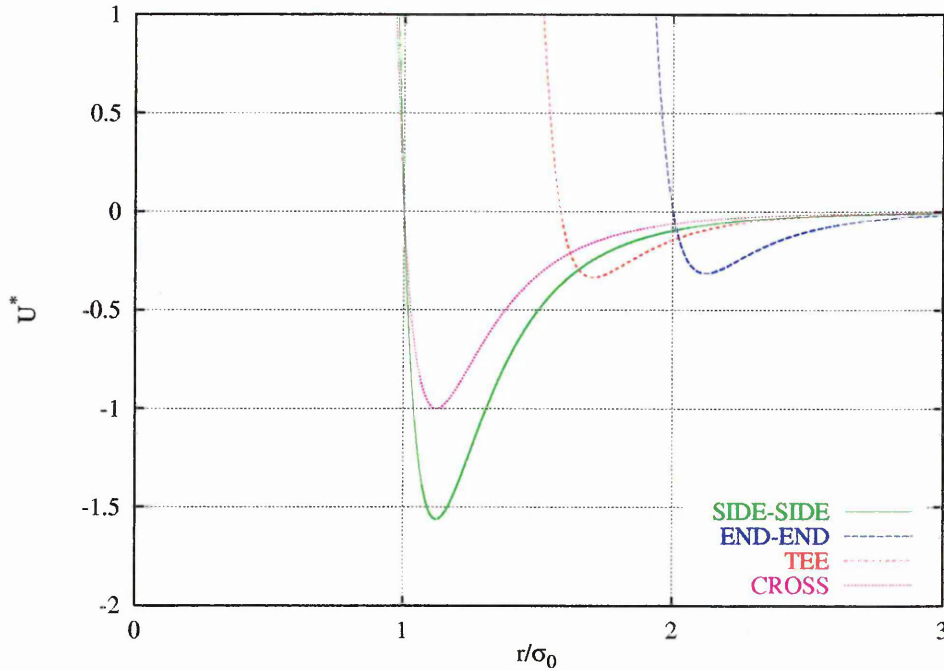

Figure 4.1: GB well depths - ($\kappa = 2.0, \kappa' = 5.0, \mu = 1.0, \nu = 2.0$)

Again, broadly spaced temperature intervals were considered, and this time simple

91

I-V coexistence was observed, for $T^* = 0.56$. Simulations were then conducted at rather smaller temperature intervals below this; sample density evolutions for the two boxes at two temperatures in the isotropic-vapour coexistence region are shown (Fig 4.2)

As can be seen, the values are reasonably stable after as little as 10,000 MC sweeps, and for the isotropic region runs of this length were used as the equilibration period. Average values were then measured for various observables over production runs of 20,000 sweeps, the errors on these averages being estimated by a block averaging technique, with 10 blocks of 2000 sweeps each. Observation of the nematic order parameter P_2 in the region $0.56 \geq T^* \geq 0.485$ showed no indication of orientational order in the dense box, and it was concluded that stable isotropic liquid- vapour coexistence was being observed for these temperatures. However, upon further cooling to $T^* = 0.480$, a relatively large increase in density of the liquid box was observed, with a corresponding increase in the nematic order parameter. The evolution of these two functions from the final configuration of the $T^* = 0.485$ production run is shown (Fig 4.3), together with the density of the vapour box. A significantly longer equilibration run length of 140,000 MC sweeps was required at this lower temperature due to the slow onset of orientational ordering.

Upon further cooling, similar values for ρ^* and P_2 were observed in the liquid box, with an expected slight increase in the density with lowering of temperature. However, no large discontinuities similar to that between $T^* = 0.485, 0.48$ were seen, and it was concluded that a region of stable nematic-vapour coexistence existed in this temperature range. This is confirmed by looking at plots for two structural
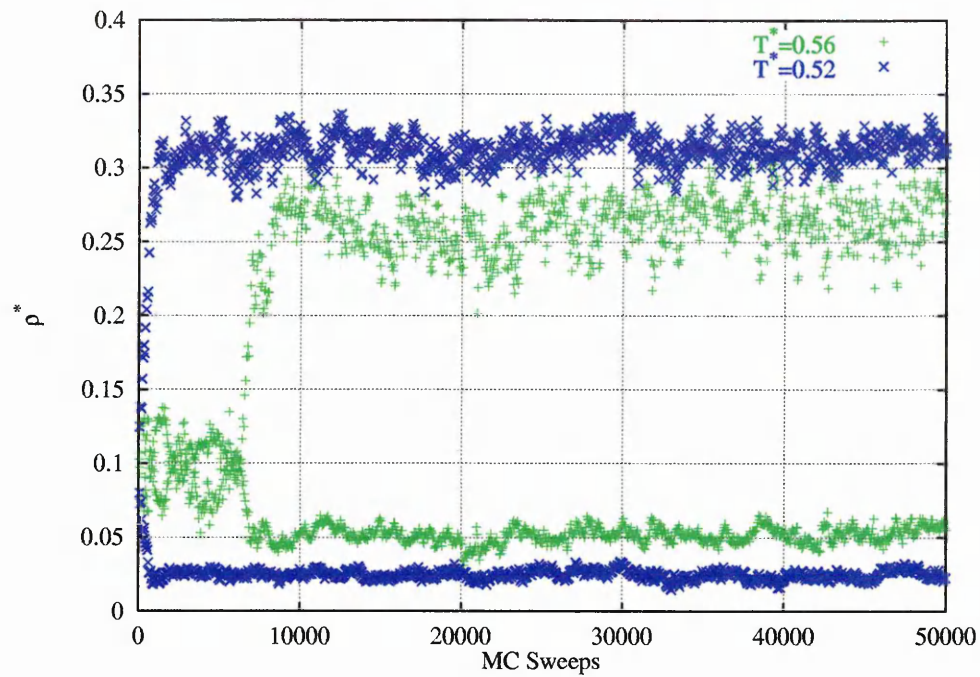
Figure 4.2: Density evolutions for isotropic-vapour coexistence
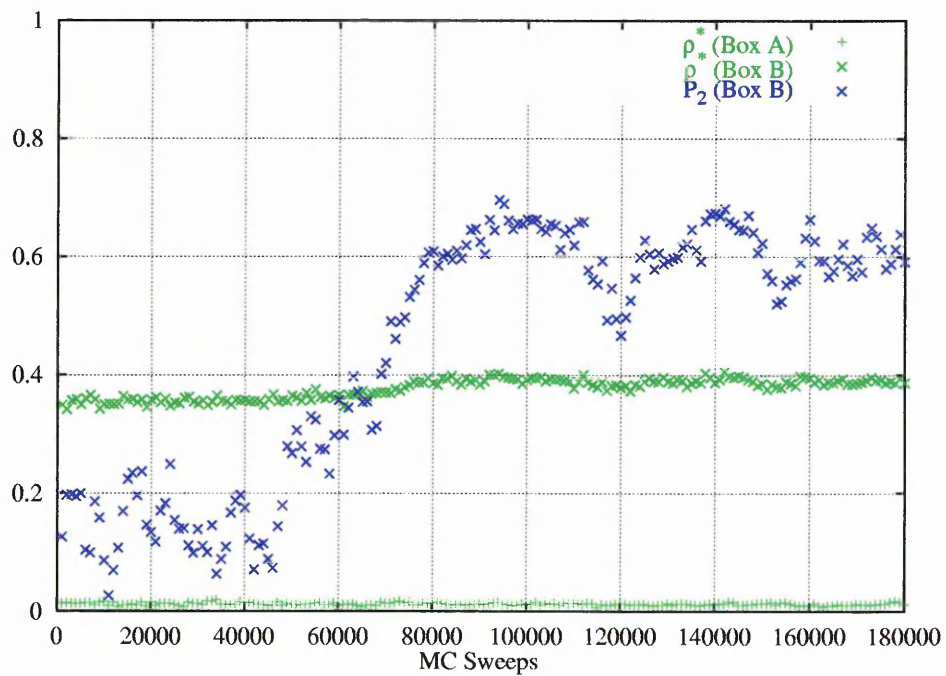

Figure 4.3: Density evolutions and order parameter for $T^* = 0.480$

functions at the temperature $T^* = 0.480$ (Fig 4.4).

The second rank order correlation function, $g_2(r)$, clearly shows a non-zero limiting value, indicative of an orientationally ordered phase. However, the radial distribution function resolved parallel to the director, $g_{par}(r)$, shows no indication of a layered structure, so the ordered phase must be a nematic. (NB - These two functions are formally defined in the following chapter)

Values of various key observables for the cooling runs are presented (Table 4.1), together with the phase diagram in the appropriate temperature-density plane (Fig 4.5).

T^*	$U^*(l)$	$U^*(v)$	$\rho^*(l)$	$\rho^*(v)$	$P^*(l)$	$P^*(v)$	$P_2(l)$
0.560	-2.18(8)	-0.52(4)	0.271(12)	0.045(3)	0.02(2)	0.016(2)	0.090(16)
0.550	-2.32(9)	-0.50(8)	0.288(13)	0.042(5)	0.03(3)	0.015(3)	0.077(17)
0.540	-2.42(2)	-0.39(5)	0.301(02)	0.034(3)	0.03(3)	0.013(2)	0.077(15)
0.530	-2.52(5)	-0.27(3)	0.311(07)	0.025(2)	0.01(3)	0.010(2)	0.097(30)
0.520	-2.65(6)	-0.25(3)	0.326(06)	0.024(2)	0.01(3)	0.009(1)	0.082(22)
0.510	-2.75(4)	-0.21(5)	0.334(04)	0.020(3)	0.00(3)	0.008(1)	0.133(24)
0.500	-2.81(4)	-0.20(3)	0.340(04)	0.017(1)	0.01(2)	0.008(1)	0.090(29)
0.490	-2.94(6)	-0.19(3)	0.351(05)	0.015(1)	0.02(3)	0.006(1)	0.143(33)
0.485	-2.97(6)	-0.16(4)	0.358(06)	0.014(2)	0.01(3)	0.006(1)	0.158(53)
0.480	-3.70(6)	-0.15(3)	0.394(04)	0.012(1)	-0.01(4)	0.005(1)	0.657(29)
0.475	-3.83(9)	-0.14(3)	0.402(05)	0.012(2)	-0.01(5)	0.005(1)	0.686(32)
0.470	-4.00(4)	-0.10(3)	0.409(03)	0.010(1)	-0.01(5)	0.004(1)	0.734(15)

Table 4.1: Observable averages at various temperatures

In addition to measuring the potential energy, U^*, average density, ρ^*, pressure, P^*, and nematic order parameter, P_2, the reduced chemical potential μ^r was also measured, to ensure that the two phases were in chemical equilibrium. This was done using a modified version of the Widom insertion method, the energies calculated for the insertion moves of the Gibbs method used in the expression [116]

94
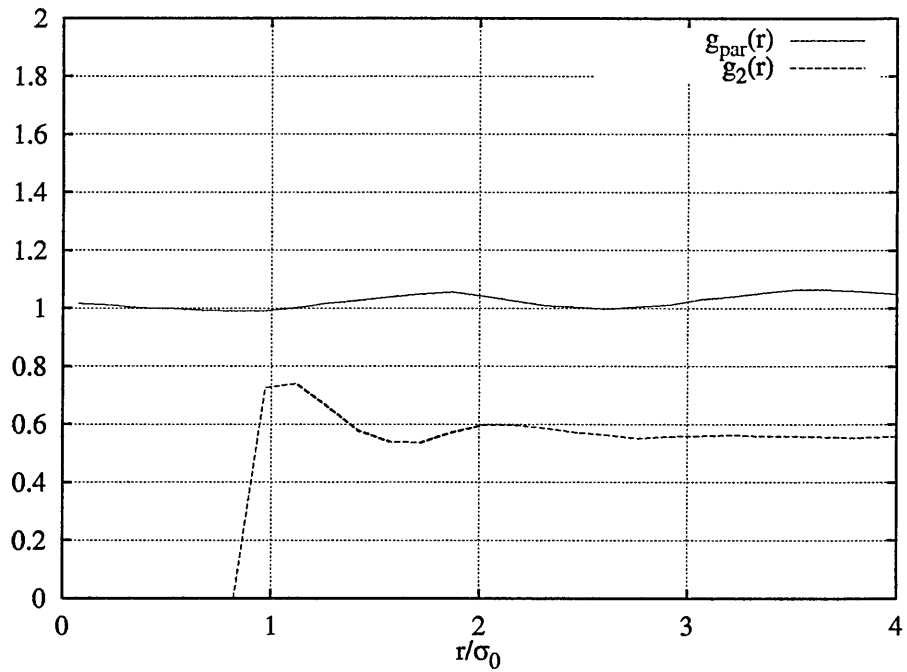
Figure 4.4: Structural functions for $T^* = 0.480$
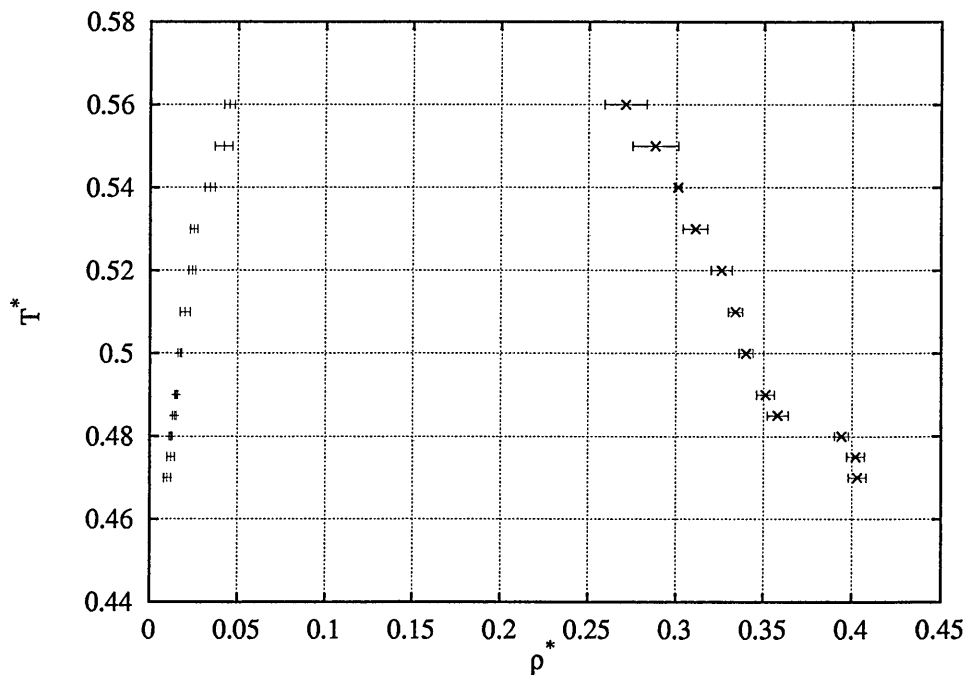
Figure 4.5: $T^* - \rho^*$ phase diagram - liquid vapour region

95

$$\mu_A^r = -k_B T \, ln \left\langle \frac{V_1}{n_A + 1} exp \left[-\frac{U_A^*}{k_B T} \right] \right\rangle_{box\ 1} \tag{4.1}$$

where U_A^* is the energy change for a given insertion, V_1 and n_A the volume of and number of particles in the receiving box at the time, and the angular brackets denote an ensemble (simulation) average. Further details are given in Appendix A. The reduced chemical potential values for each of the phases, along with the particle insertion ratios, p_{ins}, and the number of attempted insertions per cycle, N_{ins}, are shown at various temperatures (Table 4.2). These show, in conjunction

T^*	$\mu^r(l)$	$\mu^r(v)$	p_{ins}	N_{ins}
0.560	-2.16(04)	-2.16(2)	0.0262(72)	200
0.540	-2.13(04)	-2.16(2)	0.0130(63)	400
0.520	-2.16(08)	-2.19(3)	0.0073(12)	600
0.500	-2.13(06)	-2.21(4)	0.0040(08)	1000
0.490	-2.17(06)	-2.21(3)	0.0030(11)	1000
0.485	-2.20(11)	-2.24(5)	0.0009(02)	2000
0.480	-2.14(10)	-2.23(4)	0.0004(02)	10000
0.475	-2.11(17)	-2.25(5)	0.0002(01)	10000
0.470	-2.27(11)	-2.28(4)	0.0001(01)	20000

Table 4.2: Chemical potentials, insertion acceptance rates and attempts

with the pressure values in Table 4.1, that the criteria for chemical, mechanical and thermal equilibrium have been satisfied, each of the two coexisting phases at a given temperature having, to within statistical accuracy, the same pressure and chemical potential.

In previous Gibbs simulations involving relatively dense anisotropic fluids [93, 94], the issue of particle insertion has caused particular problems, with the Gibbs method quickly becoming intractable as the probability of inserting a particle decreases ex-

ponentially towards the triple point. However, for the temperature range studied here, no particle insertion problems were encountered. Down to the lowest temperature, $T^* = 0.470$, insertion success rates of around 0.0001 were observed, which for 20000 attempted insertions per sweep gave approximately 0.4% of the particles transferring at each step. Although this is lower than the original 1-3% suggested by Panagiotopoulos [57], considering the slow timescale of orientational ordering, it seems to be sufficient to ensure equilibrium, as has been noted before [9]. This reasonable success rate is attributed, in part, to the relatively small degree of particle shape anisotropy being used ($\kappa = 2.0$). Upon further cooling, however, the success rate dropped even further and it became too computationally expensive to increase the number of particle insertion attempts sufficiently for equilibrium to be established. The simulations were therefore curtailed at this temperature.

4.2   Generalised Gay-Berne Results

4.2.1   Parameter Fitting

The parameters used in the original Gay-Berne potential were arrived at by comparing the well depths for various configurations with those obtained from two linear arrays of Lennard-Jones sites. One of the advantages of the GB potential is that its four parameters are conceptually easy to understand. Changes to this original parameterisation have been relatively simply implemented, with their effects readily understood, at least on a microscopic interaction level, by comparing the well depths in the four main configurations.

97

However, for the GGB potential [98], the situation is considerably more complicated, there being 4 different parameters, χ, χ', α and α', for each of the four different molecule pairs, ii, jj, ij, ji. Having decided upon the lengths of the two unlike particles, the like-like parameters χ and χ' are given by the explicit definitions in the standard GB, and α and α' are set to one, since they only have a role in unlike pairings. However the relative strength of the two interactions, $\epsilon_{ii}/\epsilon_{jj}$ still needs to be calculated. For the unlike interactions, ij and ji, whilst there are explicit definitions, given in terms of the molecular dimensions, for χ and α, for α' and χ', there are no such expressions, and appropriate values must be arrived at using an alternative, but physically meaningful, method.

In the one previous parameterisation and subsequent simulation using the GGB potential [99], a fitting routine was described which gave the parameter values for a bi-disperse mixture of molecules with $\kappa = 3.0$ and 3.5. Rather than using linear arrays of Lennard-Jones sites, which were remarked upon as introducing an unrealistic odd-even dependency into the interactions, the fitting used the side-side and tee interactions of two Lennard-Jones jellium lines (in the following discussion the subscripts i and j will be used when referring to the GGB particles, A and B for the corresponding jellium lines). The interaction between these is given by

$$U_{AB}^{\mathrm{LJ}} = \varepsilon_0^{\mathrm{LJ}} \int_{\mathbf{r}_B - L_B \hat{\mathbf{u}}_B/2}^{\mathbf{r}_B + L_B \hat{\mathbf{u}}_B/2} \int_{\mathbf{r}_A - L_A \hat{\mathbf{u}}_A/2}^{\mathbf{r}_A + L_A \hat{\mathbf{u}}_A/2} \left(\frac{\sigma_0^{\mathrm{LJ}}}{\left| \mathbf{r}'_A - \mathbf{r}'_B \right|} \right)^{12} - \left(\frac{\sigma_0^{\mathrm{LJ}}}{\left| \mathbf{r}'_A - \mathbf{r}'_B \right|} \right)^{6} d\mathbf{r}'_A d\mathbf{r}'_B \quad (4.2)$$

where L_A and L_B are the two jellium line lengths, and $\hat{\mathbf{u}}_A$, $\hat{\mathbf{u}}_B$, $\mathbf{r}_A$, $\mathbf{r}_B$, are, respec-

tively, their orientations and positions.

Using this function, the distance at which the potential energy equals zero was calculated for the side-side and tee configurations of pairs of identical jellium lines of equal, varying lengths $(L_A = L_B = L_{\mathrm{LJ}})$. It was found that for lines of length $2.5\sigma_0^{\mathrm{LJ}}$ and greater, these were within 1% of the $L_{\mathrm{LJ}} = \infty$ analytical results, these being $(\frac{2}{5})^{1/6}\sigma_0^{\mathrm{LJ}}$ for the side-side interaction $(S(L_{\mathrm{LJ}}))$, and $(\frac{21}{80})^{1/6}\sigma_0^{\mathrm{L-J}}$ for the tee $(T(L_{\mathrm{LJ}}))$. This latter distance was measured between the centre of the cross-bar molecule and the near end of its partner (Fig 4.6).
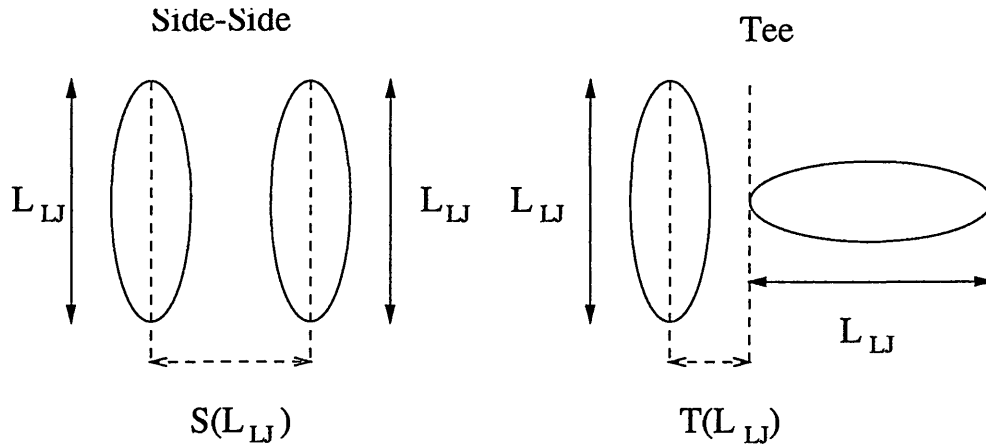

Figure 4.6: Particle positions and separation distances

The above distances were then used to determine the lengths of analogous jellium lines for the two GGB lengths under consideration, by equating the separations at repulsion in the two different configurations for two identical GGB particles with the equivalent separations for two identical jellium lines, $S(L_{\mathrm{LJ}})$ and $T(L_{\mathrm{LJ}})$.

Firstly, considering the side-side interaction, since the distance at zero energy for the side-side interaction of the GGB potential is always equal to $1\sigma_0^{\mathrm{GGB}}$, a quite simple relationship resulted

99

$$1.0\sigma_0^{\text{GGB}} = (\frac{2}{5})^{1/6}\sigma_0^{\text{LJ}}. \tag{4.3}$$

When equating the separation in the tee configurations, which is given by $\sqrt{\frac{\kappa^2+1}{2}}\sigma_0^{\text{GGB}}$ for two identical GGB particles, a term $\frac{L_{\text{LJ}}}{2}\sigma_0^{\text{LJ}}$ needed to be incorporated, since the distance in GGB terms is given between the centres of the two ellipsoids, rather than the centre and the near-end as for $T(L_{\text{LJ}})$. This gave the equation

$$\sqrt{\frac{\kappa^2+1}{2}}\sigma_0^{\text{GGB}} = \frac{L_{\text{LJ}}}{2}\sigma_0^{\text{LJ}} + \left(\frac{21}{80}\right)^{\frac{1}{6}}\sigma_0^{\text{LJ}} \tag{4.4}$$

By combining Eqns 4.3 and 4.4, a relatively simple relationship between a GGB particle of given shape anisotropy κ and the length of its analogous jellium line, L_{LJ} was achieved

$$\frac{L_{\text{LJ}}}{2} = \left[\frac{1}{2}\left(1+\kappa^2\right)\left(\frac{2}{5}\right)^{\frac{1}{3}}\right]^{\frac{1}{2}} - \left(\frac{21}{80}\right)^{\frac{1}{6}}. \tag{4.5}$$

The appropriate jellium lines were then used to plot the well-depths for the four different tee configurations, using Eqn 4.2, and the remaining parameters in the GGB model obtained by fitting the GGB well depths to them, subject to the constraints $\epsilon_0^{ij} = \sqrt{\epsilon_0^{ii}\epsilon_0^{jj}}$ (i.e. the Lorentz-Berthelot mixing rule), $\chi'_{ji} = \chi'_{ij}$ and $\alpha'_{ji} = 1/\alpha'_{ij}$. The parameters obtained are shown in bold in Table (4.3), together with those explicitly declared in the GGB potential.

For the simulations of the I-N coexistence region considered in this work, simple

	ii	jj	ij	ji
	3.5:1	3.0:1	mixed	
χ	0.849	0.800	0.824	0.824
χ'	0.666^r	0.666^r	**0.6662**	**0.6662**
ϵ_0	**1.103**	1.0	**1.050**	**1.050**
α	1.0	1.0	1.0150	0.9852
α'	1.0	1.0	**1.011**	**0.989**

Table 4.3: Parameter set for GGB potential (3.5:1 and 3:1)

perturbations away from the one-component, $\kappa = 2.0$ system, which has been shown to display such a rich phase behaviour earlier in this chapter, were used. This had the advantage that this relatively short molecule was already known to be readily insertable using the Gibbs method, and also that for the pure system a stable nematic phase exists at densities low enough for nematic-vapour coexistence. Thus it was reasonable to expect that for a not too dissimilar mixed system this would also be the case. This was particularly important because it was expected that any simulations close to a smectic phase would fail due to the inability of the Gibbs method to work at the high densities typical of such systems.

Two such deviations from the pure 2:1 system were considered, both being 50:50 mixtures of 2:1's with either 2.5:1s or 3:1s. In arriving at the GGB parameterisation for these mixed systems, an identical method to that described earlier for the longer system was initially considered. However, it needed modifying slightly since the separations at $U_{AB}^{LJ} = 0$ were observed to be approximately the same as the analytical values only for jellium lines of lengths $2.5\sigma_0^{LJ}$ or greater. For the new systems under consideration, it was expected that shorter lengths would be required, so instead of mapping directly onto the fixed separations as previously, the separations at

zero repulsion were obtained by numerical integration of Eqn 4.2 for a number of shorter *identical* lengths in the tee and side-side configurations, giving two functions $T_{\mathrm{LJ}}(L_{\mathrm{LJ}})$ and $S_{\mathrm{LJ}}(L_{\mathrm{LJ}})$ in terms of σ_0^{LJ}. For the GGB particles, again $S_{GB}(\kappa)$ was fixed at $1.0\sigma_0^{\mathrm{GGB}}$, and $T_{GB}(\kappa)$ was as given before, so a relationship could again be constructed between L_{LJ} and κ, now being

$$\frac{T_{\mathrm{LJ}}(L_{\mathrm{LJ}})}{S_{\mathrm{LJ}}(L_{\mathrm{LJ}})} + \frac{L_{\mathrm{LJ}}}{2s_{\mathrm{LJ}}(L_{\mathrm{LJ}})} = \sqrt{\frac{\kappa^2 + 1}{2}} \qquad (4.6)$$

(if one inserts the limiting values of $T_{\mathrm{LJ}}(L_{\mathrm{LJ}})$ and $S_{\mathrm{LJ}}(L_{\mathrm{LJ}})$ for $L_{\mathrm{LJ}} \geq 2.5\sigma_0^{\mathrm{LJ}}$, equation (4.5) is recovered by rearrangement). In practice, a trial and error fitting was sufficient to determine reasonably accurate analogous lengths of the jellium lines for $\kappa = 2.5, 2.0$; since the LHS of Eqn(4.6) was almost linear with L_{LJ} making its behaviour quite easy to predict. Once these lengths had been determined, the fitting was then continued in an identical manner to that described earlier, the four GGB tee well depths being fitted to those from the jellium lines to determine realistic values for the undefined parameters. The final two sets arrived at are given in Tables (4.4,4.5).

	ii	jj	ij	ji
	3.0:1	2.0:1	mixed	
χ	0.800	0.600	0.693	0.693
χ'	0.666^r	0.666^r	**0.6600**	**0.6600**
ϵ_0	**1.520**	1.0	**1.233**	**1.233**
α	1.0	1.0	1.075	0.931
α'	1.0	1.0	**1.050**	**0.952**

Table 4.4: Parameter set for GGB potential (3:1 and 2:1)

	ii	jj	ij	ji
	2.5:1	3.0:1	mixed	
χ	0.724	0.600	0.659	0.659
χ'	0.666^r	0.666^r	**0.6600**	**0.6600**
ϵ_0	**1.316**	1.0	**1.147**	**1.147**
α	1.0	1.0	1.048	0.954
α'	1.0	1.0	**1.030**	**0.971**

Table 4.5: Parameter set for GGB potential (2.5:1 and 2:1)

4.2.2 Simulation Details

The constant pressure Gibbs method was used instead of constant volume used in the previous simulations, since it removes the uncertainty in the coexistence pressures [58]. Also, by setting a relatively low constant pressure, it was hoped that the region at slightly higher densities than the supposed nematic-vapour coexistence could be targeted, which should be the most favourable for conducting the Gibbs simulations. A generic phase diagram showing the expected location of the isobar to be traversed is shown (Fig 4.7).
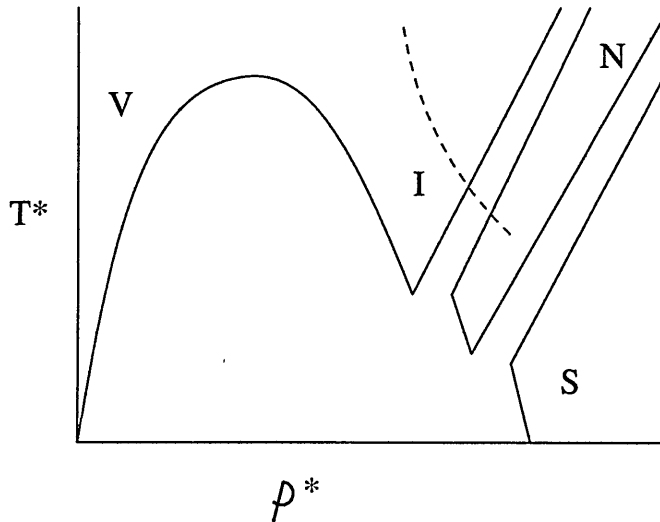
Figure 4.7: Phase diagram and isobar

It should be remembered that in the two-component case being studied here, the system has another degree of freedom, namely concentration, which is not shown here as it is difficult to predict how exactly the three dimensional structure would look. The above diagram is probably best regarded as a slice through this structure at constant concentration.

A number of preliminary simulations were again carried out in an attempt to find a range of suitable temperatures and pressures at which to simulate, and check the suitability of the above parameterisations for simulating I-N coexistence. The isotropic nematic transition for the 2:1 and 3:1 system was found to occur at rather high densities. Also the degree of difference in particle sizes was thought to be a little too large and capable of causing too much fractionation, raising the spectre of layering in the long particle-rich phase.

Instead, attention was concentrated on the 2:1 and 2.5:1 system. Three isobars were studied using single-box NPT-MC, at $P^* = 0.5, 1.0, 2.0$. The potential energy, U^*, density, ρ^*, and nematic order parameter, P_2, were monitored in the box as the temperature was reduced, in order to determine approximate locations for the phase boundaries. These results are shown by a temperature-density plot (Fig 4.8), where the approximate phase boundaries are shown in purple.

As can be seen, the size of the nematic range increases at higher pressures, as has been shown previously [93, 94]. However, although a large nematic range is desirable for this work, too high a pressure would result in the density at which nematic ordering occurs being too large and inhibiting particle insertion to an intractable degree. Some preliminary insertion attempts on configurations produced by the

104

Figure 4.8: Approximate phase diagram for 2.5:1 and 2:1 GGB mixture

above runs suggested that using $P^* = 2.0$ would require prohibitively long runs due to the large number of attempted insertions required. However no such problems were encountered for $P^* = 1.0$, and so this pressure was used for the main Gibbs fractionation simulations.

Before commencing these simulations, some short runs using standard NPT-MC were carried out on the two corresponding pure systems to find the approximate location of the isotropic nematic transition. Although only relatively small numbers of particles were used, $N = 200$, previous finite size studies (see eg. [90]) indicate that the temperature values for the infinite system should be within a few percent. By observation of the nematic order parameter, P_2 and the potential energy per particle, U^*, the transition temperatures were found to be $T_{IN}^* \simeq 0.600$ for the 2:1 system, and $T_{IN}^* \simeq 1.050$ for the 2.5:1 system. Linear extrapolation between these

gave an estimate of the transition temperature for the 50:50 mixed system of around $T^* = 0.825$. Note that this is consistent with the data shown in Fig 4.8.

The main Gibbs simulations were carried out as follows. A totally homogeneous starting system with $N = 500$ and $X_i = 0.50$ was set up and brought off the lattice at a high temperature ($T^* = 4.00$) to remove all traces of order from the system. This was then steadily cooled to a temperature of $T^* = 1.00$ using standard NPT-MC, during which no signs of ordering were observed. The box was then coupled with a replica of itself using the Gibbs code and the particle exchange and volume change moves were switched on, the former being attempted a sufficient number of times to enable at least approximately 0.01% of the particles to be exchanged each step. This did not prove to be too computationally expensive; runs of several hundred thousand MC sweeps were certainly within reach for each temperature studied. Particle exchanges between the boxes were only attempted for the shorter j particles; inter-box identity swap moves [59] were also carried out which proved to be much more efficient as a way of allowing the phase space to sampled effectively. Intra-box identity swap moves were also attempted in the usual MC fashion, although these could only improve the equilibration in each box separately and not for the system as a whole. Reasonable success rates ($\sim 20\%$) were observed for both these swap moves throughout the temperature range studied, and only a few such moves needed to be attempted each sweep.

At the initial high temperatures studied, $1.00 \geq T^* \geq 0.90$, both boxes stayed isotropic, with no evidence of fractionation occuring. However, upon cooling to $T^* = 0.900$, some marked pre-nematic fluctuations were observed in the nematic

order parameter, P_2, of each box, as shown in Fig 4.9. There was, though, no accompanying sign of either of the boxes changing markedly in size, as indicated by the box volumes (given in reduced units of σ_0^3) (Fig 4.10), and it was concluded that the I-N envelope had not yet been reached.

Upon further cooling, orientational ordering was observed over much longer timescales, although at temperatures $T^* = 0.89, 0.88, 0.87$ this did not persist indefinitely, the system showing marked long timescale orientational fluctuations. However, upon cooling the final $T^* = 0.90$ configuration rather rapidly to $T^* = 0.850$, order developed which was observed to be stable over a much more convincing number of MC sweeps. This can be seen by looking at the graphs of the nematic order parameter P_2 (Fig 4.11) and mole fraction of longer rods, X_i (Fig 4.12) in each box. The corresponding volume evolutions (Fig 4.13) show that this system is still equilibrating right up until $\sim 450,000$ sweeps, after which the volume of each box becomes approximately stable. This is confirmed by looking at the potential energy evolution, U^*, for each box during this run (Fig 4.14). In view of the timescale of fluctuations observed here even after the system had evolved to a relatively stable state, production periods of 200,000 MC sweeps were decided upon. These were typically preceeded by equilibration periods of up to 400,000 MC sweeps, although the precise number was decided upon by observation of each particular system evolution.

Further simulations were carried out in a strict cooling sequence from the end of the $T^* = 0.850$ run, a temperature interval of 0.005 being used. Evolutions of the nematic order parameter, P_2 (Fig 4.15), mole fraction of longer rods, X_i (Fig 4.16), number of particles (Fig 4.17) and potential energy per particle, U^* (Fig 4.18), for

107
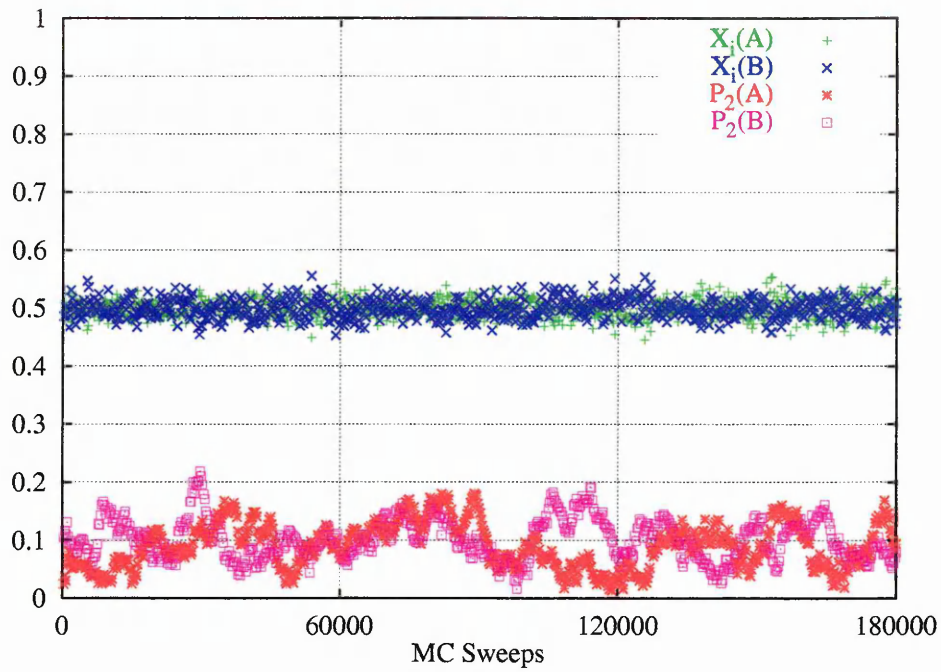
Figure 4.9: Mole fraction and nematic order parameter evolutions for $T^* = 0.900$
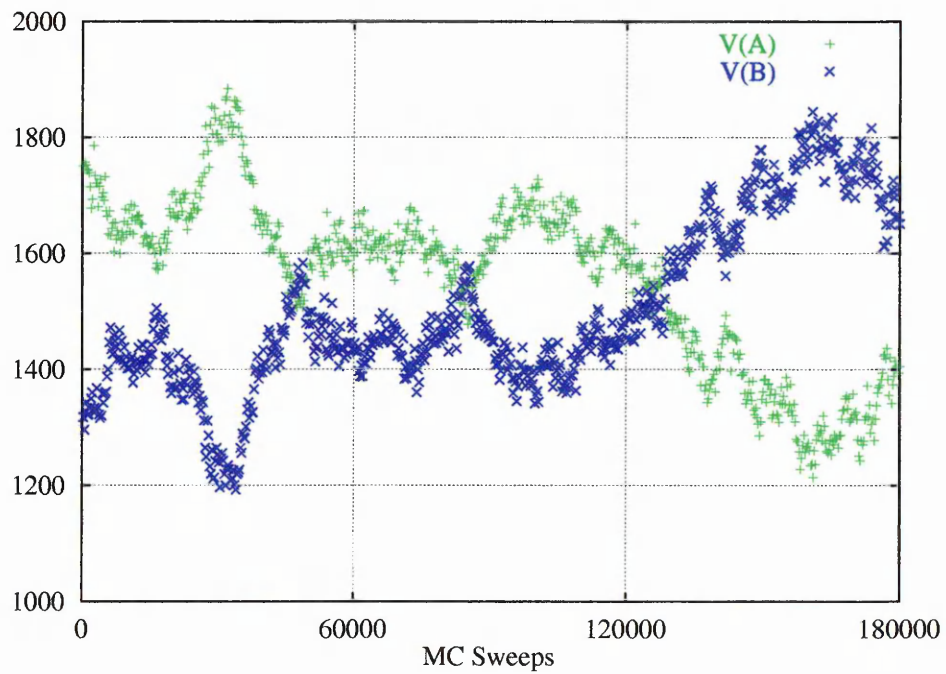
Figure 4.10: Volume evolutions for $T^* = 0.900$

108
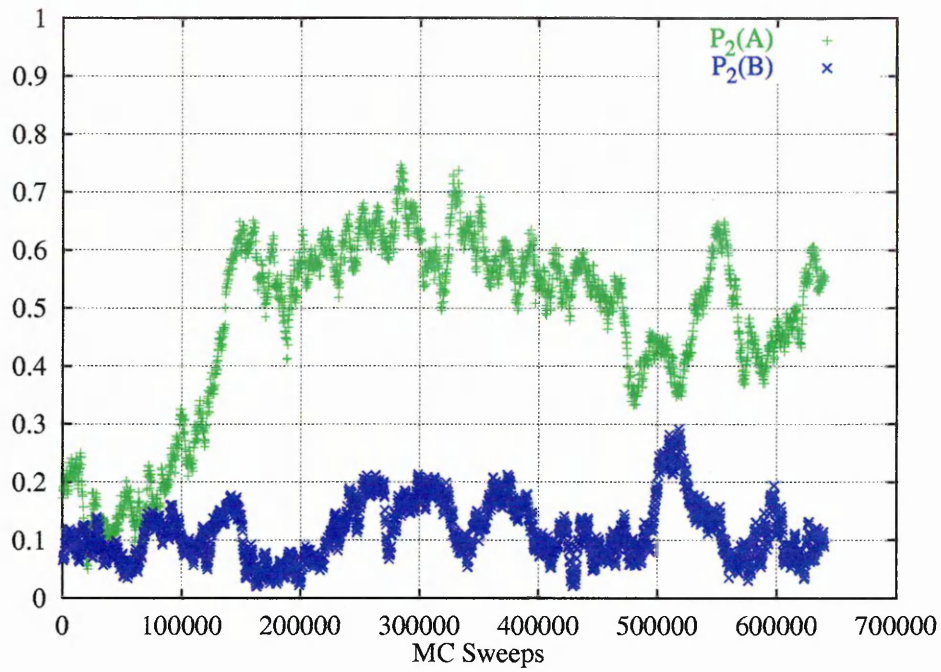
Figure 4.11: Nematic order parameter evolutions for $T^* = 0.850$
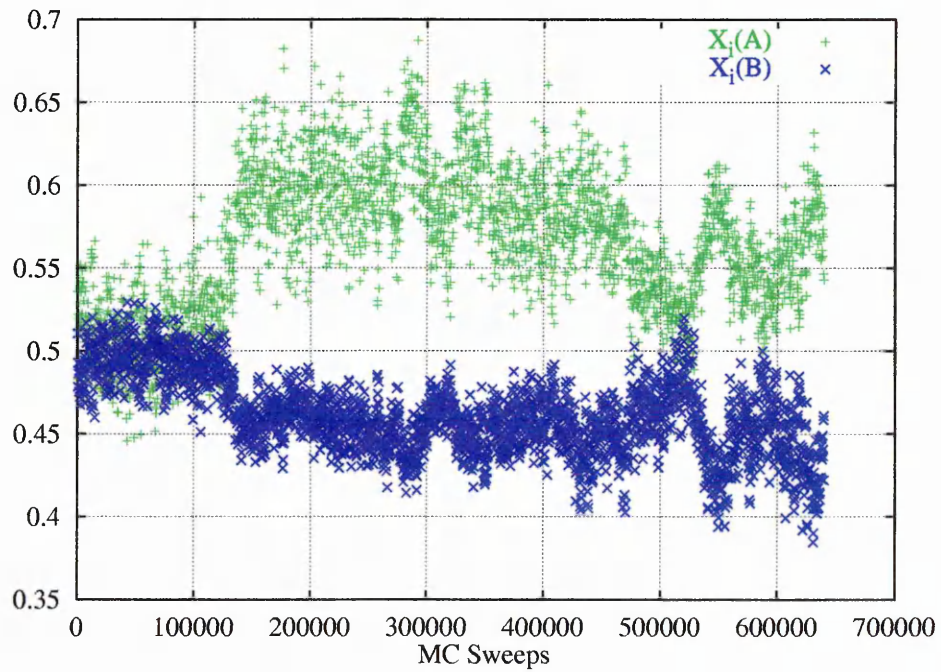
Figure 4.12: Mole fraction evolutions for $T^* = 0.850$

109
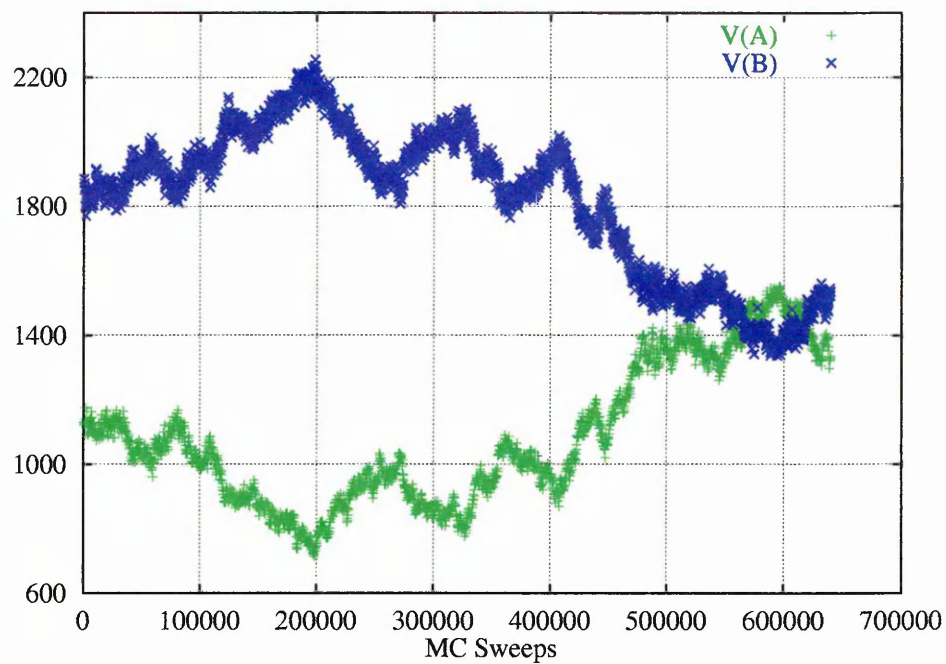
Figure 4.13: Volume evolutions for $T^* = 0.850$
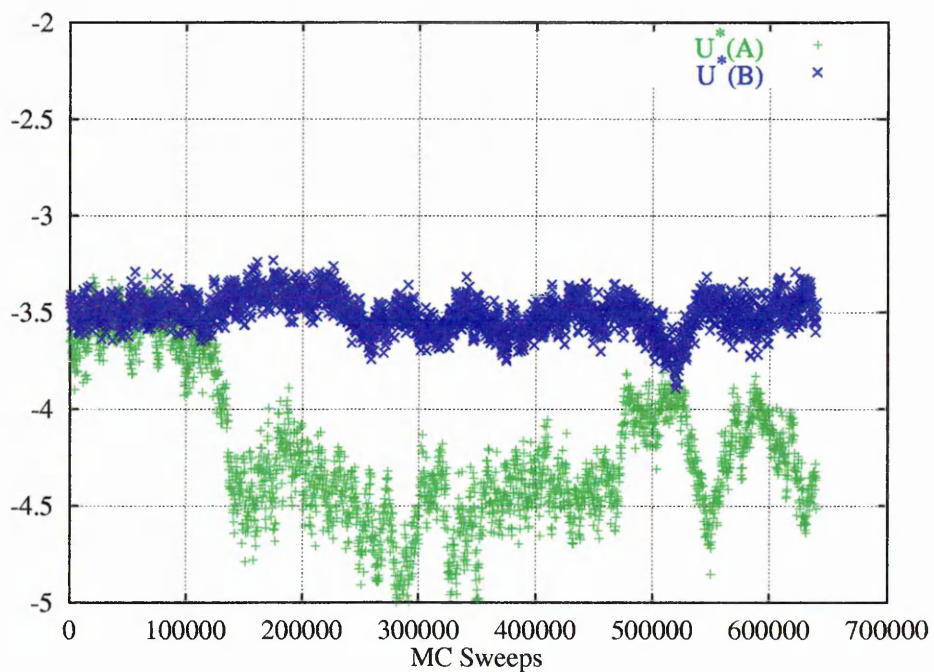
Figure 4.14: Potential energy evolutions for $T^* = 0.850$

each box, are presented for the production runs at $T^* = 0.850, 0.840, 0.830$. All three can be seen to show the characteristic signs of fractionation, namely coexisting isotropic and nematic boxes with a higher proportion of longer rods in the nematic phase. Noticeably larger fluctuations were observed in the nematic order parameter of the isotropic box during the $T^* = 0.830$ run, thought to be indicative of the bottom of the coexistence envelope being approached.

An attempt was also made to warm the system from $T^* = 0.850$, but even after one temperature increase to $T^* = 0.855$, changes in the box identities were observed, and it was concluded that the system was too near a phase boundary (ie the top of the coexistence envelope) to achieve satisfactory equilibration.

Mean values for each of the observables were compiled over each production run, the uncertainties being calculated using a block averaging technique, each production run being split into ten blocks of 20,000 sweeps each. These results, being the potential energy per particle, U^*, the mole fraction of longer rods, X_i, the nematic order parameter, P_2, the box volume, V, in units of σ_0^3, and the number of particles per box, N, are presented below (Table 4.6)

The values for $T^* = 0.855$ are included as a guide to what is happening at the top of the envelope, although they should be treated with some caution as strictly speaking a histogram technique is needed for analysis when the box identities are changing. The data from all the other points show, however, that fractionation is definitely occuring. What is notable is that although the equilibrium value for X_i *in the isotropic phase* clearly decreases with lowering of temperature, as is predicted by mean field theory, no such corresponding trend is observed in X_i for the nematic
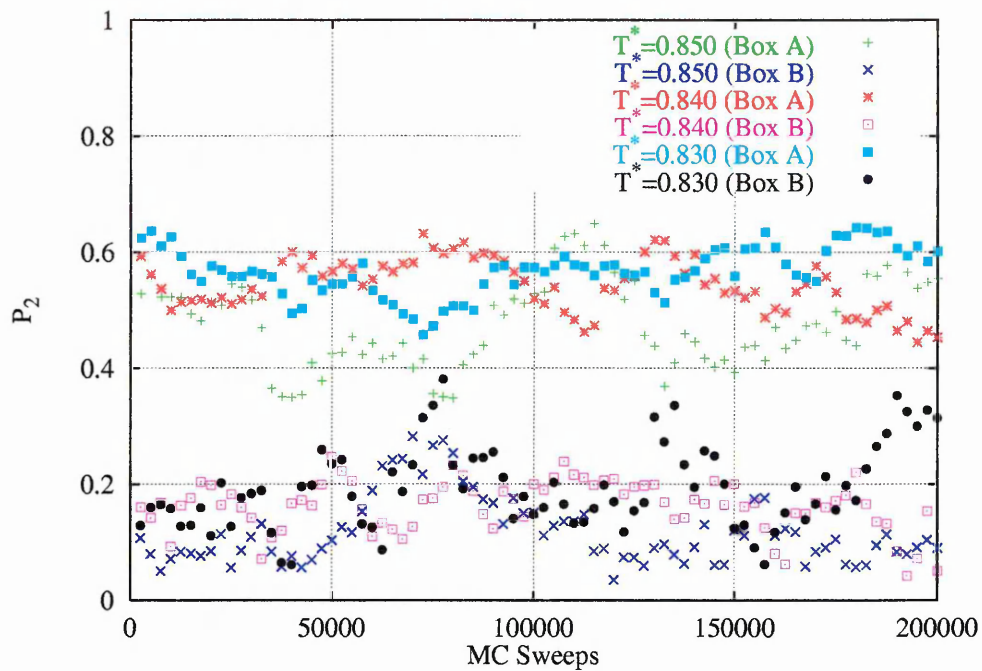
Figure 4.15: Nematic order parameter evolutions for production runs
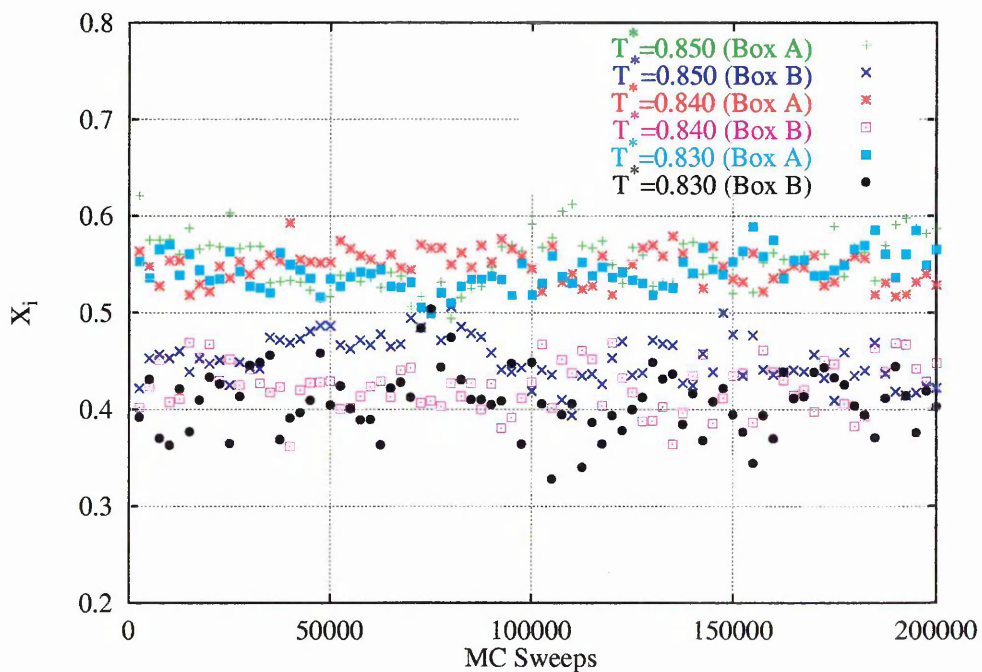
Figure 4.16: Mole fraction evolutions for production runs
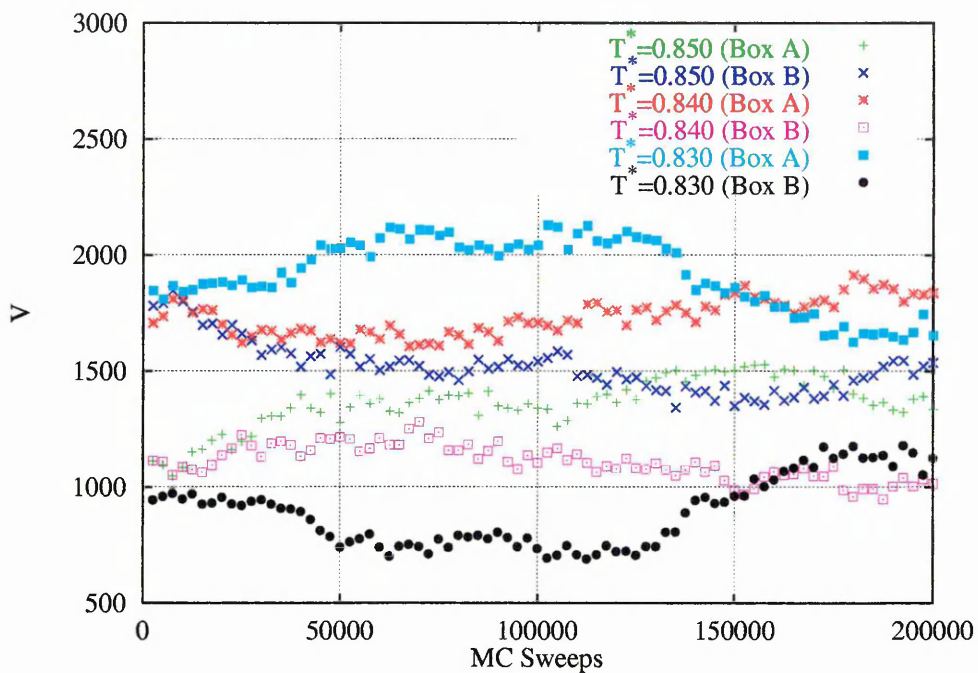
Figure 4.17: Volume evolutions for production runs
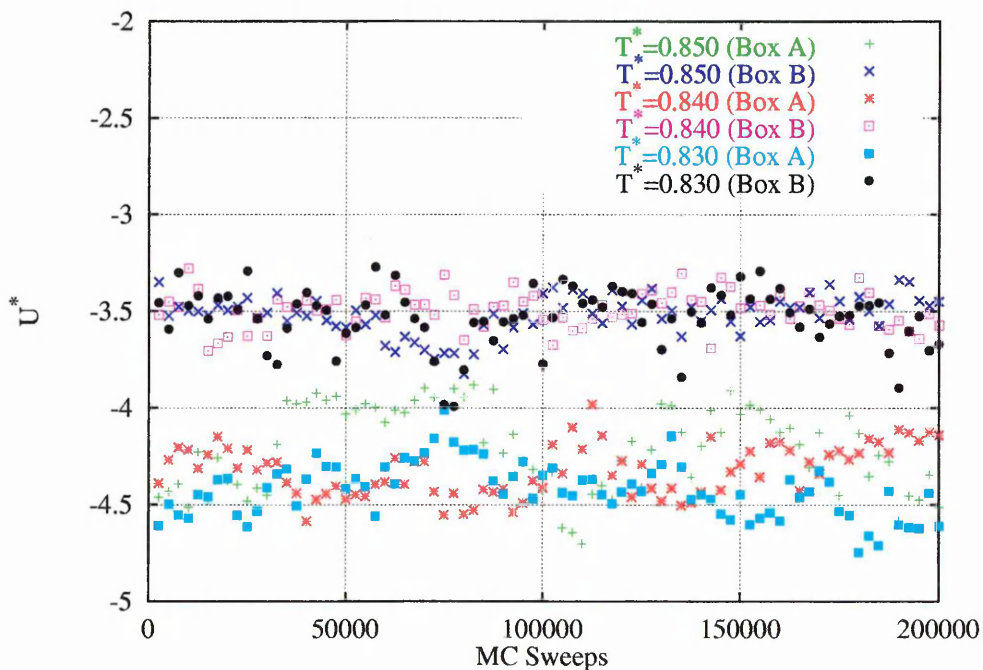
Figure 4.18: Potential energy evolutions for production runs

T^*	0.855	0.850	0.845	0.840	0.835	0.830
$U^*(A)$	-3.82(30)	-4.21(18)	-4.08(11)	-4.33(11)	-4.36(11)	-4.42(11)
$U^*(B)$	-3.70(25)	-3.52(07)	-3.54(06)	-3.50(04)	-3.59(21)	-3.53(10)
$X_i(A)$	0.51(04)	0.55(02)	0.53(01)	0.55(01)	0.54(02)	0.54(01)
$X_i(B)$	0.49(04)	0.45(02)	0.45(01)	0.42(01)	0.43(03)	0.41(02)
$P_2(A)$	0.28(16)	0.48(07)	0.43(05)	0.54(04)	0.55(03)	0.57(04)
$P_2(B)$	0.21(14)	0.12(05)	0.14(04)	0.16(03)	0.21(13)	0.19(06)
$V(A)$	1563(44)	1361(103)	1803(59)	1733(69)	1736(61)	1921(146)
$V(B)$	1334(49)	1519(102)	1066(55)	1106(65)	1092(63)	891(143)
$N(A)$	540(19)	477(36)	632(22)	615(24)	618(24)	688(51)
$N(B)$	460(19)	523(36)	368(22)	385(24)	382(24)	312(51)

Table 4.6: Observable averages at various temperatures

box.

To ensure that the boxes were in chemical equilibrium, the reduced chemical potential of the smaller species being inserted was calculated (Eqn 4.7) along with the difference in chemical potential values calculated in an analogous fashion from the inter-box species swap moves [117], according to

$$\Delta\mu_{ij}^{ex} = \mu_j^{ex} - \mu_j^{ex} = -k_B T \, ln \left\langle \frac{N^i}{N^j + 1} exp \left[-\frac{U_{ij}^*}{k_B T} \right] \right\rangle_{box1}. \qquad (4.7)$$

Here U_{ij}^* is the potential energy change upon converting a particle of species i into one of j, that is, a deflation move, with N^i and N^j the number of particles of species i and j, respectively, in the box where the swap is occuring. Swapping round the i's and j's gives an equation for $\Delta\mu_{ji}^{ex}$, calculated from the energy change associated with an inflation move. These results are presented below (Table 4.7)

Encouragingly, the values for the reduced chemical potential, μ_j^r, of the smaller species j, are approximately equal in both phases for each of the temperatures

T^*	0.855	0.850	0.845	0.840	0.835	0.830
$\mu_j^r(A)$	0.60(4)	0.66(7)	0.65(7)	0.69(7)	0.71(6)	0.77(5)
$\mu_j^r(B)$	0.58(5)	0.61(5)	0.62(5)	0.66(5)	0.65(6)	0.68(5)
$\Delta\mu_{ji}^{ex}(A)$	-0.50(6)	-0.55(5)	-0.58(4)	-0.66(4)	-0.70(3)	-0.75(3)
$\Delta\mu_{ji}^{ex}(B)$	-0.50(6)	-0.55(4)	-0.57(5)	-0.67(3)	-0.69(4)	-0.75(4)
$\Delta\mu_{ij}^{ex}(A)$	1.09(6)	1.14(9)	1.16(5)	1.27(8)	1.29(7)	1.34(7)
$\Delta\mu_{ij}^{ex}(B)$	1.07(9)	1.11(9)	1.14(6)	1.23(6)	1.26(6)	1.31(4)

Table 4.7: Chemical potentials averages at various temperatures

studied. Also, the difference in excess chemical potentials, $\Delta\mu^{ex}$, are basically the same for each of the temperatures studied, with $\Delta\mu_{ji}^{ex}(A) \sim \Delta\mu_{ji}^{ex}(B)$ and $\Delta\mu_{ij}^{ex}(A) \sim \Delta\mu_{ij}^{ex}(B)$. This would seem to indicate that the system is in chemical equilibrium for each of the temperatures studied. However, there is one discrepancy, in that by simple reversal of the species types in Eqn 4.7 the equality

$$\Delta\mu_{ij}^{ex} = -\Delta\mu_{ji}^{ex} \tag{4.8}$$

should be satisfied, which is clearly not the case here. This suggests that at least one of the $\Delta\mu^{r*}$ calculations is not sampling phase space efficiently, leading to an erroneous value. Further analysis of this described in Appendix A, suggests that the identity swap move from i to j ie deflation, which is used in arriving at $\Delta\mu_{ij}^{ex}$, gives erroneous results.

Attempts were made to cool the system further to $T^* = 0.820$, but problems were encountered with the isotropic box becoming so small that the potential cutoff exceeded half the box length, and it was again concluded that the system was too near to a phase boundary (this time the bottom of the envelope) for fractionation to be

observed. Instead a more rapid cooling was attempted, with the temperature being lowered first to $T^* = 0.80$, and then to 0.78. At the higher temperature a definite increase in the degree of order in the isotropic box was observed, but there was still markedly less than in the nematic box, and the mole fractions still showed evidence of phase separation. Only at the lower temperature did this difference in the degree of nematic order in both of the boxes become negligible, although fluctuations in the mole fraction values were still observed. It was concluded however that this behaviour was representative of the one-phase nematic region. Evolutions of the nematic order parameter and mole fraction per box at these two temperatures are shown (Figs 4.19,4.20).

This single phase point along with the one observed at $T^* = 0.900$ were plotted with the coexisting mole fraction values to construct a rudimentary phase diagram (Fig 4.21).

The linear extrapolation on (Fig 4.21) is simply a straight line between the two isotropic nematic transition temperatures for the pure systems, which were determined as described earlier. Compared to the generic phase diagram in Chapter 2, and reproduced in Fig 4.22, which is predicted by mean field theory [38], the stable values for the mole fraction of longer rods, X_i, in the coexisting nematic phase do not show the expected decreasing trend with lowering of temperature. In seeking to explain this discrepancy, we point out that whilst Fig 4.22 relates to two infinite bulk phases in coexistence with each other, the system studied here is subject to finite size effects due to the periodic boundary conditions imposed. The periodicity of the simulation causes the nematic phase to be stabilised which means that it is

116
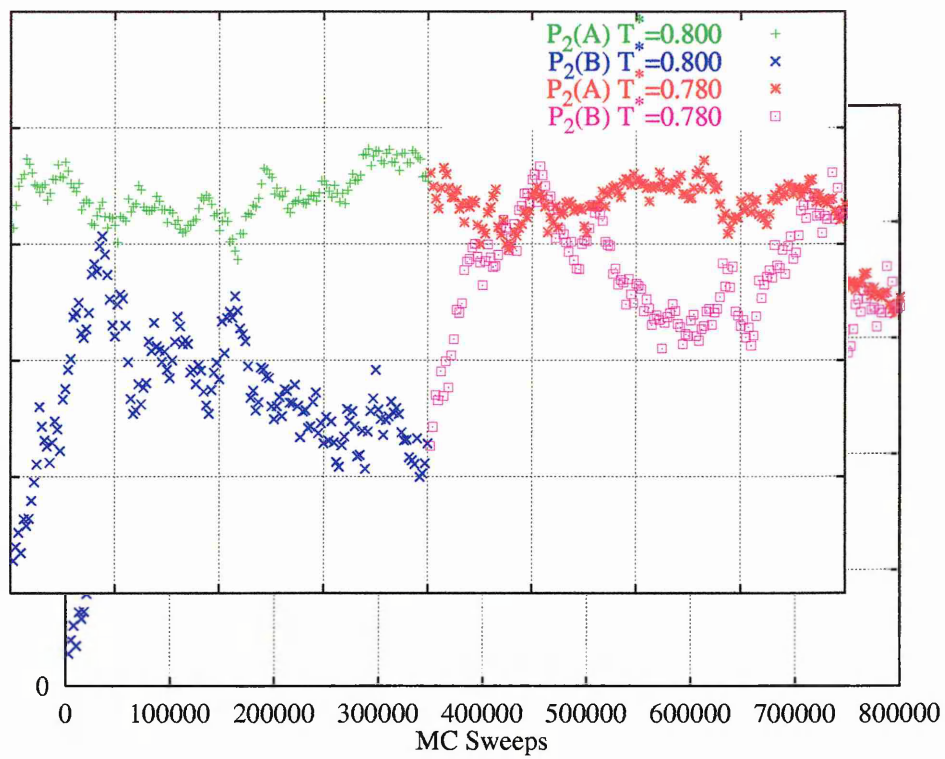
Figure 4.19: Nematic order parameter evolutions for $T^* = 0.80, 0.78$
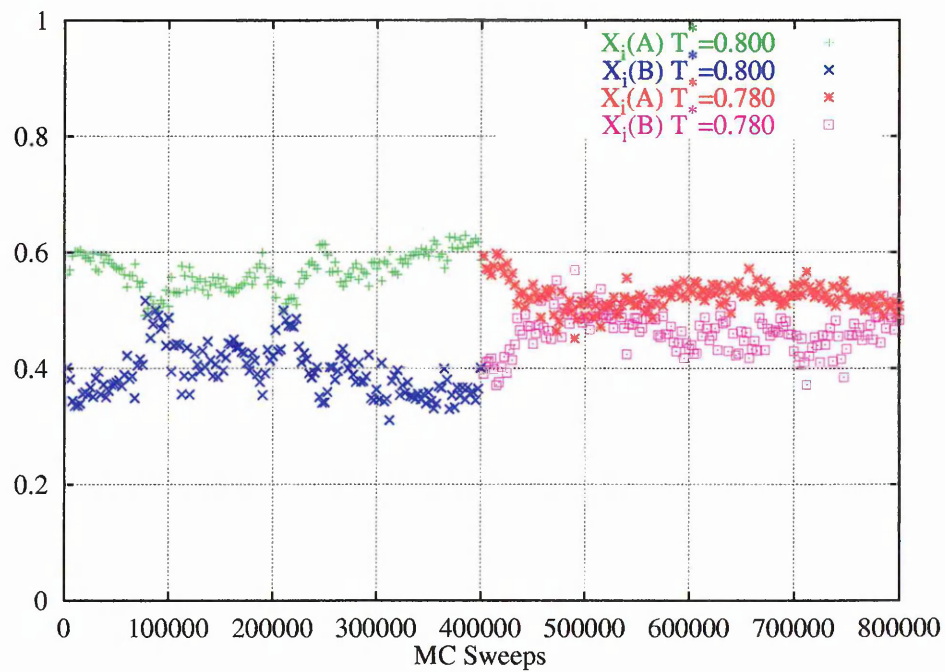
Figure 4.20: Mole fraction evolutions for $T^* = 0.80, 0.78$

117
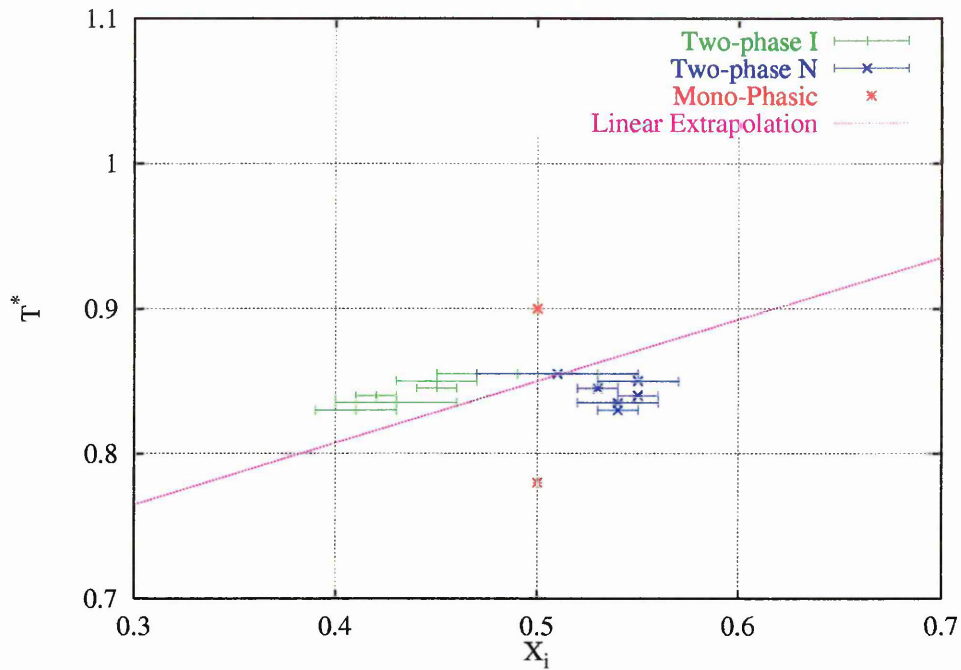
Figure 4.21: Phase Diagram

stable at a lower mole fraction than would be the case in the infinite system. This effect is most noticeable at the top of the envelope, where, due to the Lever rule, the size of the box containing the nematic phase is at its smallest. The periodicity induced enhancement of the nematic phase is, therefore at its largest and the shift of this branch to lower concentrations is maximal at the top of the envelope. In the isotropic phase, a similar effect can be expected at the bottom of the coexistence envelope. The finite size of the isotropic box also promotes orientational order, and hence requires a lower concentration of long rods than an infinite system in order to stop a nematic forming. As the temperature is lowered the decrease in the size of the isotropic box leads to progressively enhanced periodicity, and thus, a growing divergence from infinite system behaviour. Applying these arguments leads to the modified phase diagram shown schematically (Fig 4.23). Whilst a full study of the system size dependence of the I-N coexistence envelope is beyond the scope of this

118
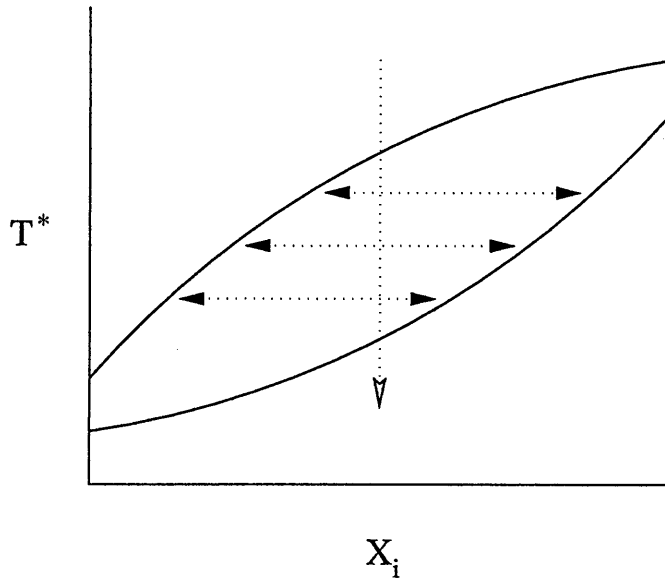
Figure 4.22: Generic Phase Diagram - Infinite System
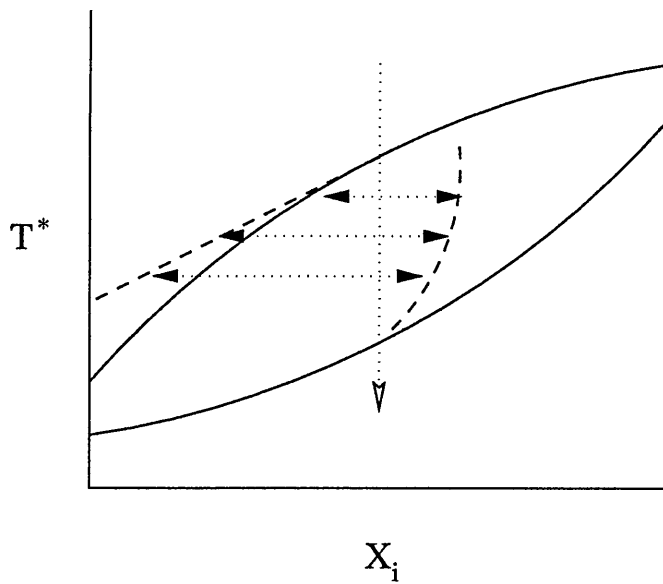
Figure 4.23: Generic Phase Diagram - Finite System

119

thesis, we note that the trends shown by our results are certainly consistent with these finite size arguments.

4.3 Conclusions

This section considered two types of simulation, based, respectively, on one and two-component Gay-Berne (GB) systems. The GB potential has been extensively studied and provides a rich body of previous work for comparison. For the two-component system, the interaction between unlike particles was modelled using a recently developed generalisation of the Gay-Berne (GGB), which has been simulated [99] and shown to display behaviour in qualitative agreement with that observed experimentally for liquid crystal mixtures.

Firstly, the one component coexistence will be considered. This set of results compares well with previous studies of isotropic-vapour coexistence for the Gay-Berne model using different parameters, showing similar coexisting densities. The additional discovery of nematic-vapour coexistence was an initially unexpected result, but in retrospect is consistent with previous results when the relative strengths of the various well-depths are taken into account. Unfortunately, equilibration problems were encountered as the temperature was lowered past a certain point in the nematic phase, due to the insertion move of the Gibbs ensemble becoming rapidly intractable. This meant that stable nematic-vapour coexistence could only be confirmed in a small temperature range. However, this is still an important result, since it shows this GB parameterisation to have a relatively stable nematic phase, and

opens up the possibility of direct nematic-vapour coexistence simulation, which was exploited later in this work.

The results of this work were then used as the basis for the study of two-component coexistence at the isotropic-nematic transition. Theoretical predictions [8] have suggested that a widened coexistence envelope should exist at this transition for two-component systems, and as would be intuitively expected, that the more anisotropic particles should occur with a higher concentration in the ordered phase.

Before simulating such a system though, a parameterisation for a suitable two-component interaction needed to be arrived at. This was based upon a fitting conducted in a previous study [99] of the GGB, where Lennard-Jones jellium lines were used to provide the relative strengths of the particle interactions in various configurations.

Preliminary simulations were carried out to estimate the region of phase space of interest, using a standard one-box technique, and then the main Gibbs simulations were initiated. These were relatively expensive computationally, and required considerable run times to achieve equilibration. However, in the middle of the temperature range where signs of phase separation were observed, stable coexistence was indicated by the evolution of the system order parameters, mole fractions and, most importantly, the average chemical potential values for each phase. It was therefore concluded that satisfactory evidence for isotropic-nematic phase separation in this mixture had been gathered. Furthermore, the Gibbs technique was found to be applicable to coexistence between a judicious choice of moderately dense fluids, without recourse to technical refinements, such as an insertion biasing. Here the

relatively small degree of shape anisotropy enabled particle insertion to be successful at high enough densities for an ordered phase to be observed, though the rate of insertion was still low enough to cause considerable computational cost.

Upon analysis of the results, a notable shift in the coexistence curves from the form predicted by mean field theory was observed, and it is suggested that this is due to a finite size effect. This will be very significant when studying the I-N transition with the Gibbs ensemble, since the Lever rule dictates that relatively small boxes should form at phase points close to the coexistence boundaries. Previous studies have shown a small but measurable temperature shift of the order of a few percent at the isotropic-nematic transition, on changing the system size by around a factor of two ($N = 512$ to $N = 1000$) [92]. An intuitive discussion of how this finite size effect would affect the phase envelope has been given, which is consistent with the shift observed here. However, a detailed quantitative analysis beyond the scope of this thesis would be required to be verify the argument.

In conclusion, a simulation of fractionation at the isotropic-nematic transition, albeit subject to finite size effects, has been achieved, and from a scientific point of view the application of the Gibbs ensemble to such a dense system is a notable step forward. These results should also prove to be of use in further simulations using the generalised Gay-Berne potential, giving an estimate of the degree of fractionation expected in such a mixture. However, much remains to be done to achieve a fuller understanding of the driving effects in bulk mixtures of liquid crystals, before the question of interfacial effects is considered.

Chapter 5

Thin Film Simulations

5.1 Introduction

In this chapter, the results of computer simulations carried out on thin films of
Gay-Berne particles, in coexistence with their own saturated vapour, are reported,
together with appropriate analysis and comparison with existing results in the literature.

The motivation for this work was provided by the discovery of a region of nematic-
vapour coexistence for a specific parameterisation of the GB model, as detailed in
Chapter 4. The lack of interfaces in the Gibbs simulations meant that no preferred
alignment could be induced; instead the nematic director adopted an arbitrary direction in the ordered phase.

It is, however, possible to induce a preferred direction by introducing a degree of
inhomogeneity into the system, such as with an external field [84], presence of sur-

faces [105] or, possibly, the use of an extremely anisotropic simulation box, where periodic boundary conditions over different repeat lengths could feasibly result in enhanced ordering along some direction. The inhomogeneity in this last case would arise due to the non-uniform suppression of the system-disordering fluctuations which are limited by the artificial periodicity in such simulations. In the following sets of simulations, two such aspects are present: a liquid vapour surface and an elongated simulation box with a relatively small cross-sectional area. Primarily, this work is concerned with the interfacial influence on both alignment and the ordering regime - it is well established [21, 44, 45] that in systems involving non-spherical molecules, the molecules close to the surface will generally have a preferred lowest free energy configuration strongly dependent upon their orientation relative to the surface. If the rest of the bulk material is nematic with an arbitrary preferred direction, the system should minimise its energy by forming a nematic monodomain with the director dictated by the surface molecules. However, this will not necessarily be the case, as will be seen later in this chapter.

Preliminary investigations, conducted with a homogeneous starting system at a region in the phase diagram known (from the Gibbs results) to display isotropic-vapour coexistence proved to be unsatisfactory. Although spontaneous phase separation was observed after reasonable equilibration times (the order of 100000 MC sweeps for 500 particles), it was in the form of 2 vapour regions. Both of these were approximately spherical in shape and showed no sign of coalescing even after considerable run times, and so it was decided to use a more judicious initial configuration. This consisted of a central isotropic liquid region which was equilibrated separately at a temperature and density corresponding approximately to that of an isotropic liquid

124

phase observed in the Gibbs simulations ($T^* = 0.550$ and $\rho = 0.35$). The equilibrated region was then placed in a long thin simulation box and surrounded on both sides (in the z direction) by equilibrated vapour, again at a phase point determined by the Gibbs results. A schematic representation of the system is shown in Fig 5.1.
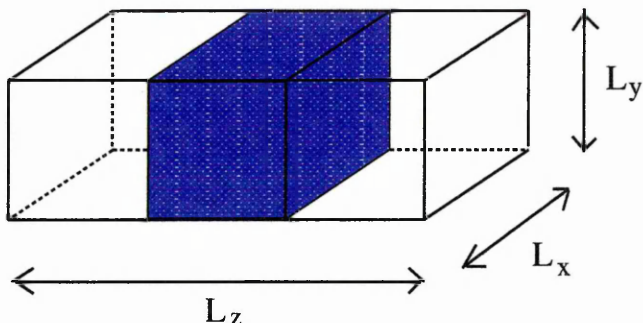

Figure 5.1: Schematic representation of the simulation box

The usual periodic boundary conditions were employed in all three directions. Strictly speaking, this periodicity in the z direction means that the system consists of a series of films, or what might be called a stripe system. The presence of these extra films could be argued to affect the behaviour observed. However, the low density vapour between the films is always in the isotropic state, and thus will not be able to support orientational fluctuations across its width.

As is usual for computer simulations [5], the starting configuration was equilibrated for a sufficient length of time for all of the observables to adopt stable values. The average values were then calculated over production runs of length such that the averages and their errors were stable. The final configuration from one production run was then used as the starting one at the next, lower, temperature simulated.

Three such systems were studied, with varying numbers of particles and simulation

box length to breadth ratios, but all with approximately the same overall density ($\rho^* \approx 0.17$) known to be in the coexistence region, and approximately the same cross-sectional area.

- A N=500; Box 3:1:1; MC simulation

- B N=1626; Box 6:1:1; MD simulation

- C N=7104; Box 22:1:1; Parallel MD Simulation

The results and subsequent analysis of each of these are reported in the following three sections.

5.2 Small System

The first film simulations were carried out using the Monte Carlo technique, which had been shown to work efficiently in this region of phase space when used for the Gibbs ensemble simulations. Also the code was readily convertible into an anisotropic (cuboid) box version (system dimensions used being $34.2\sigma_0 : 11.4\sigma_0 : 11.4\sigma_0$). The starting temperature was chosen from the bulk phase diagram described in Chapter 4. The system was slowly cooled until ordering was indicated by a few key observables.

The nematic order parameter $\bar{P}_2$ and the potential energy per particle $\bar{U}^*$(both defined in Chapter 3) were measured for the system as a whole, i.e. over all particles. Although both vapour and liquid regions contribute to these values, the fact that

the majority of the particles reside in the liquid film (approx. 480 c.f. 20 in the vapour) means that they are a reasonable guide to the progress of ordering within the film. The integrity of the film was also measured by dividing the system into strips in the z direction and calculating the density for each of these strips.

The values $\bar{P}_2$ and $\bar{U}^*$, along with the equilibration period run lengths (R.L.) required for the system to stabilise at each temperature, are given below (Table 5.1). These averages were calculated over production runs of 100,000 MC sweeps, divided into 10 blocks of 10,000 sweeps each to calculate uncertainties. This information is also shown in graphical form (Figs 5.2 and 5.3).

T^*	$\bar{U}^*$	$\bar{P}_2$	R.L.
0.500	-2.13(4)	0.07(1)	50
0.490	-2.25(4)	0.08(1)	50
0.480	-2.37(5)	0.09(2)	50
0.470	-2.47(8)	0.15(6)	100
0.460	-2.78(9)	0.29(5)	200
0.450	-3.21(9)	0.56(4)	100
0.440	-3.46(6)	0.64(2)	50
0.430	-3.59(6)	0.66(2)	50
0.420	-4.96(1)	0.89(1)	50
0.410	-5.00(1)	0.90(1)	50
0.400	-5.04(1)	0.91(1)	50

Table 5.1: Observable averages at various temperatures

As can be seen by inspection of the values and graphs, two discontinuities in the potential energy occur in the temperature range covered, at $T^* \approx 0.465$ and $T^* \approx 0.425$. The one at the lower temperature is quite marked, whereas that at $T^* \approx 0.465$ is much weaker. However, 3 distinct regions where the potential energy is linear with temperature are clearly visible. Observation of the nematic order parameter for these three regions suggests them to correspond to isotropic, nematic and smec-
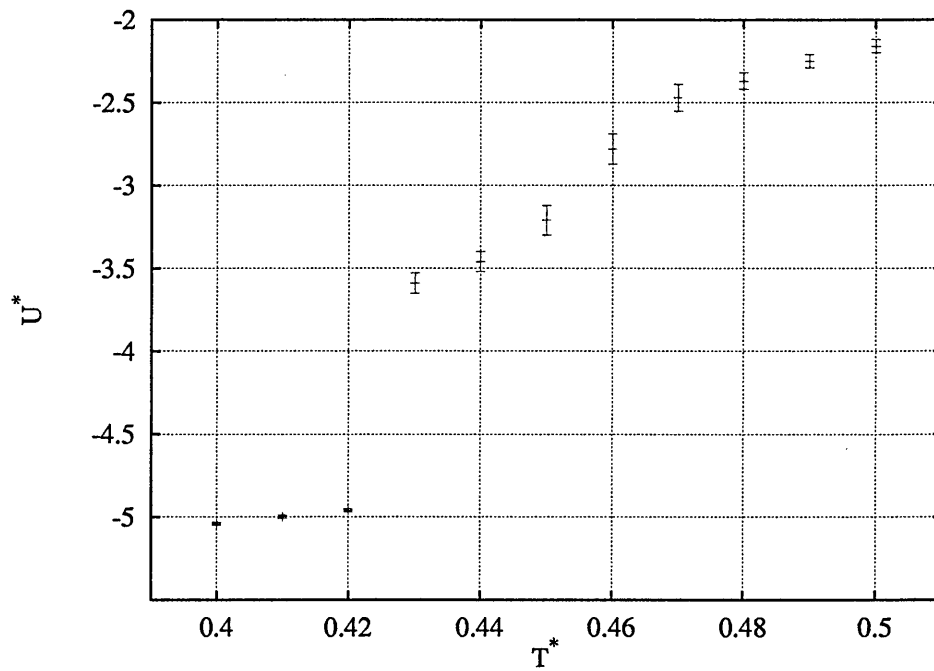
Figure 5.2: Average potential energy vs temperature for the 500 particle system
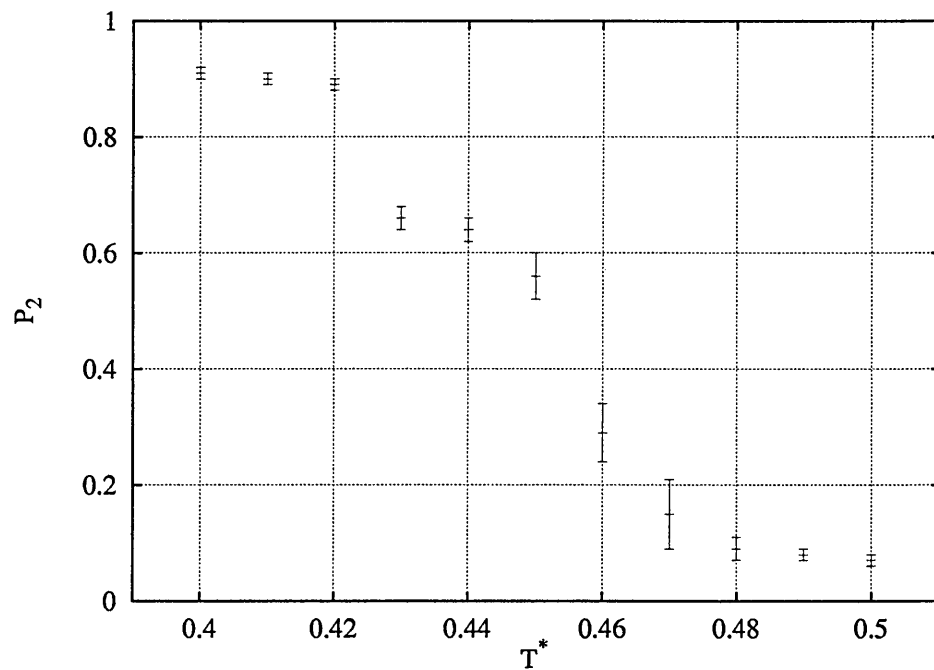
Figure 5.3: Average nematic order parameter vs temperature for the 500 particle system

tic/crystalline phases, in order of decreasing temperature. This agrees with the size of the discontinuities since the isotropic-nematic transition is generally much weaker than the nematic-smectic.

This was confirmed by observation of configuration snapshots for each of these phases, showing definite nematic ordering for the intermediate phase (Fig 5.4) with homeotropic (perpendicular) anchoring at the free surfaces. A comparison of the density profiles obtained at three temperatures (Fig 5.5), corresponding to the three different phases as labelled, also shows a marked difference between the values, indicative of phase changes. The additional profile, at $T^* = 0.460$, corresponds to the I-N transition region. It is interesting to note that at this temperature a higher density is observed at the centre of the film than near to the interfaces, indicating orientational ordering occurs in the middle of the film first. It also suggests that rather than seeing a sudden discontinuity in the density values at the transition, as for the potential energy and nematic order parameter, the high density region of the film instead grows slowly from the centre. At this particular temperature, a long
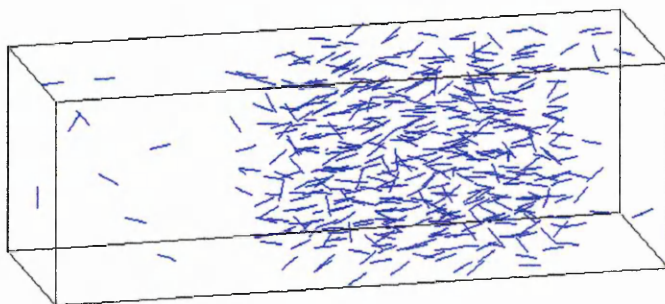

Figure 5.4: Configuration snapshot for $T^* = 0.440$

equilibration period was needed due to long timescale fluctuations observed in the order parameter. Initially, insufficient equilibration of the system was suspected,
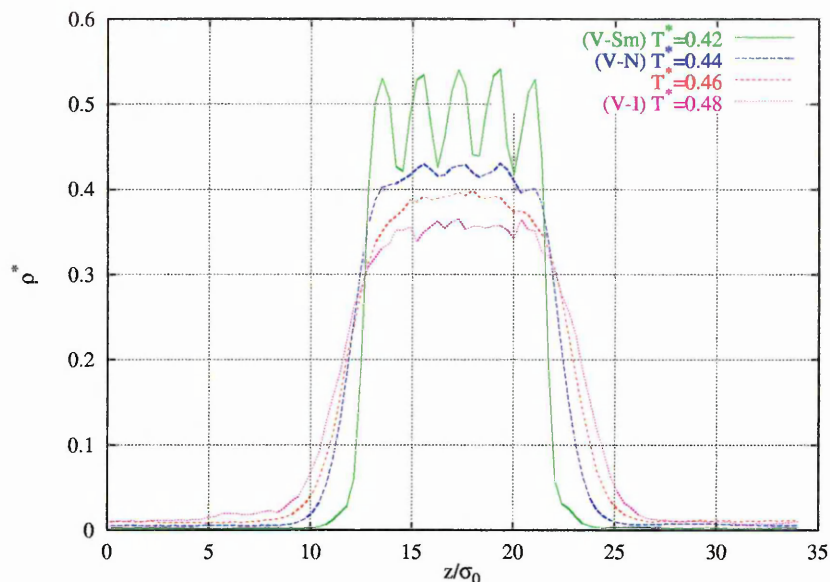
Figure 5.5: Density profiles for various temperatures

but the persistence of these oscillations, even after run times of several 100000's of sweeps, indicated that some sort of orientational fluctuations were taking place within the film. It was decided to defer in-depth analysis to a wider film, where the orientational fluctuations would have a larger length scale over which to occur, thus making them easier to quantify and analyse. These fluctuations were observed to be much smaller upon cooling below $T^* = 0.450$.

5.2.1 Summary

This first attempt at reproducing the phase coexistence shown in the Gibbs ensemble work has confirmed the validity of those results, in that stable coexistence was indeed observed, as well as the expected transition between the isotropic and nematic phases of the liquid film. Rather pleasingly, at low enough temperatures in the nematic range, homeotropic anchoring was observed at the free interfaces, with this

alignment being conferred across the whole of the film in the form of a nematic monodomain. However, at the onset of nematic ordering, orientational fluctuations were observed, suggesting a non-trivial ordering mechanism. In depth analysis of these fluctuations within the film and the effects of the interfaces upon them was considered inappropriate for this very thin film, and deferred to the next section.

5.3   Medium System

The main series of unconfined simulations were carried out using 1626 GB particles, in a 6:1:1 ($68.1\sigma_0$: $11.4\sigma_0$: $11.4\sigma_0$) box. This resulted in a film which was approximately $20\sigma_0$ wide, or 10 molecular lengths. Initial simulations of this system using one box MC proved to be inefficient, due to the slow reorientation of ordered domains, and the molecular dynamics (MD) technique at constant NVT was decided upon instead. The temperature was kept constant by rescaling the velocities at each timestep, which was fixed to $\delta t = 0.0015 \, (m\sigma_0^2/\epsilon_0)^{\frac{1}{2}}$.

In addition to the overall observables and the density profiles calculated as for the smaller system, a qualitative measurement of the interfacial alignment was determined. Since the interfaces had been set up perpendicular to the z-axis, and were observed to stay roughly in that plane throughout the above simulation, an indication of the interfacial alignment could be obtained by measuring the orientation of of all molecules with respect to the z-axis. This was comparatively easy to calculate since the orientations of the molecules are stored in terms of the three director cosines. The z-axis order parameter Q_{zz} is given by

$$Q_{zz} = \frac{1}{N} \sum_{i=1}^{N} \left[\frac{3}{2} u_{i,z}^2 - \frac{1}{2} \right] \tag{5.1}$$

This takes similar values to P_2, but is restricted by P_2 (i.e. it can never be greater in magnitude) so the ratio Q_{zz}/P_2 is useful in determining the direction of alignment for systems displaying intermediate orientational order.

Values for the average densities of the two coexisting phases and the interfacial thickness were obtained by fitting the measured density profiles $\rho(z)$ to hyperbolic tangents of the form

$$\rho(z) = \frac{1}{2} \left(\rho_l + \rho_v \right) + \frac{1}{2} \left(\rho_l - \rho_v \right) tanh \left[\left(z - z_G \right) / 2\delta \right] \tag{5.2}$$

where the adjustable parameters are ρ_l and ρ_v, the densities of the bulk liquid and vapour phases; z_G the position of the Gibbs dividing surface; and δ, the interfacial thickness.

As well as calculating the order parameters P_2 and Q_{zz} for the system as a whole, they were profiled across the system in an analogous fashion to the density profiles shown in the previous section, so that the progress of orientational ordering within the film could be monitored. The $P_2(z)$ values were renormalised using a modified eigenvalue calculation due to Wall and Cleaver [112,118], in order to reduce the tendency for small numbers of molecules in the vapour phase to give misleadingly high values.

Two other quantities were also profiled; the *normal* and *transverse* components of the

pressure tensor, which were used to calculate the surface tension for the interfaces. These are defined by

$$p_N(z) = \rho(z)T^* - \frac{1}{2V_c}\left\langle \sum_{i,j}^{(k)} z_{ij}\frac{\partial U_{ij}}{\partial z_{ij}}\right\rangle \qquad (5.3)$$

$$p_T(z) = \rho(z)T^* - \frac{1}{4V_c}\left\langle \sum_{i,j}^{(k)} x_{ij}\frac{\partial U_{ij}}{\partial x_{ij}} + y_{ij}\frac{\partial U_{ij}}{\partial y_{ij}}\right\rangle \qquad (5.4)$$

where V_c is the volume of each bin and the symbol (k) means that the summation is restricted to pairs of molecules of which at least one is in the corresponding bin. The surface tension γ^* can be calculated from these by numerical integration [44, 119] according to the expression

$$\gamma^* = \int_{z_v}^{z_l} [p_N(z) - p_T(z)]\, dz \qquad (5.5)$$

where the limits of integration refer to values in the bulk liquid and vapour phases far from the interface. In practice the integration was performed over both interfaces present in the system, and a value obtained by averaging these two.

Details of the behaviour of these various properties upon cooling are now presented.

133

5.3.1 Orientational Order

As the system was cooled down, the average density of the liquid and vapour parts of the system and the interfacial thickness were measured, along with the overall order parameters discussed in the previous section, and the system potential energy per particle. These are displayed along with the length of each equilibration run in thousands of timesteps (R.L.) (Table 5.6). Also shown are the potential energies and order parameters in graphical form (Figs 5.7 and 5.8). The errors were estimated using a block averaging technique, each block consisting of 10,000 MD steps and there being at least 20 blocks in each production run.

T^*	$\bar{U}^*$	ρ_v	ρ_l	δ	PII	$\bar{Q}_{zz}$	$\frac{Q_{zz}}{P_2}$	R.L.
0.520	-2.262(43)	0.035	0.309	1.16	0.041(14)	0.005(24)	0.122	200
0.500	-2.457(42)	0.024	0.329	0.94	0.047(18)	0.004(27)	0.085	200
0.490	-2.558(36)	0.020	0.337	0.82	0.056(22)	0.004(29)	0.071	200
0.485	-2.630(34)	0.018	0.343	0.81	0.053(19)	0.002(28)	0.038	200
0.480	-2.701(38)	0.013	0.346	0.84	0.060(23)	0.003(29)	0.050	200
0.475	-2.750(59)	0.016	0.353	0.83	0.126(58)	-0.022(47)	-0.175	350
0.473	-2.966(06)	0.015	0.369	0.83	0.286(53)	-0.130(37)	-0.455	350
0.470	-3.243(06)	0.013	0.382	0.81	0.461(38)	-0.016(75)	-0.035	1200
0.465	-3.412(52)	0.012	0.397	0.80	0.549(28)	0.333(84)	0.607	500
0.460	-3.604(46)	0.011	0.406	0.73	0.626(23)	0.577(32)	0.922	400
0.455	-3.687(57)	0.009	0.408	0.67	0.643(27)	0.597(52)	0.928	300
0.450	-3.786(42)	0.008	0.412	0.65	0.676(18)	0.634(39)	0.938	200
0.445	-3.887(45)	0.008	0.418	0.63	0.695(20)	0.591(68)	0.850	200
0.440	-5.212(31)	0.007	0.475	0.40	0.889(04)	0.819(08)	0.921	350

Figure 5.6: Average observables at various temperatures

At high temperatures, the film remains in the isotropic phase, as can be seen from the values for the orientational order parameters. Inspection of the profile and snapshot (Figs 5.9 and 5.10) confirms that there is no local nematic order.

Upon lowering the system temperature, there is a large discontinuity in the potential
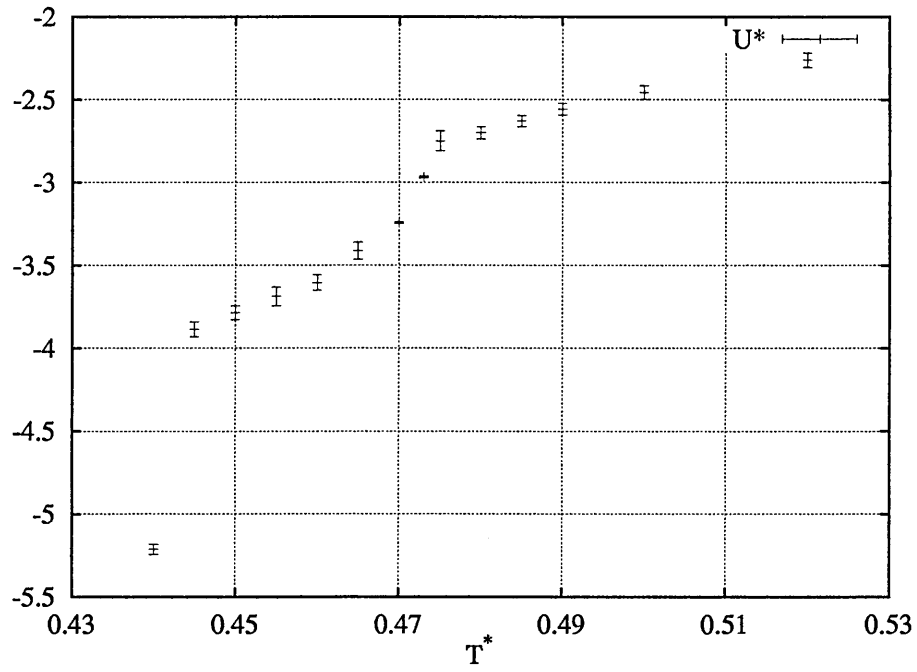
Figure 5.7: Average potential energy vs temperature for the 1626 particle system
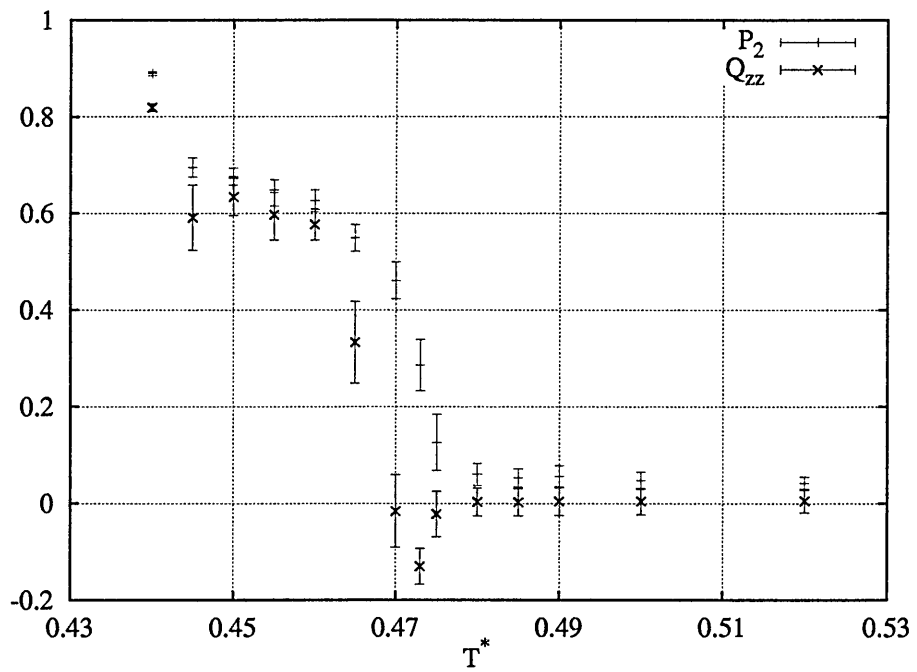
Figure 5.8: Average order parameters vs temperature for the 1626 particle system

135
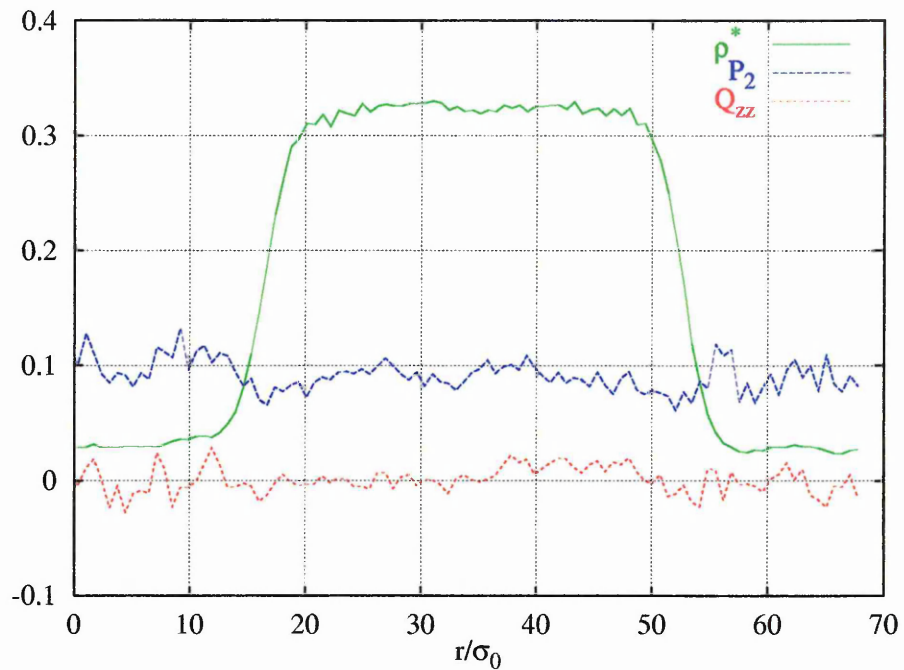
Figure 5.9: Order parameter profile at $T^* = 0.520$
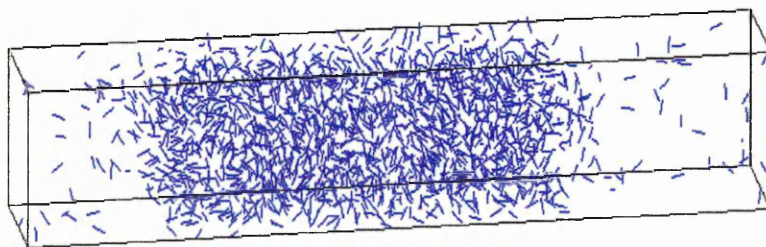
Figure 5.10: Configuration snapshot at $T^* = 0.520$

136

energy values around the temperature $T^* = 0.470$, which suggests that a phase transition has occured. This is consistent with the corresponding values for the overall nematic order parameter, $\bar{P}_2$, which increases to a value typical of a nematic phase. Progressing further into the nematic range, the values for the z-axis order parameter, $\bar{Q}_{zz}$ seem to contradict what would be expected considering that the final stable nematic has a positive $\bar{Q}_{zz}$ value. This can be explained by looking at the equilibrium profiles for $T^* = 0.475$ and $T^* = 0.473$ (Figs 5.11 and 5.12). It is clear that the film has ordered up in the middle first, and that this nematic order has spread towards the interfaces as the temperature is lowered. Since there is no interfacial ordering at these temperatures, the liquid vapour interfaces can induce no preferred direction upon the ordered bulk (though it should be noted that now two isotropic-nematic interfaces have been set up, which could be alignment inducing). The negative regions in the associated Q_{zz} profiles give a weak indication that this nematic domain is tilted with respect to the z-axis. This could be attributed to a preferred alignment associated with the implicit nematic-isotropic interfaces. However, the values of $\bar{Q}_{zz}$ measured over all particles (Fig 5.8) are zero to within error estimates for all but one $T^* \geq 0.470$. It is suggested, therefore, that the alignment adopted at this intermediate temperature is arbitrary and there is no preferred direction for the bulk ordering.

At the slightly cooler temperature of $T^* = 0.470$, the nematic order spreads to the edges of the film and would be expected to order up perpendicular to the interfaces. However, observation of the time evolutions of P_2 and Q_{zz} at this temperature (Fig 5.13) indicate that although an initial large increase in *normal* ordering is observed, this is a quenching effect caused by cooling the system so close to the
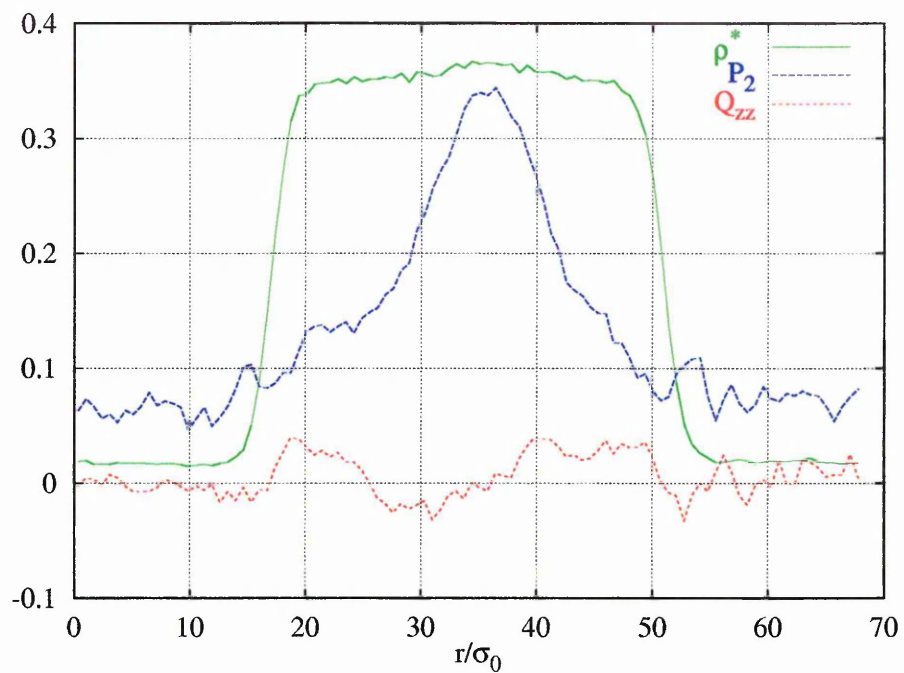
Figure 5.11: Order parameter profile at $T^* = 0.475$
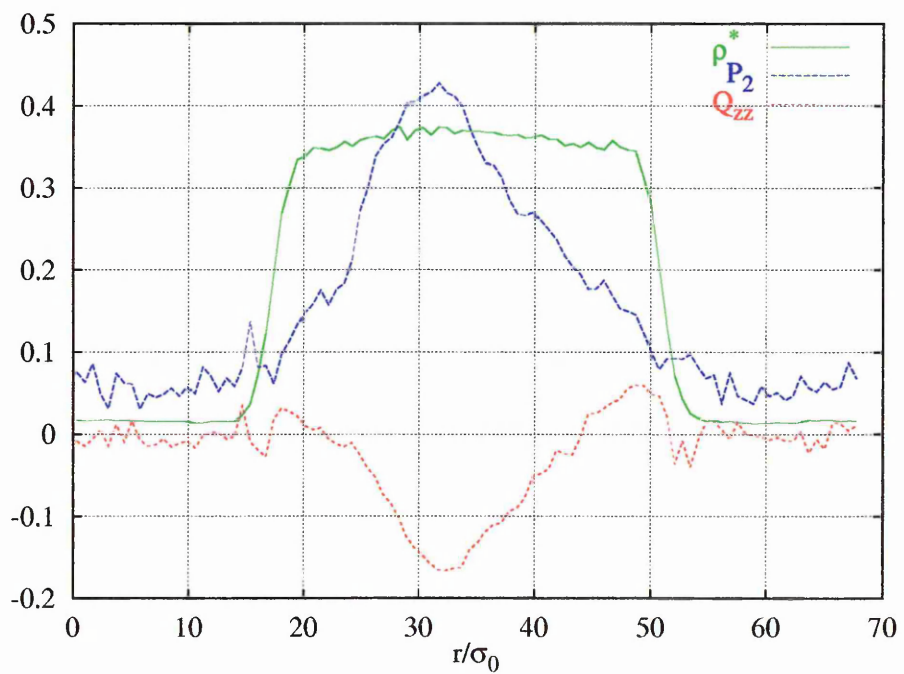
Figure 5.12: Order parameter profile at $T^* = 0.473$

phase transition; given sufficient time to equilibrate, the system settles into an ordered system with a low Q_{zz}. Even in this equilibrated period, oscillations are seen to occur on timescales of order 10^5 timesteps. Animations of the runs in the intermediate temperature regime (i.e. $0.460 \leq T^* \leq 0.475$) indicate that at any instant, far from there being a single central nematic domain, the system typically comprises a series of competing domains. These are commonly seeded near to the film centre before propagating towards the interfaces, at which they disperse.
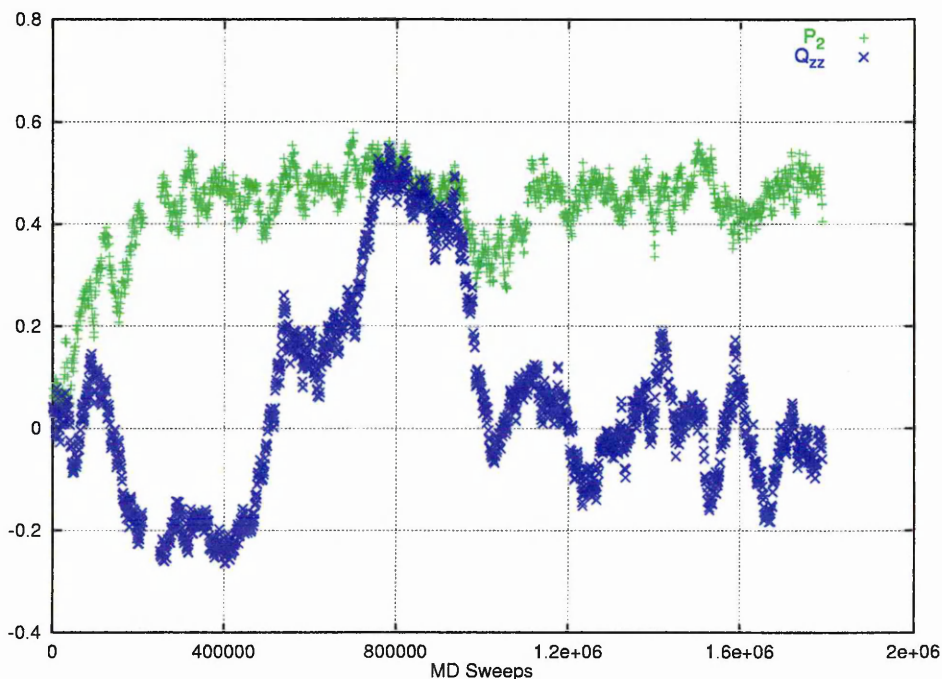
Figure 5.13: Order parameter evolutions at $T^* = 0.470$

To demonstrate this process, sub-run averages are presented of the $P_2(z)$ and $Q_{zz}(z)$ profiles for $T^* = 0.470$ (Fig 5.14). Compiled over relatively small time periods (50,000 timesteps) for consecutive stages of the production run at this temperature, these show the existence of different nematic domains as regions with similar $Q_{zz}(z)$ values, with changes in the value of $Q_{zz}(z)$ corresponding to the twist that is adopted by the film between these domains. The sequence of profiles here show an initial

two domain arrangement, with a gradual spatial reorientation occuring between the domains. In profile (b), the right-hand domain can be seen to have grown significantly, whilst profile (c) shows that it goes on to split in two. The final profile shows that these domains of positive Q_{zz} then disperse as the centre of the film develops a tilted domain. Orientational fluctuations of this type were observed to occur continually at these intermediate temperatures.
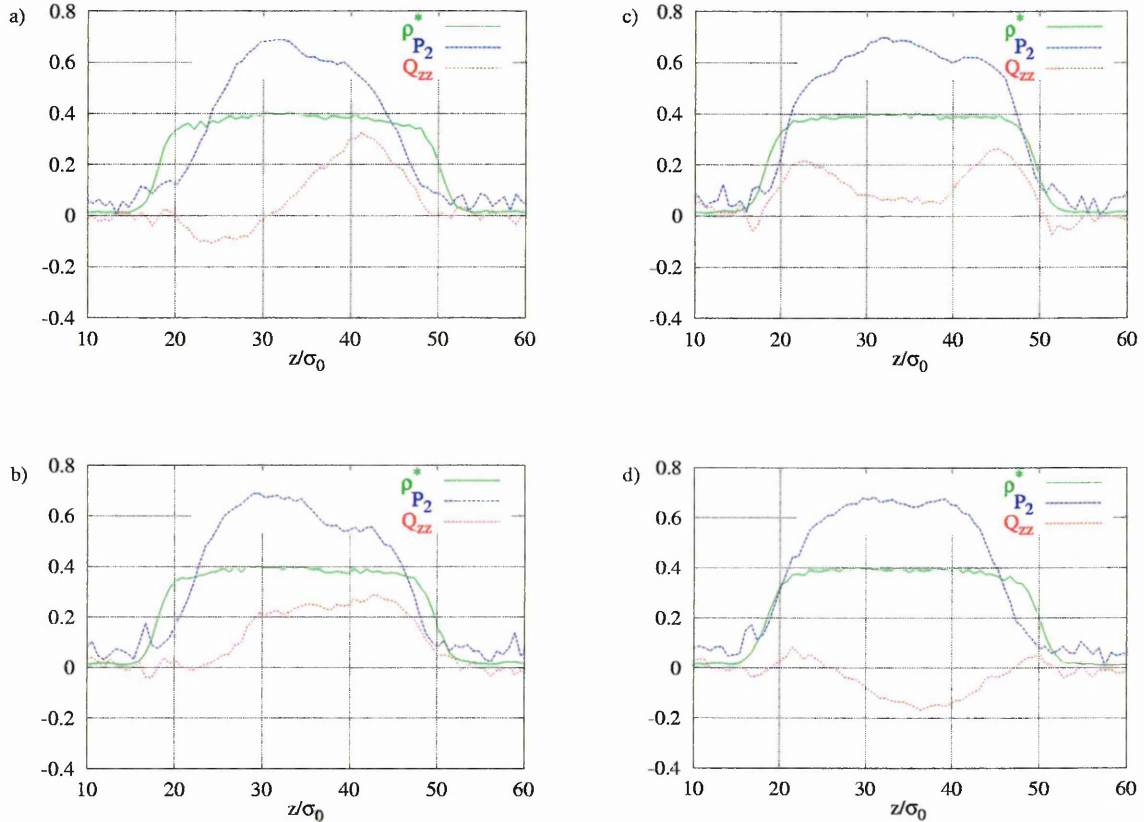

Figure 5.14: Sub-run profiles

The corresponding $P_2(z)$ profiles are relatively insensitive to the domain boundaries (note that in calculating these, only the particles within the relevant slice are considered, so the effects of any gradients in the director are not included directly). However, they *do* all show a relative disordering at the liquid-vapour interface. The density profiles, $\rho(z)$ are virtually independent of the changing orientational domain

140
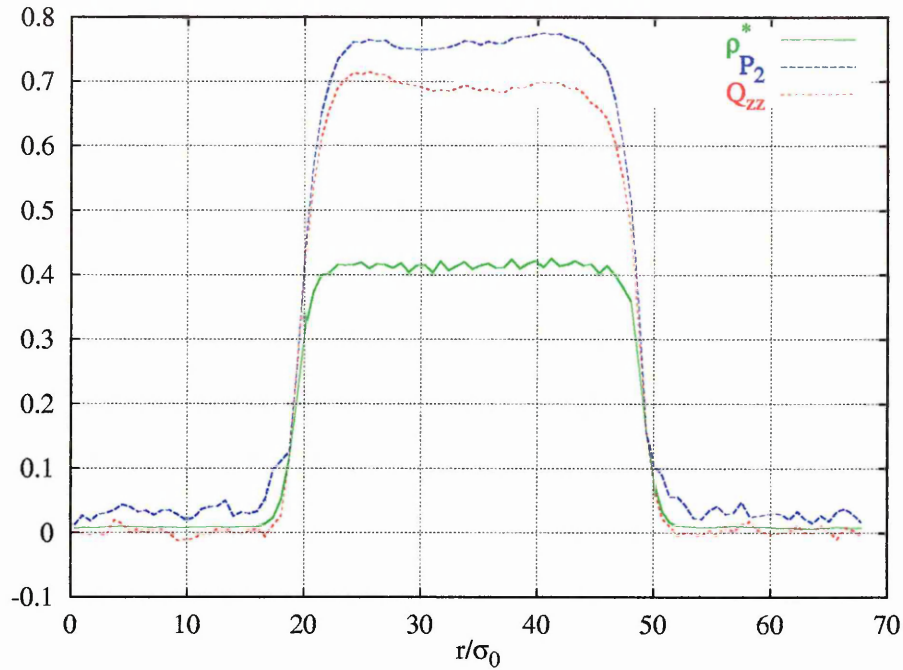
Figure 5.15: Order parameter profile at $T^* = 0.450$

structure.

Progressing further into the nematic range, the $\bar{Q}_{zz}$ values increase, indicating that the nematic has a preferred direction of alignment *normal* to the free interfaces. This can be quite easily verified by looking at the corresponding profiles and configuration snapshot (Figs 5.15 and 5.16). It follows that this direction must be induced by the interfaces, since there should be no preferred direction in the bulk.

Note that the degree of perpendicular order indicated by the ratio of order parameters reaches a maximum, at $T^* \simeq 0.450$. Upon further cooling, this ratio decreases slightly, before the system undergoes what appears to be a first order phase transition at $T^* = 0.440$. The high orientational order parameters at this temperature (Fig 5.17) indicate a highly ordered system and a layered structure is clearly visible from the appropriate snapshot (Fig 5.18), with hexagonal packing evident in the

141
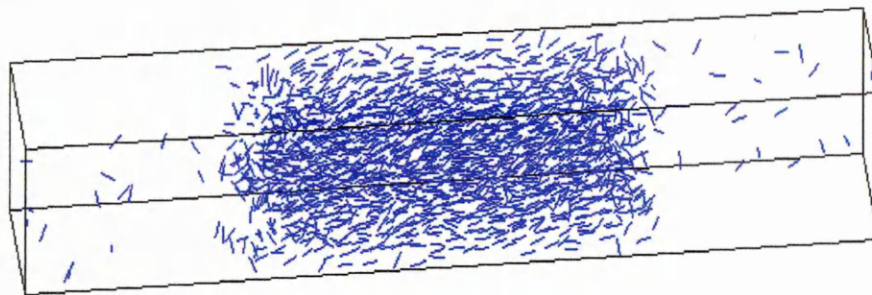
Figure 5.16: Configuration snapshot at $T^* = 0.450$

layers. This structure appears to be a crystalline solid whose layers are slightly tilted with respect to the interface normal, contrary to the preferred direction in the nematic phase. It is suggested that this tilt is due to the box dimensions originally chosen being incommensurate with the hexagonal layers, stopping the system from ordering perpendicularly and forcing it to adopt a tilted arrangement. This also explains why the degree of perpendicular ordering starts to decrease in the nematic phase: as the crystal phase is approached, competition develops between the interfacial and boundary-condition contributions to the preferred system orientation. The boundary conditions also explain the apparent partial layers observable at the interfaces (Fig 5.18). It is tempting to suggest that had the box dimensions been allowed to change (whilst keeping the overall volume constant) the system would have found its truest lowest energy state with perpendicular ordering in the crystal phase. However the energy penalty associated with interface formation would have most likely resulted in the system tending towards a very long, highly anisotropic box, in an attempt to minimise the cross sectional (ie interfacial) area.
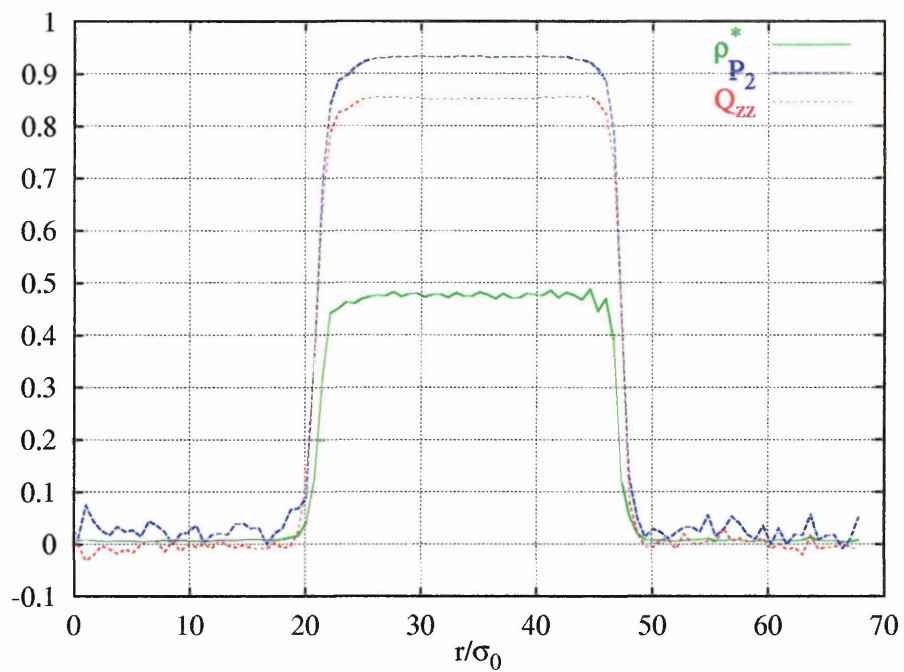
Figure 5.17: Order parameter profile at $T^* = 0.440$
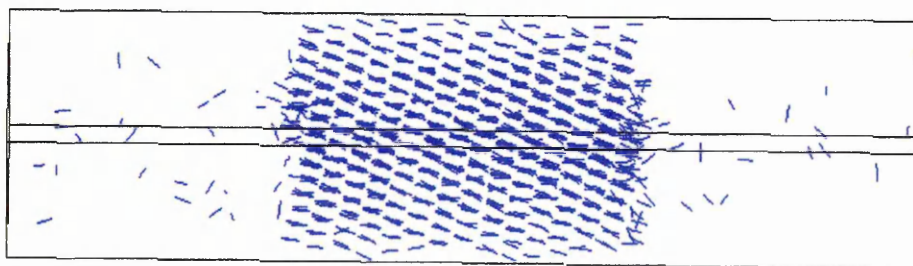
Figure 5.18: Configuration snapshot at $T^* = 0.440$

143

5.3.2 Orientational Correlations

Although P_2 is useful as an overall guide to the state of the system, as well as being particularly convenient here when used to profile the simulation box, a more rigourous quantitative measure of orientational order can be made using the second rank order pair correlation function, $g_2(r)$. This measures how the orientational correlations between molecules decay with distance, and is given by

$$g_2(r) = \frac{\sum_{ij} P_2\left(\hat{\mathbf{u}}_i \cdot \hat{\mathbf{u}}_j\right) \delta(r_{ij} - r)}{\sum_{ij} \delta(r_{ij} - r)} \tag{5.6}$$

where the molecules i and j are separated by a distance r_{ij}. In the isotropic phase, $g_2(r)$ decays to zero at large r, whereas in the nematic phase it levels out at a value equal to the square of P_2. In this case $g_2(r)$ has been measured for all pairs of molecules where both are within the bulk of the film. This bulk is defined as being the central portion of the film, excluding regions within 10 interfacial thicknesses of the interfaces (obtained from the hyperbolic tangent fitting). It was observed that at the edges of this bulk the density profile was still reasonably flat for all of the temperatures at which $g_2(r)$ was calculated. The values obtained are shown (Fig 5.19).

The four temperatures correspond to the range over which orientational order developed within the film, as indicated by the nematic order parameter, P_2 (Table 5.6). As would be expected, the functions decay to higher values as the temperature is decreased, due to the increased orientational correlations. Unfortunately, for the three lowest temperatures shown, the function is still decaying slightly at the maximum
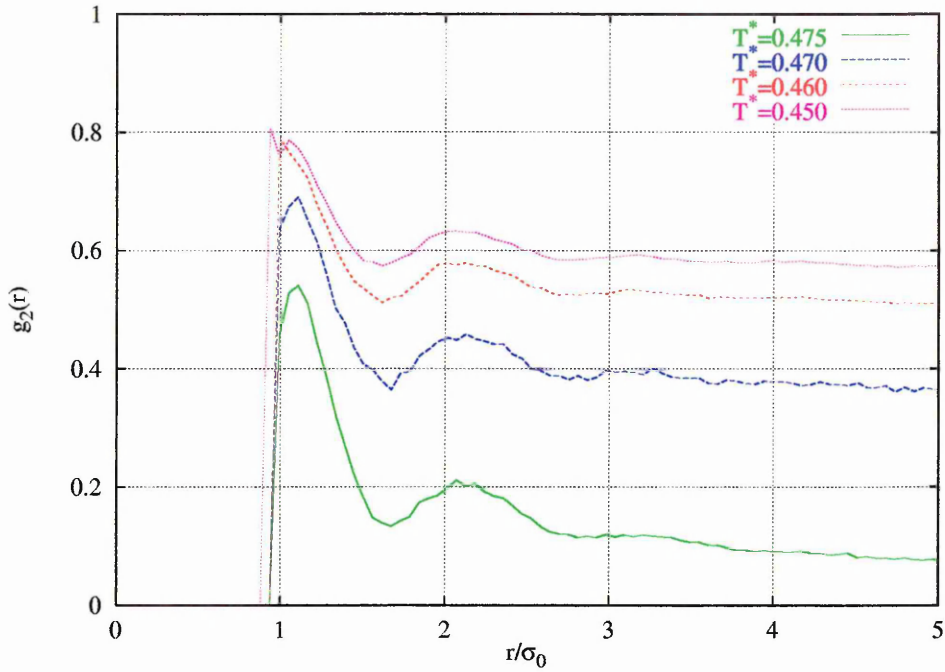
Figure 5.19: $g_2(r)$ at various temperatures

distance shown, and it is difficult to discern any real difference between the gradient

of the functions, especially for $T^* = 0.450$ and $T^* = 0.460$. This makes it difficult

using this function to determine at what temperature a true nematic monodomain

occurs, since values can only be obtained up to a maximum distance of half the

box-width in the x and y directions, which is too short for any required levelling out

of the function to be definitely said to occur. An alternative method of measuring

the orientational correlations at longer distances is therefore required, two of which

are presented next. It is worth noting in passing, however, that the values to which

$g_2(r)$ has decayed, even at this relatively short distance, are in good agreement with

the square of P_2 *as measured in the centre of the corresponding profiles, not the*

observable over all particles (since $g_2(r)$ has been calculated only in the bulk of the

film). For $T^* = 0.475$ the profile (Fig 5.11) has a central P_2 of ~ 0.3, squaring

to 0.09 cf $g_2(r = 5\sigma_0) \sim 0.1$; at $T^* = 0.470$ the sub-run profiles (Fig 5.14) have a

145

central P_2 of ~ 0.6, squaring to 0.36 cf $g_2(r = 5\sigma_0) \sim 0.35$; and the $T^* = 0.450$ profile (Fig 5.15) has a central P_2 of ~ 0.76 squaring to 0.58 cf $g_2(r = 5\sigma_0) \sim 0.58$.

As mentioned previously, orientational fluctuations have been observed in this system by looking at animations of the simulation. It was clear from these that at some intermediate temperatures a number of nematic domains were being formed, generally moving from the centre of the film towards the interfaces before dispersing. On cooling through the intermediate temperature regime, two trends were apparent from the animations: i) an increase in the size and lifetime of the nematic domains formed; ii) a decrease in the thickness of the disordered interfacial regions. In an attempt to provide a more satisfactory measure of the former, the correlations between the instantaneous nematic directors, $\hat{\mathbf{d}}(z)$, for each slice of the liquid film (as calculated in the $P_2(z)$ routine) have been calculated. Designated $D_2(d_z)$, this is formally expressed as

$$D_2(d_z) = \left\langle P_2\left(\hat{\mathbf{d}}(z) \cdot \hat{\mathbf{d}}(z \pm d_z)\right)\right\rangle' \tag{5.7}$$

where the prime on the angled brackets denotes an average restricted to the slices within the liquid region of the film.

The behaviour of $\langle D_2(d_z)\rangle$ for various temperatures around the ordering transition is shown (Fig 5.20).

For the highest temperature, $T^* = 0.500$, $\langle D_2(d_z)\rangle$ quickly decays to zero and the system is clearly isotropic. Correspondingly, at the lowest temperature shown, $T^* = 0.450$, $\langle D_2(d_z)\rangle$ decays slowly, levelling out at a value of approximately 0.85, at
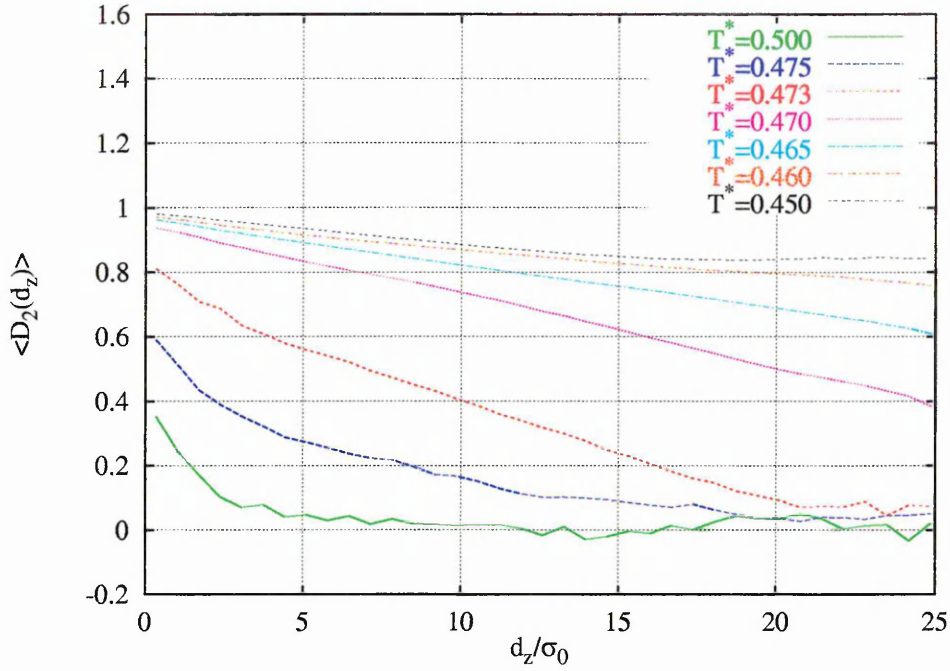
Figure 5.20: $\langle D_2(d_z) \rangle$ at various temperatures

$d_z \simeq 15\sigma_0$. This agrees well with the identification in the previous section of this phase as a stable nematic monodomain. At the other temperatures shown, $\langle D_2(d_z) \rangle$ drops approximately linearly with d_z, only levelling off in the cases where it drops all the way to zero. This slow decay in orientational correlations is not consistent with that seen in simulations of bulk systems, where typically a much shorter decay to a limiting value is seen in $g_2(r)$ [47, 90] suggesting that the disordering interfaces present in this system strongly modify the ordering process. Since the correlations between molecules in the film can only be measured up to a distance as thick as the film itself, the behaviour of $\langle D_2(d_z) \rangle$ at larger values of d_z can only be examined using a thicker film, which is presented in the next section.

Since $\langle D_2(d_z) \rangle$ gives an indication of the degree of orientational correlations in the z direction ie *normal* to the interfaces, it was decided to obtain a measure of the

147

planar order, firstly by dividing the system into 20 slices at regular z values and calculating $g_2(r)$ (Eqn 5.6) for each slice (i.e. the sums in eqn(5.6) were restricted to pairs of particles within the appropriate slice). This gave the function $g_2(r, z)$, where r is the particle-particle separation, and z is the location of the slice within the film. Since it is calculated in thin slices, $\langle g_2(r, z) \rangle$ provides a useful measure of the degree of orientational correlations *planar* to the interfaces. The number of slices was restricted to 20 in order to obtain reasonable statistics. The $\langle g_2(r, z) \rangle$ data are shown as surface plots for $T^* = 0.475, 0.473, 0.470, 0.450$ (Fig 5.21). At higher temperatures, $\langle g_2(r, z) \rangle$ was found to decay rapidly to zero at all z, indicating a film of isotropic liquid.
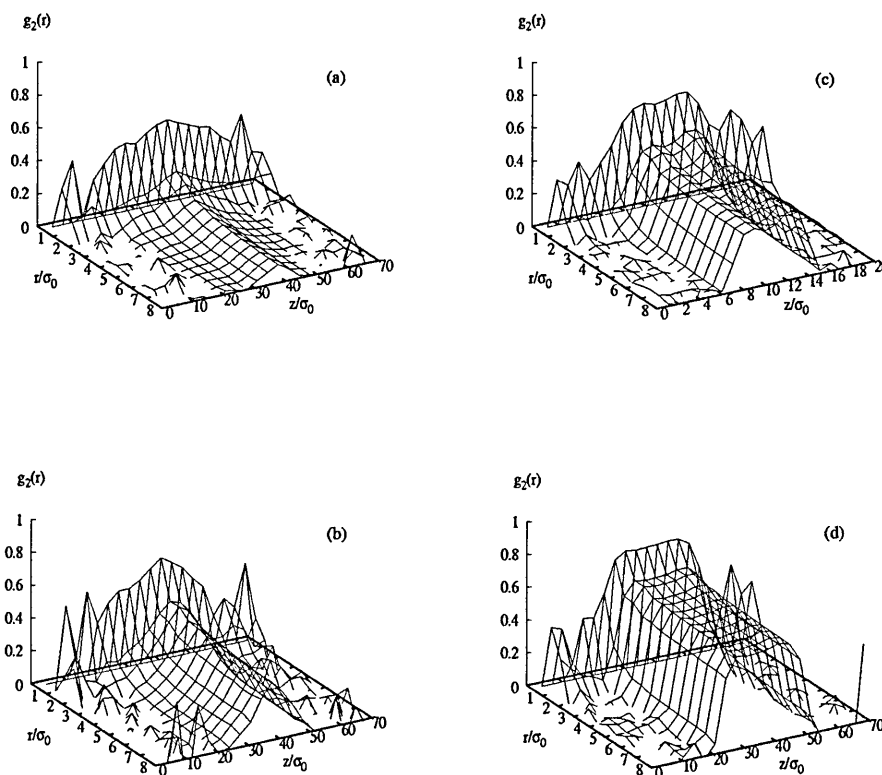

Figure 5.21: $g_2(r, z)$ at $T^* =$ (a) 0.475; (b) 0.473; (c) 0.470; (d) 0.450

At the highest temperature shown, $\langle g_2(r,z) \rangle$ decays to values slightly greater than zero in the middle of the film, corresponding to a small degree of central nematic order (as seen previously in the order parameter profiles). This effect is more noticeable at $T^* = 0.473$, where the magnitude of the limiting value is higher and the width of the ordered region is increased. At $T^* = 0.470$ this ordering has spread nearly to the edge of the film, but is not quite as wide and is much less sharply defined than the equivalent data obtained for the nematic monodomain at $T^* = 0.450$.

It can be seen that for $T^* = 0.470$ that this *planar* ordering is reasonably stable, $\langle g_2(r,z) \rangle$ levelling out across much of the film. By contrast, however, $\langle D_2(d_z) \rangle$ at this same temperature (Fig 5.20) indicates that orientational correlations *normal* to the interface continue to decay at large d_z. Indeed, the behaviour of $\langle D_2(d_z) \rangle$ suggests that nematic-like orientational correlations in the z direction develop only for $T^* \leq 0.450$.

This picture is confirmed by looking at the molecular correlations calculated using $g_2(r)$ (Eqn(5.6)) in the bulk region of the film, and resolved in the *planar* $g_2^{xy}(d)$ and *normal* $g_2^z(d)$ directions. This simply involves replacing the absolute distance r (Eqn 5.6) with either the planar or perpendicular distance between the molecules under consideration. The *planar* version is limited to distances of half the box width or less, since no two molecules can be a *planar* distance of more than half a box width apart. However the *normal* values can be calculated for much larger distances, since the film is longest in the z direction. Their behaviour at various temperatures around the transition are shown (Fig 5.22) - the shorter ranged function at each temperature is the *planar* resolution.
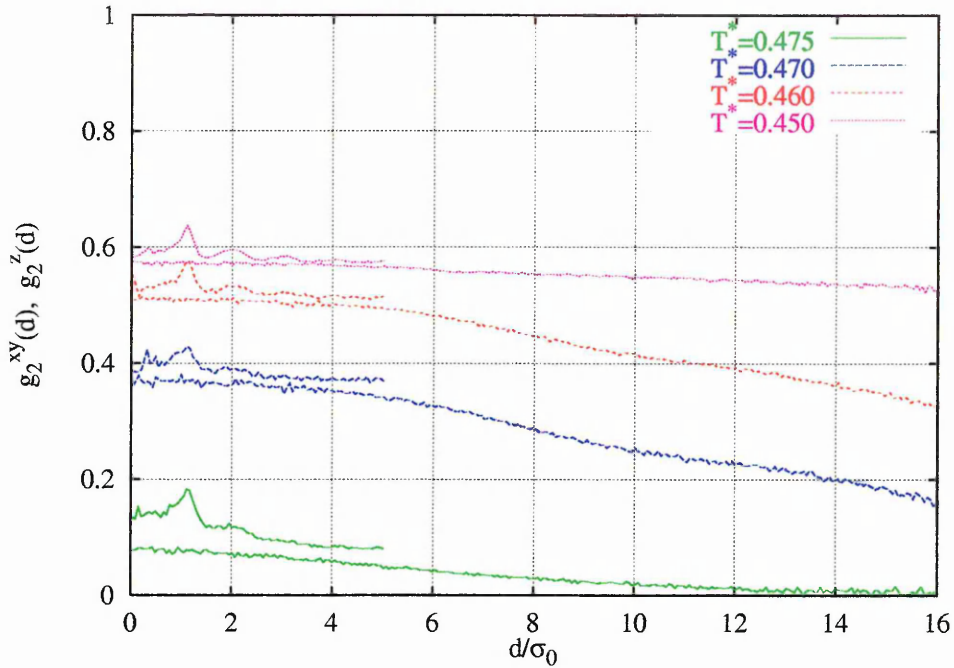
Figure 5.22: Resolved $g_2(r)$ at various temperatures (short lines are $g_2^{xy}(d)$, long ones $g_2^z(d)$)

At the highest temperature shown, $T^* = 0.475$, it is difficult to tell if $g_2^{xy}(d)$ has levelled out to a positive limiting value, indicative of nematic ordering. The value is relatively low compared to that seen in bulk nematics anyway, which would seem to indicate that this corresponds to some local orientational ordering rather than a true nematic. Certainly though $g_2^z(d)$ decays much faster, eventually tending to zero. Thus the difference between the *planar* and *normal* ordering is quite clearly illustrated. At lower temperatures, $g_2^{xy}(d)$ can be clearly seen to have levelled out to a positive value, indicating *planar* nematic ordering, while $g_2^z(d)$ continues decaying over unusually long lengths in a similar fashion to $\langle D_2(d_z) \rangle$. What is noticeable is that the difference between the two types of ordering decreases as the temperature is lowered, until, at $T^* = 0.450$, it is barely significant, corresponding to the *normal* and *planar* ordering becoming equivalent in the nematic monodomain.

The perpendicular and parallel components of the orientational ordering were also analysed by calculating the two dimensional function $g_2^*(d_{xy}, d_z)$, ie g_2 as calculated in Eqn 5.6 but stored as a function of both planar (xy) and perpendicular (z) distances. This shows the decay of g_2, and so the decay of the orientational correlations over all directions - it is best viewed as a contour plot rather then a 3d surface, since the viewing perspective can make it difficult to see exactly what the function is decaying to. However, this can simply be read off from the contours. Two such plots are shown, for $T^* = 0.475$ (Fig 5.23) and $T^* = 0.470$ (Fig 5.24). The first shows quite clearly that the correlations quickly decay to zero at around $3\sigma_0$ in all directions, confirming previous evidence that the film is isotropic with respect to both *normal* and *planar* ordering. However, at the slightly lower temperature of $T^* = 0.470$, g_2 decays quite clearly to a non-zero value between 0.3 and 0.4 in the xy direction, again indicating *planar* nematic order, whilst correlations in the *normal* direction decay smoothly with distance.

This marked difference between the *normal* and *planar* orientational correlations is presumably due to the symmetry breaking effect of the interfaces. It appears that high temperature nematic growth is stabilised by the in-plane periodicity of the system. Longitudinal correlations, conversely, are less easily established due to the inherently disordered interfaces: hence the domains of nematic order formed through strong *transverse* correlations fail to spread throughout the system. Only at temperatures sufficiently low to stabilise orientational order at the interfaces does the system become nematic in all three dimensions.
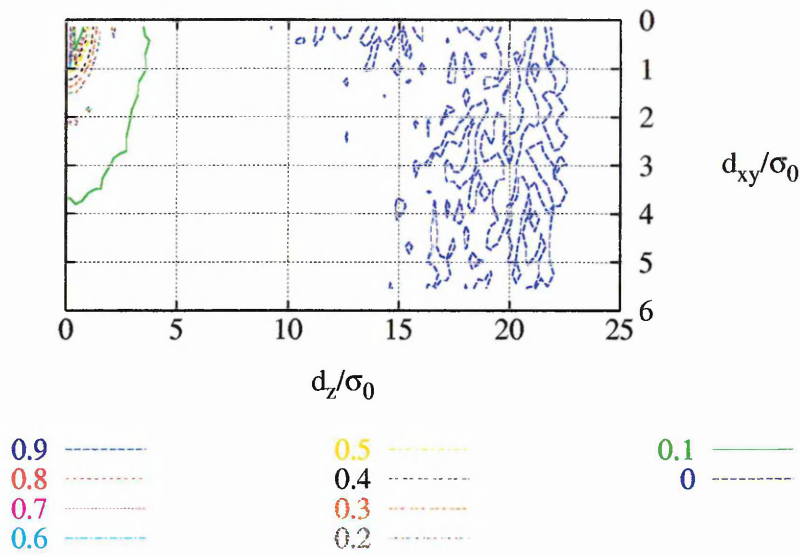
Figure 5.23: $g_2(d_{xy}, d_z)$ contour plot - $T^* = 0.475$
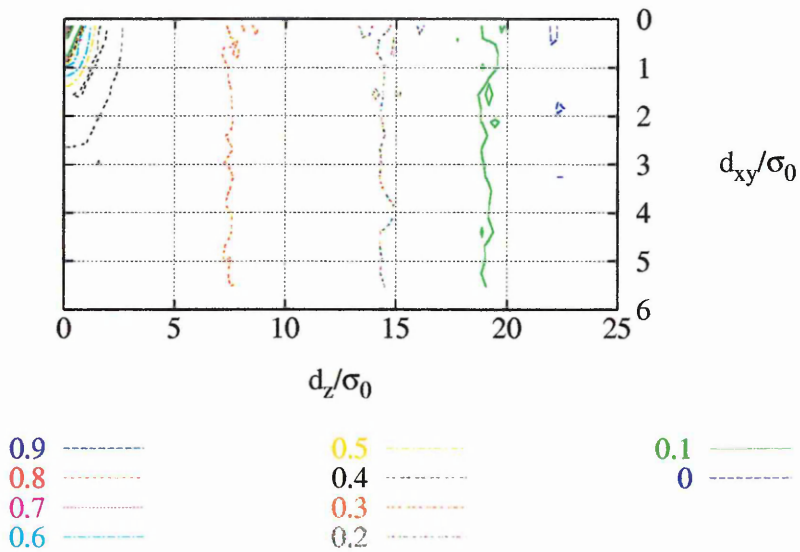
Figure 5.24: $g_2(d_{xy}, d_z)$ contour plot - $T^* = 0.470$

As was stated earlier, the surface tension at each temperature was obtained by calculating the *normal* and *transverse* components of the pressure tensor (Eqns 5.3,5.4) and using them in the integral defined in Eqn 5.5. The values for each of these pressure tensors, the difference between them and the integral are shown for three temperatures in Figs 5.25 Strictly speaking, the *normal* component should fluctuate around the bulk pressure [120] and show no structure apart from these fluctuations. As can be seen, this is true for the vapour and liquid regions far from the interface; however in the interfacial region a minimum on the vapour side and maximum on the liquid are clearly visible. This is attributed to the method used to construct the tensor values i.e. Harasima's definition [119], as has been stated elsewhere [44]. From the condition of hydrostatic equilibrium, it follows that the two components of the pressure tensor must be equivalent and equal to the bulk pressure in the bulk liquid and vapour phases. This is true for all the temperatures shown, ignoring local fluctuations. The values for the *transverse* component have the expected structure at the interface, and it is this which is the main contributor to the surface tension via the integral expression. The final graph shows the cumulative surface tension values; they show a reasonably stable profile across the bulk regions, indicating the system has reached equilibrium [100]. The final limiting value is equal to twice the surface tension value at each temperature, since the integral occurs over two interfaces.

The surface tension values calculated as above for each temperature are shown (Fig 5.26), along with error-bars at temperature intervals of 0.1. These errors were es-
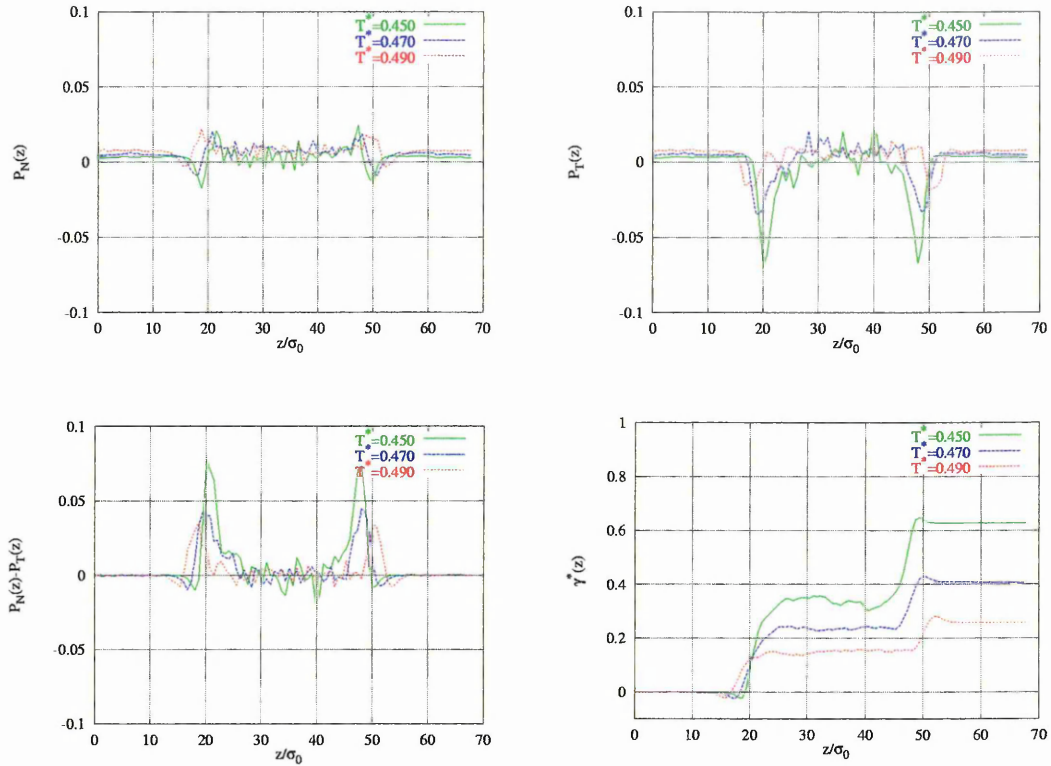
Figure 5.25: Pressure tensors, differences and surface tension integrals

timated by using a block averaging technique, each production run consisting of at least 20 blocks of 10,000 timesteps each, as for the bulk observables.

The values in the vapour-isotropic ($0.480 \leq T^* \leq 0.520$) and vapour-nematic ($0.445 \leq T^* \leq 0.460$) regions show the expected inverse correlation with temperature, with $\langle \gamma^* \rangle$ decreasing linearly as the temperature is increased and the surfaces become less rigid. As orientational order grows, a large increase in $\langle \gamma^* \rangle$ is observed, consistent with theoretical predictions for surface disordering systems [32]. The temperature dependence of the rapid rise in $\langle \gamma^* \rangle$ closely matches that of the nematic order parameter $\langle P_2 \rangle$. Thus, we note that the film's overall surface tension is considerably enhanced even at temperatures (e.g. $T^* = 0.470$) for which there is little or no orientational order *at* the liquid-vapour interface. This enhancement is

154
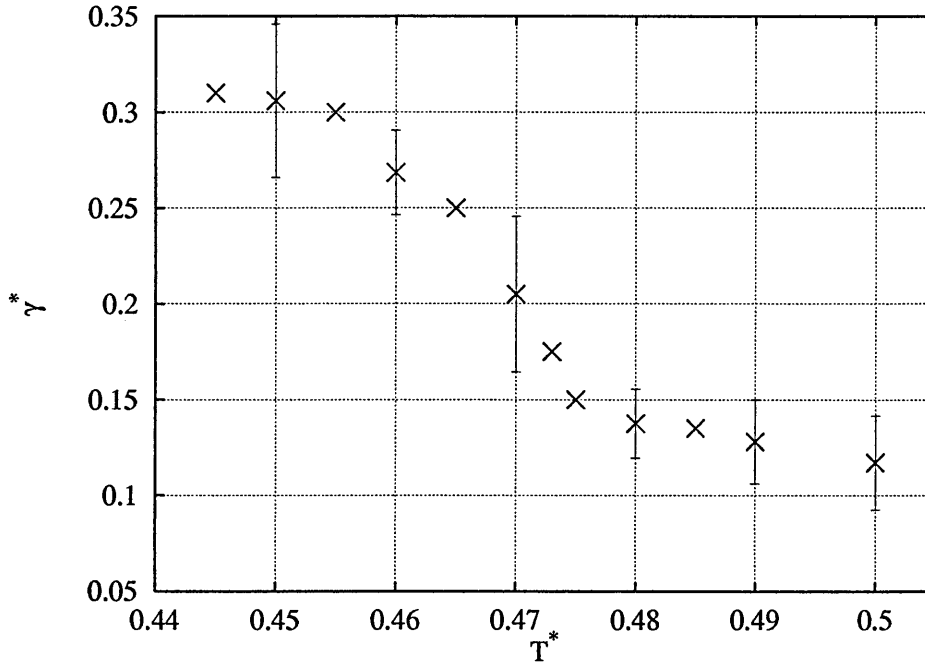
Figure 5.26: Surface tension for various temperatures

presumably due to the additional N-I interfaces (along with any nematic-nematic ones) present at these temperatures, which contribute to the surface tension because of the integral nature of the calculation, which is over the whole width of the film. Whilst theoretical treatments of this situation attribute the jump from the I-V to the N-V branches of the surface tension to such additional interfaces, it cannot be used to measure γ_{NI}^* directly; a fuller picture of the wetting behaviour (partial or complete) displayed by the system is needed first.

As well as showing the expected temperature dependence, our surface tension data compare well with the values obtained in a previous GB thin film simulation [44]. Although this used a different parameterisation which will obviously affect the sur-face tension behaviour, the well-depths are still of approximately the same order of magnitude, and thus γ^* should also be. The $\langle \gamma_{IV}^* \rangle$ values reported here are slightly

lower (0.05 - 0.15 c.f. 0.15 - 0.25) but this is to be expected since the particles here are shorter and will thus lead to less rigid interfaces. For $\langle \gamma^*_{NV} \rangle$, the difference is very small (approx 0.3 c.f. 0.25-0.35); it is possible that the presence of orientational order is a more predominant factor in the surface tension than the molecular length, and as it increases the two systems therefore adopt more equivalent values.

In conclusion, the medium sized system has shown a rich behaviour - in particular the decoupling between the *normal* and *transverse* correlations was an interesting result. Attention will now be switched to the largest system studied, with emphasis placed on the system size effects observed.

5.3.3 Summary

The medium sized system has shown a rich behaviour - as expected qualitatively similar to the small system, but with a marked shift in the transition temperature and ordering regime. Stable isotropic and nematic-vapour coexistence were again both seen, with homeotropic anchoring at the nematic free surface and the establishment of a monodomain at lower temperatures in the nematic phase, but whereas in the small system a significant rise in the bulk nematic order parameter was not seen until $T^* = 0.460$, for the medium system this occured at the higher temperature of $T^* = 0.470$. A much wider temperature range between this onset of nematic ordering and the establishment of a nematic monodomain was also observed, during which significant orientational fluctuations were seen across the film. These have been extensively analysed here, probably the most interesting finding being the decoupling between the *normal* and *transverse* correlations, and the particularly long

range of the former. This analysis was continued on a larger system, as detailed in the next section.

5.4 Large System

The largest system studied consisted of 7104 GB particles in a significantly elongated box, having relative dimensions 22:1:1 ($262.1\sigma_0$:$11.9\sigma_0$:$11.9\sigma_0$). The simulations were conducted using the parallel Gay-Berne MD code GBMESO [121] which was made available by the High Performance Computing Initiative (HPCI) consortium on *Simulation and Statistical Mechanics of Complex Fluids.*

GBMESO uses a replicated data parallel technique, where the force calculation and moving routines are split between the nodes equally according to the particle number. This was thought to be more appropriate than the domain decomposition technique, where the system volume itself is divided up and each node simulates a different domain. The large degree of inhomogeneity in the system being studied here would result in unequal loading of the processors and thus inefficiency using the latter technique.

The initial configuration was prepared in a similar fashion to that described for the smaller systems, resulting in a relatively wide liquid film, $\approx 140\sigma_0$ or 70 molecular lengths. Simulations were commenced at a temperature of $T^* = 0.520$, which was known to be right on the border of the isotropic-nematic transition for the bulk system and could be reasonably expected to still be isotropic for the interfacial system. The progress of the system was measured in a similar fashion to before,

various observables being measured over all particles and also profiled across the box width to measure the degree of ordering within each part of the film.

The progress of the potential energy per particle and the overall nematic order parameter at each temperature is shown (Figs 5.27,5.28). It is clear from the energy evolution that even at high temperatures long run times were required to bring the system to equilibration; unfortunately, due to the computational cost of these simulations, the runs often had to be curtailed before it was certain equilibrium had been established. The long timescales associated with orientational ordering seemed to be particularly problematic, and it was decided relatively early in this series of simulations to quench the system quite quickly down to a low temperature, thought to correspond to a nematic monodomain. Once established, this monodomain was considered a good starting point when seeking equilibration at higher temperatures. The correlation functions were calculated for all equilibrated runs and compared with those for the moderate system.

A more detailed description of the simulations undertaken on the cooling run is now given. At the starting temperature, $T^* = 0.520$, stable isotropic-vapour coexistence was observed, and the system relatively quickly cooled, with reasonably long runs being used in the hope of bringing the system close to equilibrium before proceeding to the next, lower temperature. No orientational ordering was observed down to $T^* = 0.485$ - a profile of the order parameters for this and the highest temperature is shown (Fig 5.29). The profiles were averaged over a relatively short time period (100,000 sweeps) and thus are rather noisy. They do, though, quite clearly show that the whole of the film was isotropic at these two temperatures.
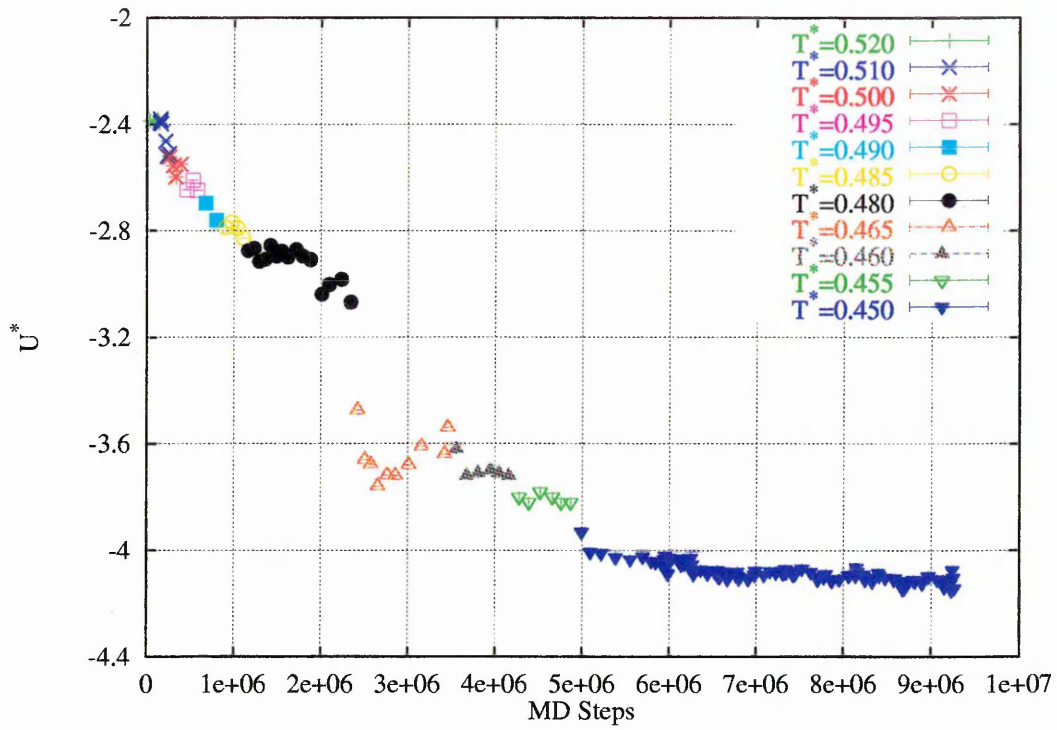
Figure 5.27: Potential energy evolution during cooling run
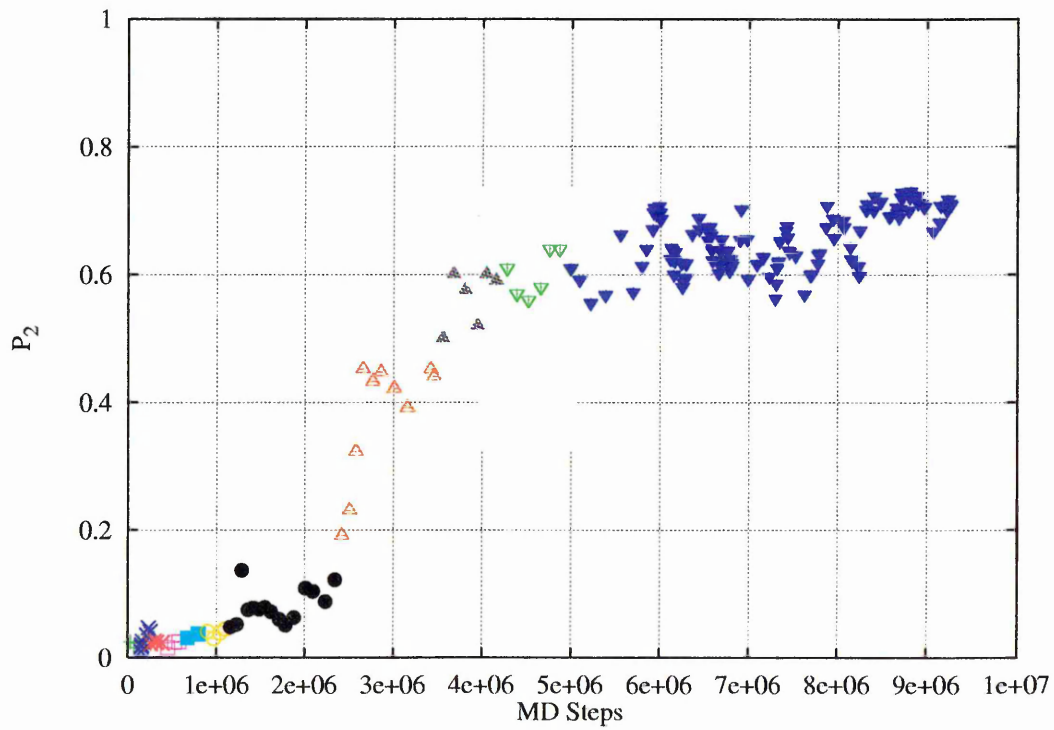
Figure 5.28: Nematic order parameter evolution during cooling run

159
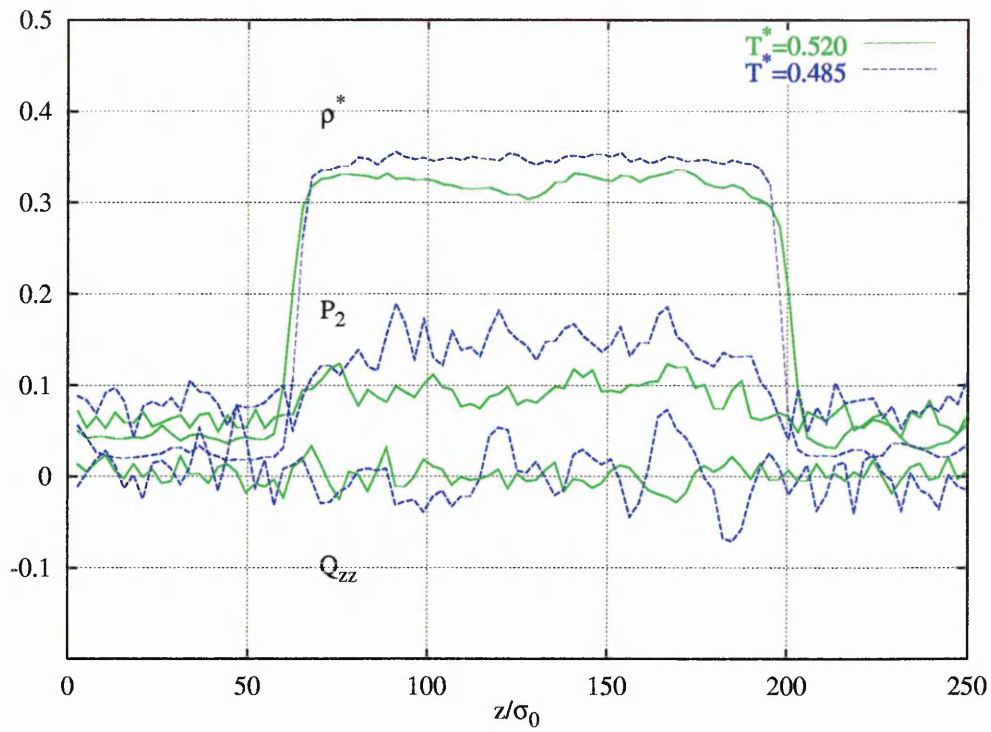
Figure 5.29: Order parameter profiles at $T^* = 0.520, 0.485$
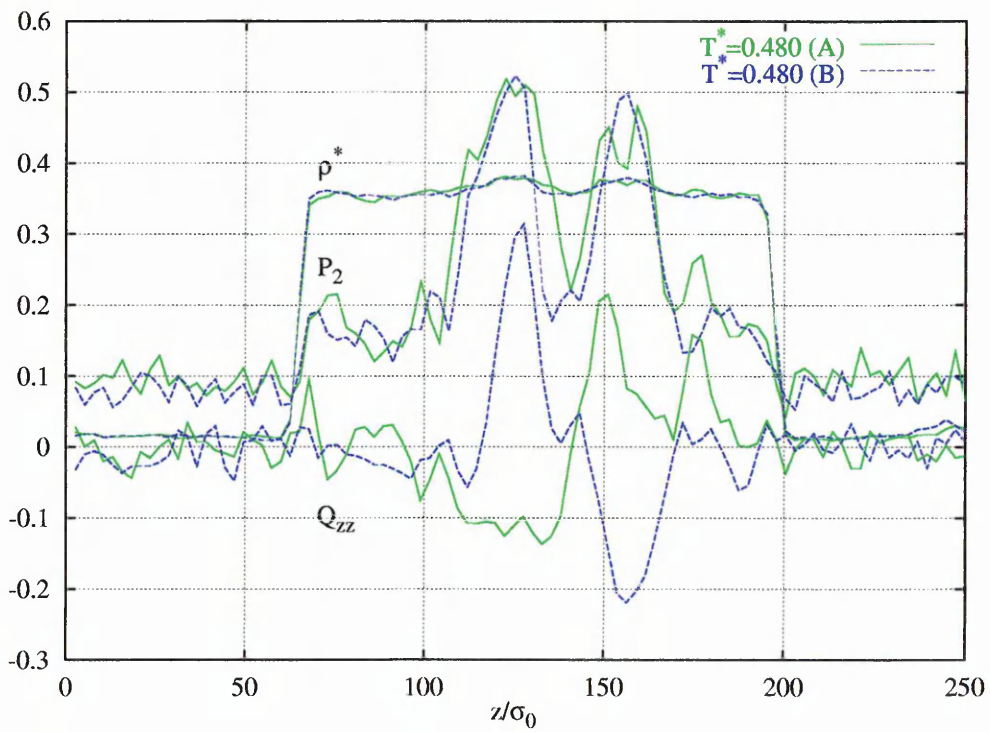
Figure 5.30: Order parameter profiles at $T^* = 0.480$

160

Upon further cooling to $T^* = 0.480$, much greater fluctuations were observed in the order parameters across the film, accompanied by corresponding density modulations. After running for a significantly longer time at this temperature ($\approx 1,000,000$ MD timesteps) the potential energy was observed to still be decreasing, and the aforementioned large fluctuations to still persist. An illustration of the dynamic state of the system at this temperature is provided by the two profiles in Fig 5.30, which were averaged over two consecutive blocks of 70,000 steps. The system consists of two central orientationally ordered domains, shown quite clearly by the two peaks in $P_2(z)$ and having different preferred directions as indicated by the values of $Q_{zz}(z)$. However, after 70,000 steps these $Q_{zz}(z)$ values have reversed, indicating these domains to be rapidly changing alignment relative to each other. Attempts to slowly cool this system further still resulted in continued significant orientational fluctuations. Domains were formed and dispersed as previously and the overall energy dropped very slowly. Abandoning this approach, it was decided instead to rapidly cool the system from a judiciously chosen configuration at $T^* = 0.485$, with a relatively large degree of positive Q_{zz} ie. perpendicular ordering. This configuration was chosen since it offered the system a clear route to the state adopted by the smaller systems at a low temperature in the nematic phase of a perpendicularly ordered monodomain.

The profile of the configuration at $T^* = 0.480$ used as the starting point for the quenched run is shown (Fig 5.31). It comprises three nematic domains, the two nearest the interfaces showing a significant degree of perpendicular ordering. It was hoped that upon rapid cooling, the interfacial order would increase as for the medium sized film, and that this perpendicular ordering would spread to the middle

of the film. Evolution of the Q_{zz} profile at $T^* = 0.465$ is shown (Fig 5.32), after (A) 200,000 and (B) 500,000 MD Steps, along with the starting profile (E). Upon first cooling to $T^* = 0.465$, the potential energy dropped quite significantly, and the order at the free interfaces did indeed increase. However, this was a short lived phenomenon, and after a small time the order at the left hand surface decreased again. It is noteworthy, however, that there is relatively little fluctuation with time of the $Q_{zz}(z)$ values compared with that witnessed over a much shorter timescale at $T^* = 0.480$ (Fig 5.30). This slowing down of the domain fluctuations with decreasing temperature was also observed in the medium sized system.

Upon further cooling, relatively little change in the profiles was seen, except for these long timescale fluctuations, until $T^* = 0.450$ was reached. Here a very slow realignment of the film was observed, occurring over several million timesteps. The evolution of the Q_{zz} profile is presented at 500,000 step intervals (Figs 5.33,5.34), (shown in alphabetical order) and gives a reasonable indication of how ordering within the film actually progressed.

At early times, the most obvious feature is the enhanced perpendicular ordering at the interfaces, which slowly spreads in from the left hand side of the film. Rather than extending all the way across the film though, this then retreats as order spreads in from the right hand side, leaving a domain of parallel ordering within the centre of the film. This is then slowly destroyed by both sides as the order moves in once more, and the film finally evolves into perpendicularly ordered nematic monodomain (at $\approx 8,500,000$ steps on Fig 5.27).

The run was continued at this temperature for another 500,000 steps, over which ob-
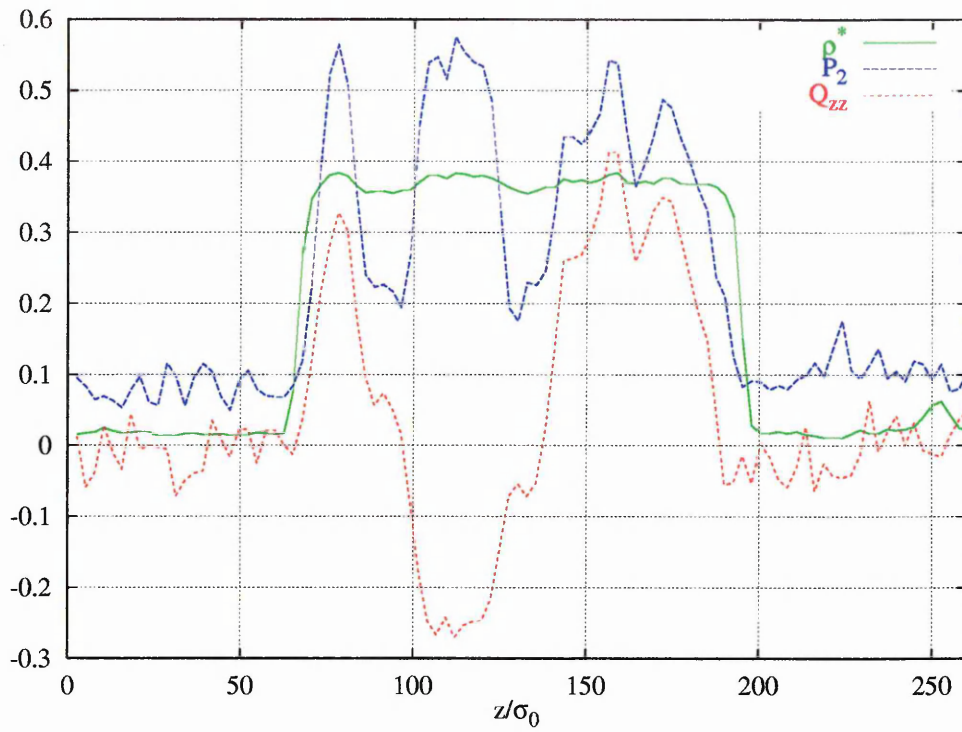
Figure 5.31: Order parameter profile - start of quenched run
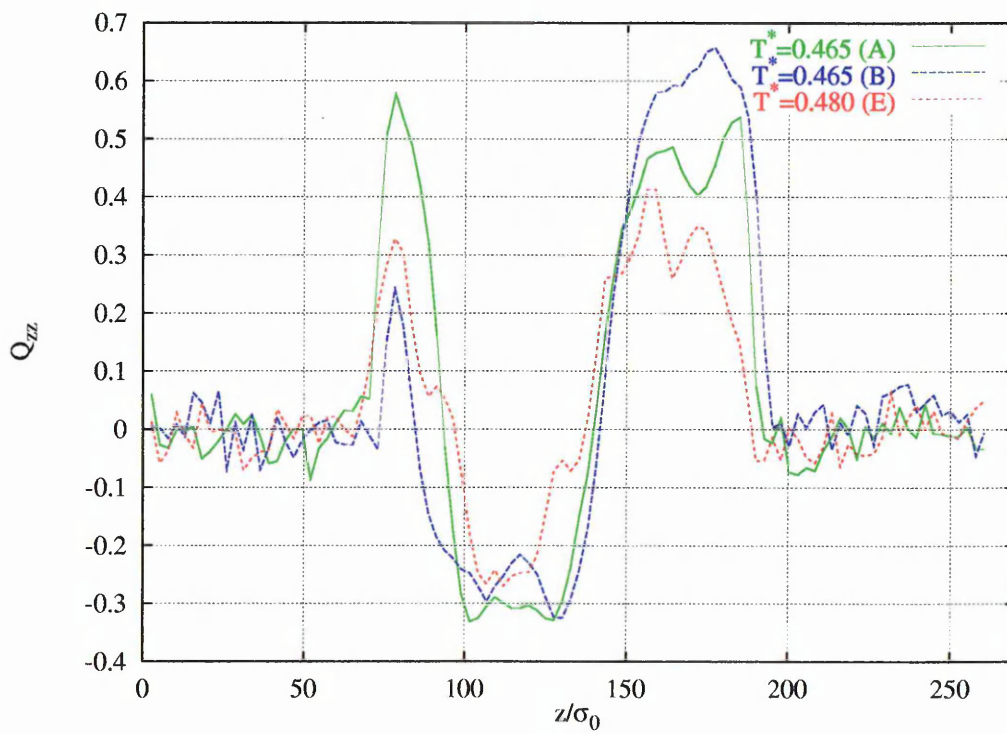

Figure 5.32: $Q_{zz}(z)$ behaviour at $T^* = 0.465$, compared with that at final $T^* = 0.480$
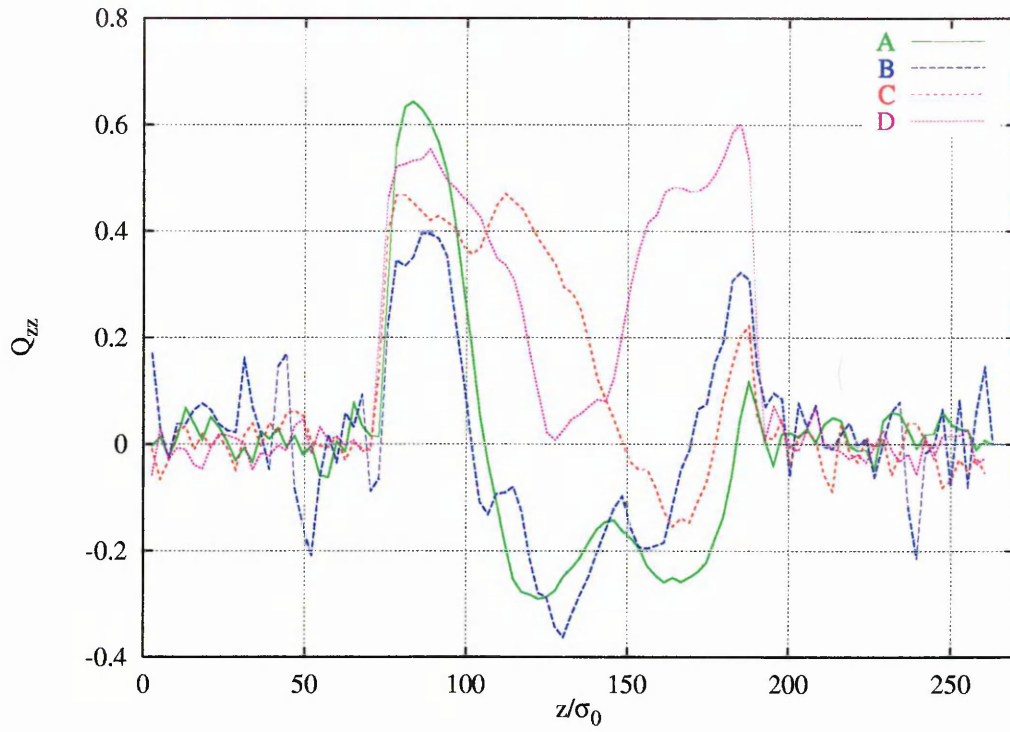
Figure 5.33: $Q_{zz}(z)$ behaviour at $T^* = 0.450$ (First part)
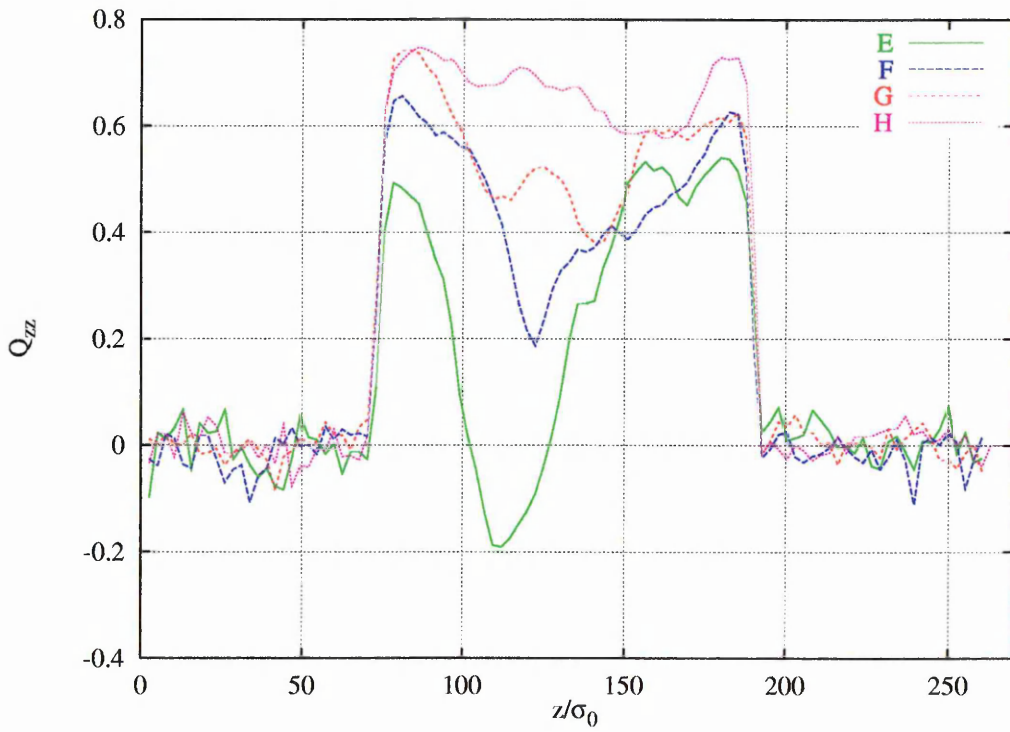
Figure 5.34: $Q_{zz}(z)$ behaviour at $T^* = 0.450$ (Second part)

164

servables were averaged and orientational correlation functions calculated. A series of relatively short heating runs were then commenced, in an attempt to achieve more accurate values (ie using equilibrated data) for the observables of interest. Typically these consisted of equilibration runs of approximately 1,000,000 steps, followed by production runs of 500,000 steps. As can be seen from the time evolutions of the potential energy (Fig 5.35) and nematic order parameter (Fig 5.36) during the heating run, these observables were reasonably stable after the equilibration time allowed.

5.4.1   Orientational Correlations

During the production periods, correlation functions were calculated in an identical manner to that for the medium sized system. These were the second rank order pair correlation function, $g_2(r)$ (Eqn 5.6), calculated for the bulk of the film and also in slices at regular z values, giving $g_2(r, z)$. Also measured were the correlations between slice directors, $D_2(d_z)$ (5.7), and $g_2(r)$ resolved in the *planar* and *normal* directions, $g_2^{xy}(d)$ and $g_2^{z}(d)$. These are presented for all the temperatures in the heating run, except for $g_2(r, z)$, which is only presented for the highest and lowest temperatures, $T^* = 0.480, 0.450$. In all cases where functions required splitting of the system into slices, the slice width was set to be the same as that in the medium film analysis, to enable meaningful comparison.

The behaviour of $g_2(r)$ (Fig 5.37) demonstrates quite clearly that the film is orientationally ordered at all of the temperatures studied, $g_2(r)$ decaying to a significant non-zero value for even the highest temperature, $T^* = 0.480$. Comparison with the medium system results shows that approximately the same limiting value, 0.38, is
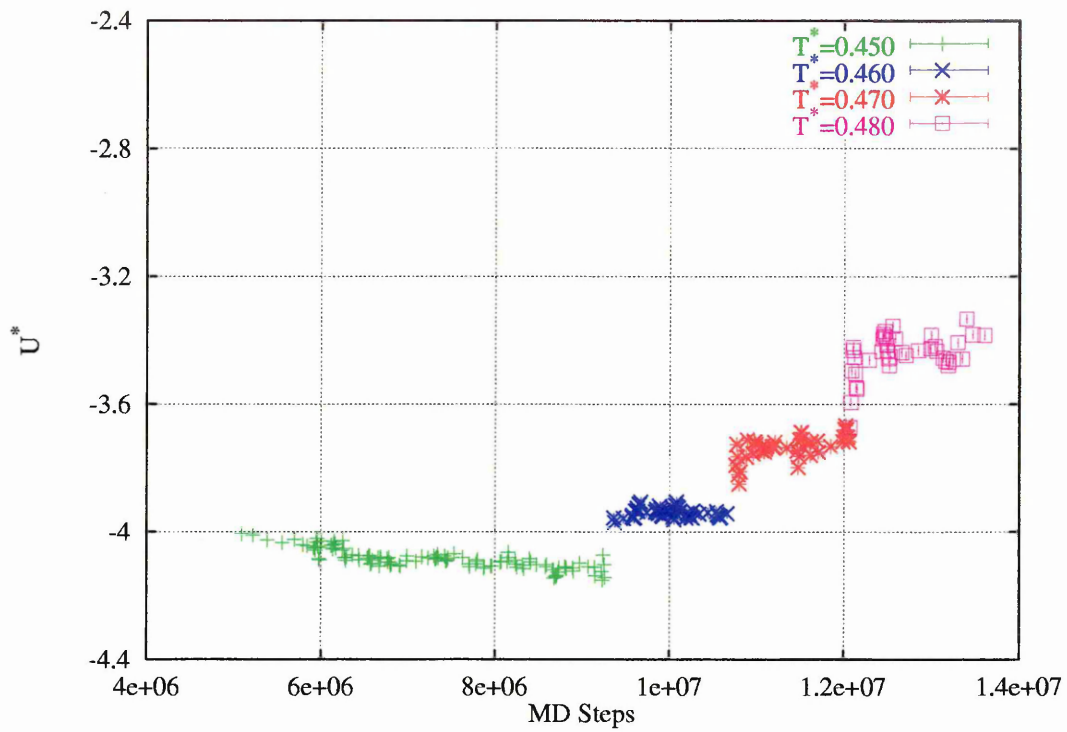
Figure 5.35: Potential energy evolution during heating run
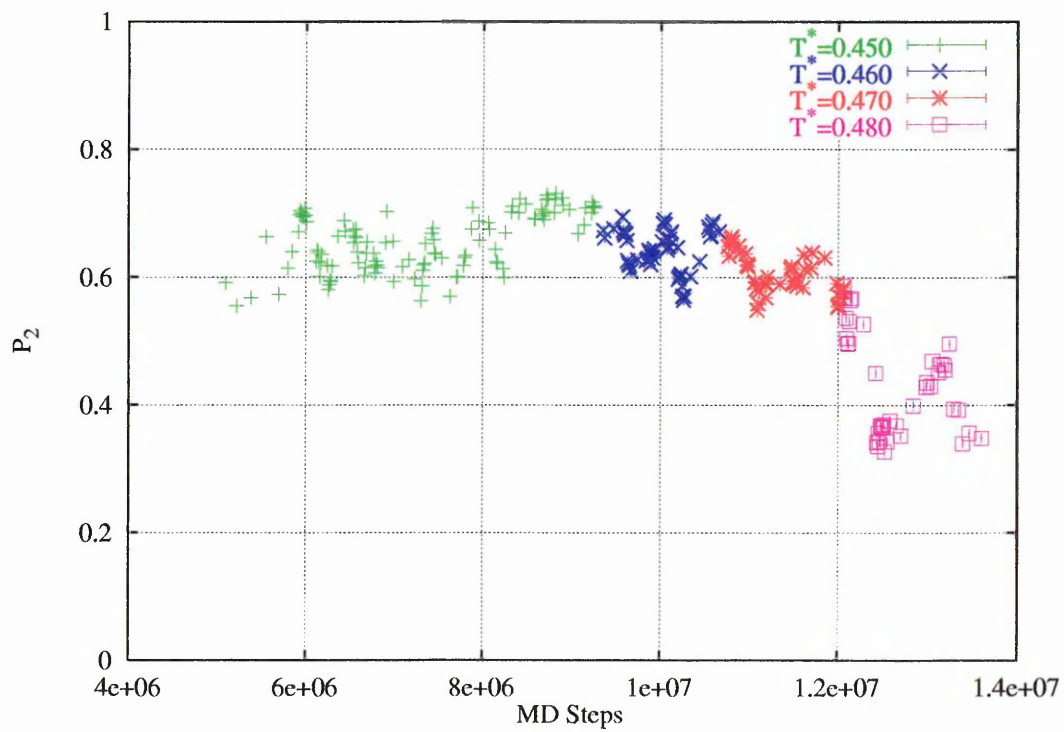
Figure 5.36: Nematic order parameter evolution during heating run

166
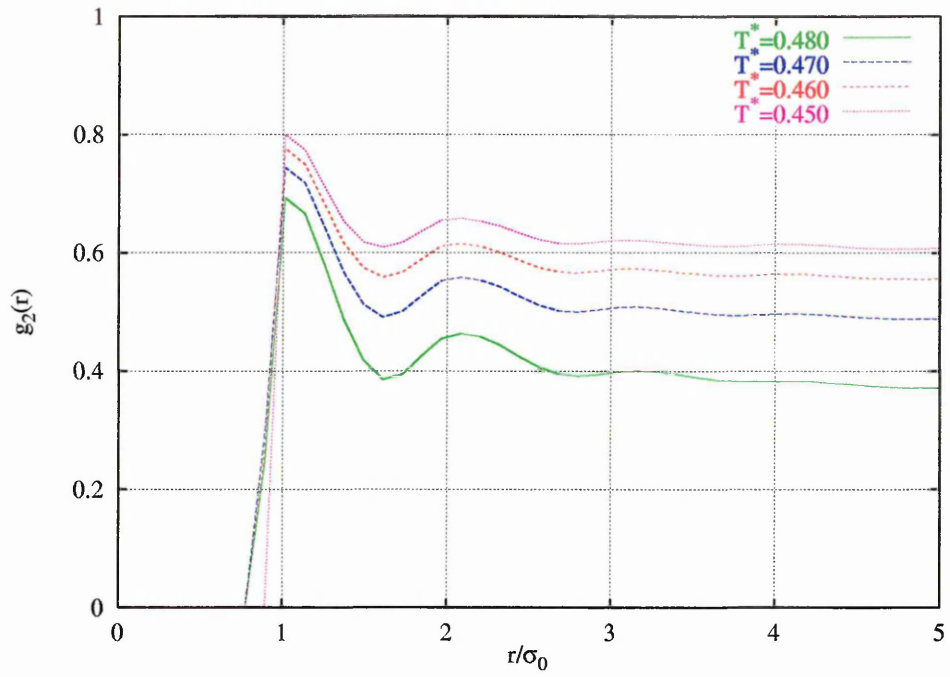
Figure 5.37: $g_2(r)$ at various temperatures
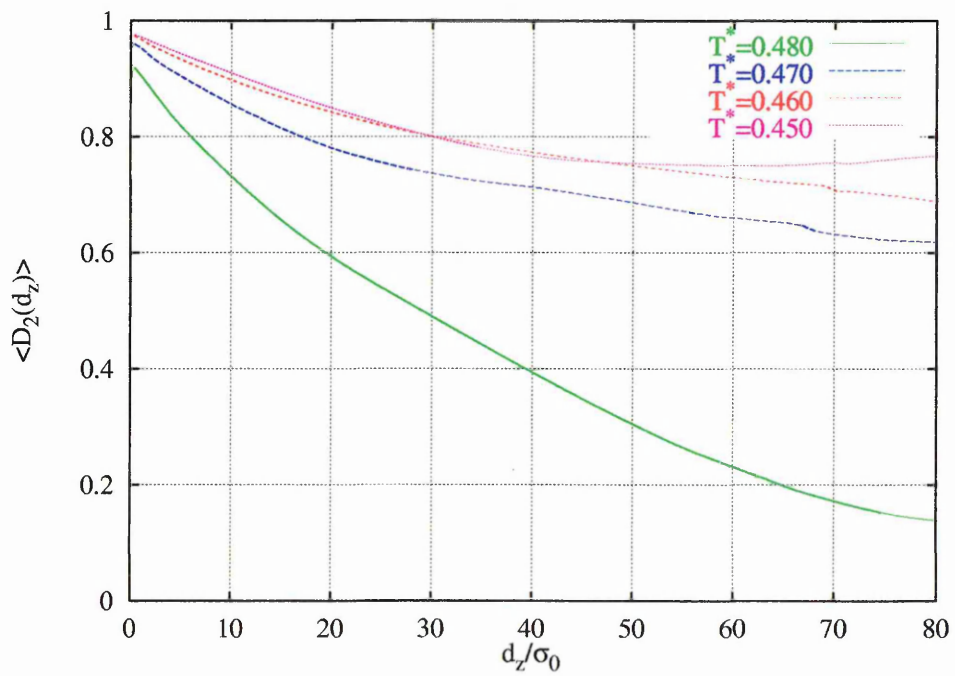
Figure 5.38: $\langle D_2(d_z) \rangle$ at various temperatures

167

observed for $T^* = 0.470$ instead, suggesting that the diminishing surface disordering effect in the larger system has resulted in a temperature shift of $T^* \approx 0.01$.

$D_2(d_z)$ tells a slightly different story (Fig 5.38), in that although nematic type ordering is indicated by the behaviour at the three lowest temperatures, at the highest, $T^* = 0.480$, a long ranged decay to a value typical of an isotropic phase is found. Since $D_2(d_z)$ measures the degree of *normal* orientational correlations, this tends to support the evidence of decoupling of *normal* and *parallel* orientational fluctuations observed in the medium system. However, the length scale of this decay can now be seen to extend to much larger distances, again significantly greater than that seen in bulk systems. Comparing this $T^* = 0.480$ curve with those obtained for the medium system (Fig 5.20) indicates the equivalent temperature in the latter to be somewhere between $T^* = 0.470$ and $T^* = 0.465$. This is in reasonable agreement with the temperature shift indicated by $g_2(r)$ data.

The behaviour of $g_2(r)$ resolved in the *planar* ($g_2^{xy}(d)$) and *normal* ($g_2^z(d)$) directions confirms the existence of nematic ordering in all three dimensions for the lowest three temperatures, with the long ranged decay in the *normal* correlations clearly demonstrated. Comparison of the $T^* = 0.480$ data with the medium system results, with $g_2^z(d)$ decaying to ≈ 0.31 by $d = 10\sigma_0$, again shows this degree of ordering to be equivalent to that displayed by the medium system for $0.470 > T^* > 0.465$.

3d plots of $\langle g_2(r, z) \rangle$ (Figs 5.40,5.41) again show nematic ordering in plane for both the highest and lowest temperatures studied, with the expected increase in the magnitude of this ordering as the temperature is decreased.
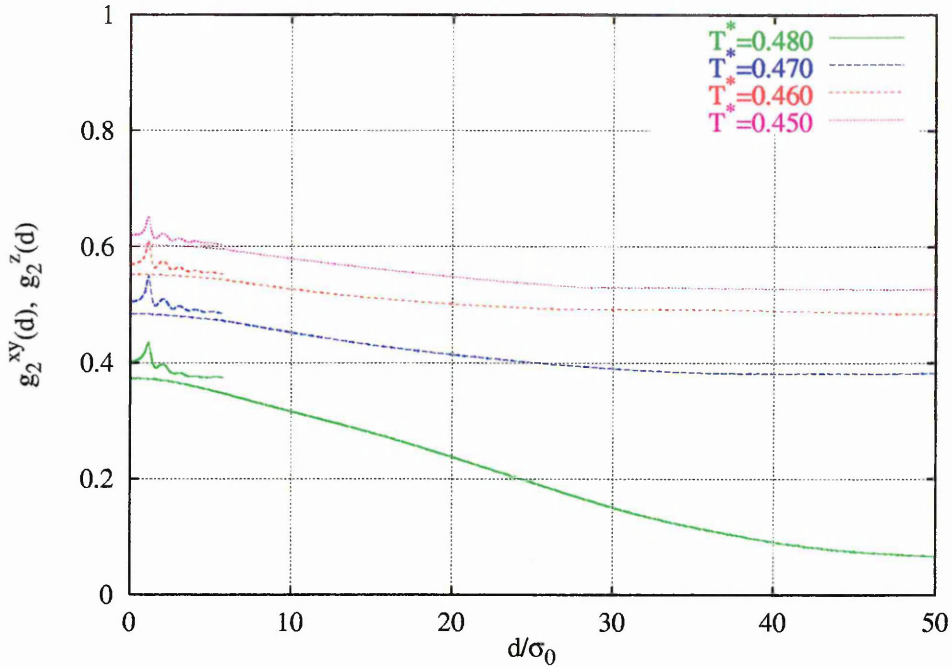
Figure 5.39: Resolved $g_2(r)$ at various temperatures (short lines are $g_2^{xy}(d)$, long ones $g_2^z(d)$)

Finally, a contour plot of $g_2(d_{xy}, d_z)$ is again presented, at the intermediate temperature of $T^* = 0.480$. The correlations can again be seen to decay quite quickly to a value around 0.4 by about $3\sigma_0$ in the *planar* (xy) direction, whereas decay in the *normal* (z) direction occurs to zero over a much longer distance, taking almost $50\sigma_0$. An important point is that the 0.3 contour does not curve round towards the xy axis like the 0.4 and higher ones, indicating that the decay has ceased in the xy direction at this point, whilst continuing in the z. This decay to zero of long range *normal* ordering is in agreement with previous results for the $D_2(d_z)$ and $g_2^z(d)$ data.
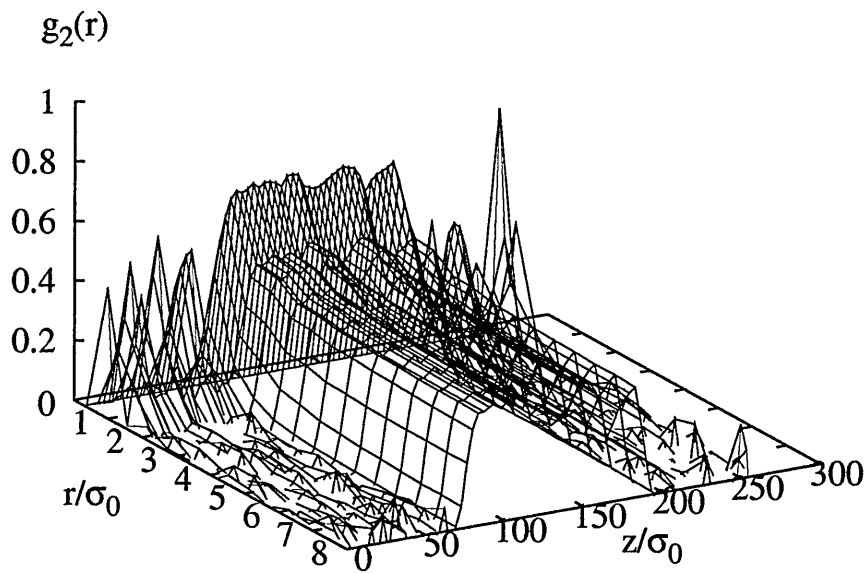
Figure 5.40: $g_2(r, z)$ for $T^* = 0.480$
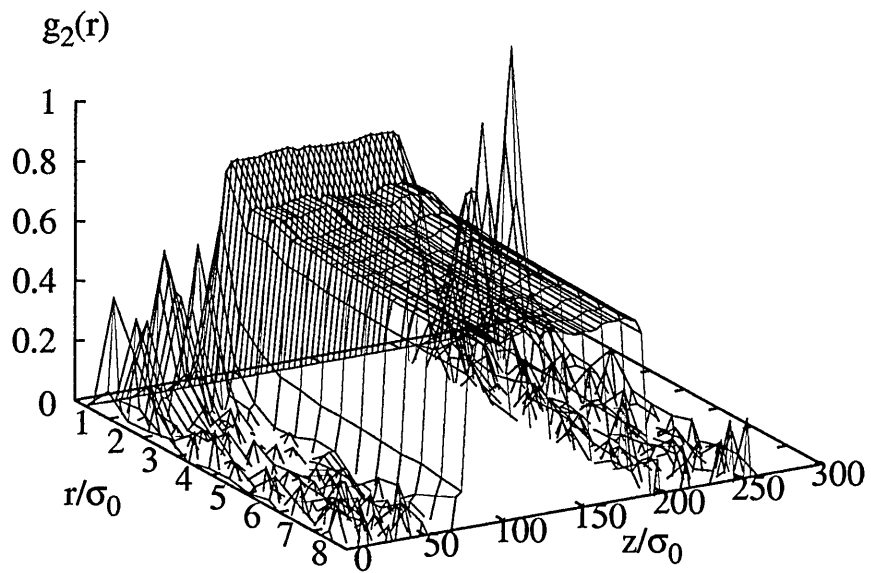
Figure 5.41: $g_2(r, z)$ for $T^* = 450$

170
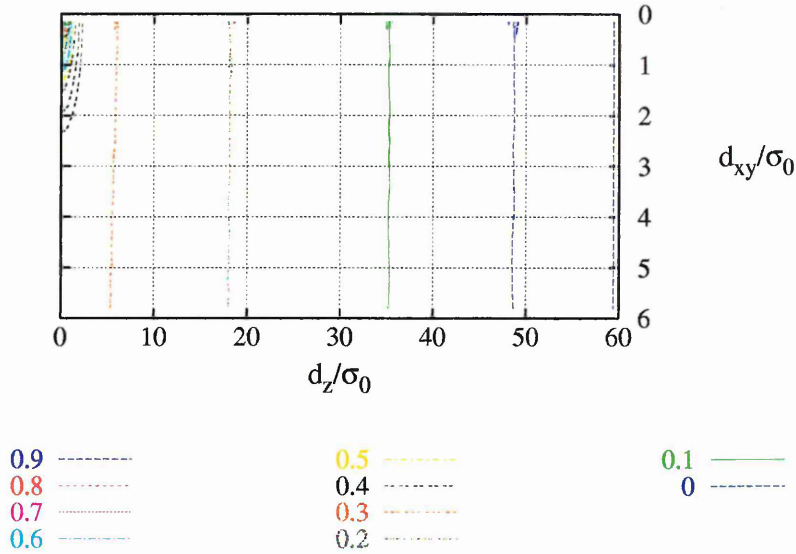
Figure 5.42: $g_2(d)$ contour plot - $T^* = 0.480$

5.4.2 Summary

The large system displayed qualitatively identical behaviour to both the small and medium systems, with a homeotropically anchored nematic monodomain again being observed at the lower temperatures. Difficulty was encountered in equilibrating this system, especially upon cooling, due to the orientational fluctuations occuring over particularly long timescales. However, reasonable analysis of these fluctuations was possible, and the heating run provided information about enough temperatures to make a fair comparison, both internally and with the medium system results. This comparison showed the fluctuations to display a similar behaviour to that presented in the previous section, except the larger width of the film made it possible to calculate them to larger distances and indeed showed a long ranged decay to be

171

occuring. The difference between the two types of behaviour is discussed in more detail in the next section.

5.5 System Size Dependency

The behaviour of the three different sized systems described above has been qualitatively almost identical, as would be expected since all that has been varied is the longest box edge length. However, notable quantitative differences have been observed, particularly in the onset temperature of nematic ordering and the behaviour of the orientational correlations.

The ordering temperatures for the various film thicknesses, L, are compared with each other and the Gibbs results from the previous chapter (which will be roughly equivalent to those for an infinite film) below (Tab 5.43). They are also plotted in graphical form against $1/L$ (Fig 5.44). For the film results, two temperatures are

Size	L/σ_0	$T_{NI}^*(xy)$	T_{NI}^*
Gibbs	∞	0.4825	0.4825
Large	~ 135	0.480	0.470
Medium	~ 34	0.475	0.450
Small	~ 11	0.470	0.450

Figure 5.43: Size dependency of transition temperatures

given. Firstly the highest temperature at which nematic fluctuations were observed to be stable across the cross-section of the box ie in plane, denoted $T_{NI}^*(xy)$. This was indicated by the temperature in the cooling runs at which P_2 showed a significant increase in both average value and error, indicating marked fluctuations to be

172

occuring, and was accompanied by notable peaks in the $P_2(z)$ profiles. Secondly the temperature at which a true nematic monodomain was established, T^*_{NI}, given by a levelling out of the *transverse* orientational correlations. For the small system, where these correlations were not measured, an estimate of this temperature was made by looking for a change in the gradient of the potential energy per particle, U^*, and nematic order parameter, P_2. For the Gibbs system these two were assumed to be equivalent. The results in Chapter 4 showed the isotropic-nematic transition to occur between $T^* = 0.485$ and 0.480 for this system. Here the average of these two, $T^* = 0.4825$, is used for comparison purposes.
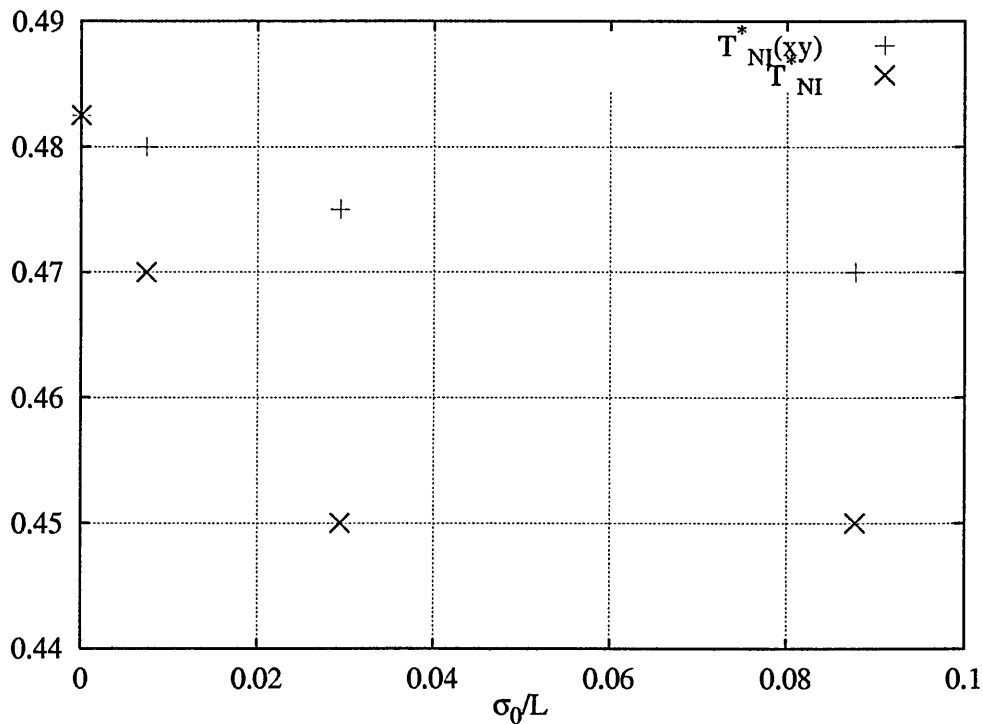

Figure 5.44: Dependency of transition temperatures upon system size

As expected, both transition temperatures are shifted down with decreasing system size, since the relative effect of the disordering interfaces increases. The temperature at which *planar* ordering occurs is always higher than that at which *perpendicular*

comes in, but still decreases quite notably, indicating that the interfaces have a marked effect on this, even though they do not break the *planar* symmetry. This is possibly due to the interfaces enabling larger density fluctuations within the film which disrupt the *planar* ordering process. The temperature at which monodomain formation occurs, ie *perpendicular* ordering becomes truly nematic, is much more sensitive to interfacial disordering, as would be expected, and appears to plateau out at around $T^* = 0.450$ for systems smaller than $L \sim 30\sigma_0$. We propose that this observation results from the competition between the relative effect of the disordering surfaces increasing with decreasing width, leading to a decrease in the monodomain transition temperature, and the fact that a smaller film width means that the range of the perpendicular orientational correlations does not have to be as great to cover the width of the film, as required for monodomain formation, and thus occurs at a higher temperature. Interestingly this suggests that the temperature range over which orientational domains are observed has a maximum value at a certain film width, which is somewhere in the vicinity of $L \sim 30\sigma_0$ according to this, admittedly very approximate, set of results.

An attempt to quantify the perpendicular orientational correlations has been made by empirically fitting an appropriate functional form to the $g_2^z(d)$ function. The best results were obtained using a tanh like function, similar to that for the density profiles used earlier. This form was chosen because the $g_2^z(d)$ functions were frequently observed to start off with a slow rate of decay, which increased as the function fell rapidly and then went through a point of inflexion before slowing as another plateau value was reached at large distances. The exact form used was

174

$$g_2^z(d) = \frac{1}{2}\left(g_2^z(0) + g_2^z(\infty)\right) + \frac{1}{2}\left(g_2^z(0) + g_2^z(\infty)\right) tanh\left[(d - d_i)/2\delta\right] \qquad (5.8)$$

where $g_2^z(0)$ and $g_2^z(\infty)$ are the limiting values for the function at $d = 0$ and $d = \infty$, d_i is the position of the point of decay inflexion, and δ the range over which decay occurs. All four values were obtained using a least squares fit to the graphs previously obtained (Figs 5.22,5.39). The fits are shown below (Figs 5.45,5.46), together with a table of the values obtained for the variables defined in the equation above (Tab 5.5)

Considering the large system first, where the fits appear to be the most accurate, it is encouraging to note that upon decreasing the temperature the decay becomes more short ranged, as indicated by δ, due to the increase in perpendicular orientational correlations. The temperature at which the orientational correlations extend the furthest without the formation of a monodomain is quite clearly at $T^* = 0.480$, with a long ranged decay being observed to a low value indicative of an isotropic phase. Whether this decay would go all the way to zero, or to a limiting finite value is impossible to say, although the fitting reports $g_2^z(\infty)$ as 0.020, indicating that over large enough distances the correlations essentially disappear. At higher temperatures this decay would presumably become shorter ranged, as seen in the medium system at $T^* = 0.475$ (which relatively speaking is further from the monodomain transition temperature), until eventually short decay lengths typical of a bulk isotropic are seen.

Unfortunately, the other fitting parameters obtained for the medium system do
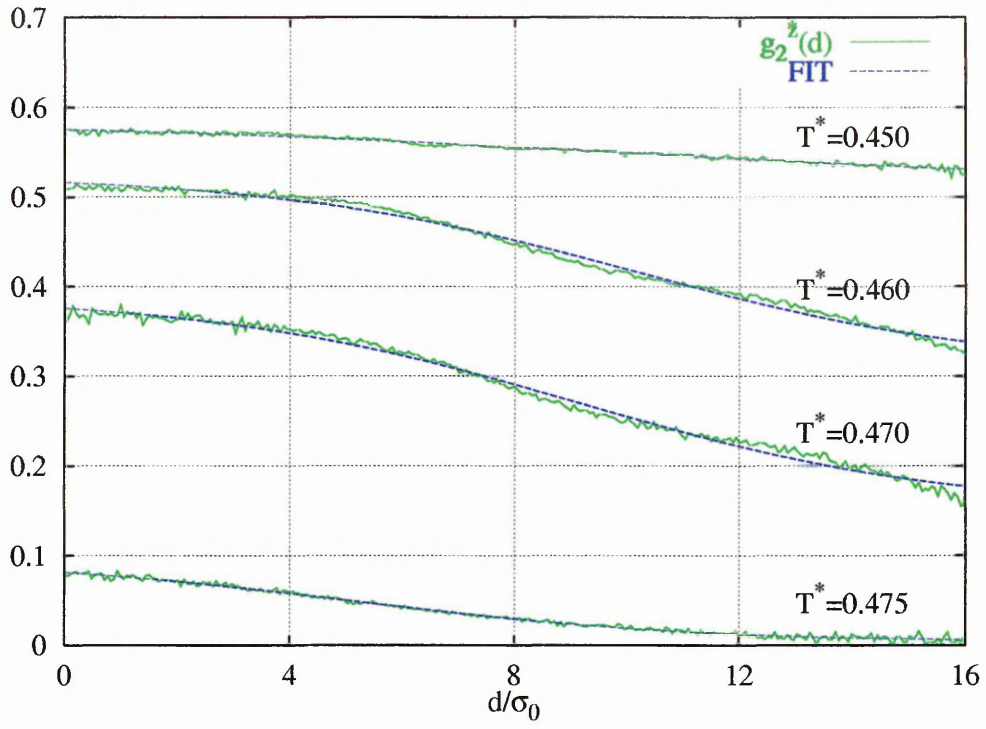
Figure 5.45: $g_2^z(d)$ and fittings for medium system
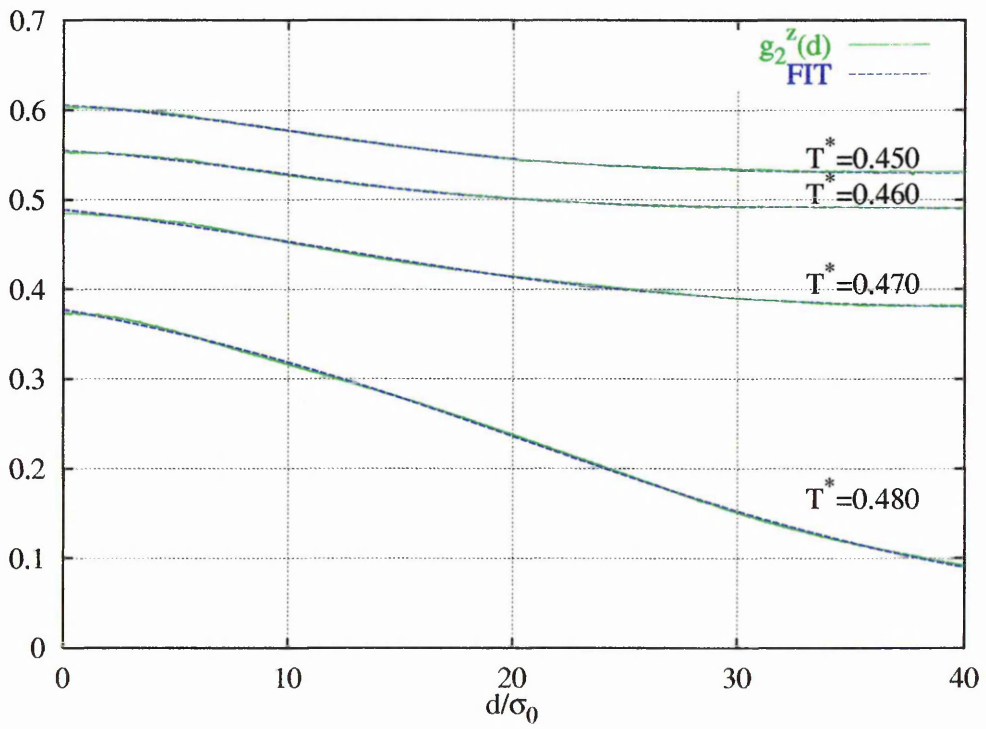
Figure 5.46: $g_2^z(d)$ and fittings for large system

176

Sys Size	T^*	$\frac{T^*}{T^*_{NI}}$	$g_2^z(0)$	$g_2^z(\infty)$	d_i	δ
Medium	0.450	1.00	0.586	0.512	10.1	5.56
Medium	0.460	1.02	0.525	0.306	10.2	3.28
Medium	0.470	1.04	0.391	0.149	9.16	3.36
Medium	0.475	1.06	0.096	0.003	5.04	3.08
Large	0.450	0.96	0.620	0.529	10.7	6.28
Large	0.460	0.98	0.565	0.490	10.0	5.45
Large	0.470	1.00	0.518	0.376	11.4	8.46
Large	0.480	1.02	0.442	0.020	20.62	12.0

not conform to this trend of a maximum range for the decay being seen in the middle of the temperature range. Although initially the decay range does increase for $T^* = 0.470, 0.460$, it does not decrease again at $T^* = 0.450$, where a nematic monodomain is formed, as shown by the $D_2(d_z)$ data. It is suspected that this is because the range of d covered by the function is not large enough, and if it were extended further it would show a levelling out to a relatively high value, indicative of a nematic. This is further supported by the fact that the decision to use a *tanh* fitting was based upon the form of the large system functions, which show two plateau areas, and that it clearly does not work as well for the medium system functions, where the function does not extend to a far enough range to show the second plateau.

Attempts were made to find a functional form which fitted the $D_2(d_z)$ data, using an exponential decay. However this proved to be unable to consistently characterise changes in the correlation length, and fitting was abandoned.

5.6 Conclusions

These simulations have clearly demonstrated the ability of a novel parameterisation of the GB to show both isotropic and nematic vapour coexistence, in good quantitative agreement with both the densities and temperatures shown by the Gibbs ensemble results in the previous chapter. In these direct simulations though, the presence of two free surfaces has considerably modified the ordering regime, and it is to this that attention has primarily been paid.

Three sets of simulations of varying box length were carried out, in an attempt to analyse the effect of film thickness upon the observed behaviour. The initial work on the smallest system was really just a preliminary study conducted to gain an indication of the sort of behaviour obtainable. Pleasingly it displayed homeotropic (normal) anchoring in the nematic phase at the free interface. Since the interfaces were the only symmetry breaking aspect of this system, the alignment was considered to have been induced by them. The tendency for homeotropic anchoring was explained in terms of the relative energies for various cleavage planes of the close-packed structures. A decrease in the ordering temperature was also observed, which suggested that the interfaces were disordering ie the system showed isotropic wetting.

This was confirmed by the study of the medium system, which was wide enough to enable observation of orientational order developing in the centre of the film and growing out to the edges. At intermediate temperatures, before stable nematic ordering had reached the interfaces, orientational fluctuations were observed across

the width of the film, which lessened with further decreasing of the temperature until finally nematic ordering was seen at the surfaces, and a monodomain observed. After extensive analysis, using a variety of functions to quantify these fluctuations, it was concluded a decoupling of *normal* and *transverse* orientational correlations led to this effect.

Simulations of a larger system produced qualitatively identical results, although it should be mentioned that significant problems in equilibrating the cooling run were encountered, and some rapid quenching of the system was required to form the expected nematic monodomain. This meant that any analysis of the cooling regime would be suspect, and so it was decided to use a heating run, starting from this nematic monodomain, to provide comparison with the medium system results, (although this of course raises the possibility of hysteresis affecting the results). Again decoupling between the normal and transverse ordering was observed, and a system size analysis attempted to quantify this effect.

This showed the temperature range associated with this decoupling to vary non-monatonically with film thickness, due to the competition between the relative strength of the disordering interfaces and the maximum correlation width needed to form a monodomain, which, respectively, tend to diminish and enlarge this range with increasing width of the film. Empirical fits to the $g_2^z(d)$ data have given some insight into the nature of the *normal* orientational correlations, but the functional form used did not appear appropriate for all of the data considered. For the largest system studied, however, the *normal* orientational correlation length certainly appeared to grow with increasing temperature, whilst the range of *transverse* correla-

tions remained qualitatively unchanged.

Although this decoupling could, to some extent, be due to the small cross-sectional area of the film, meaning greater periodicity and possibly enhanced orientational ordering, it is thought that the degree of decoupling observed here is too great for this to be the main process at work. Instead it is proposed that it is the symmetry breaking aspect of the interfaces which inhibits correlations from growing within the film. Although this mainly happens in the *normal* direction, the interfaces do have some effect, possibly through density fluctuations, upon the *transverse* ordering.

Previous simulation studies have shown various interfacial behaviours to be possible with the GB model; parallel alignment was obtained using $\kappa = 3.0$, $\kappa' = 1.0$ [105], whilst an earlier study [104] of the liquid-vapour interface using the standard GB parameterisation ($\kappa = 3.0$, $\kappa' = 5.0$) hinted at perpendicular alignment at the free interface, without showing nematic-vapour coexistence. These alignments can, again, be accounted for using simple cleavage plane arguments for the closed packed crystal structures.

The wetting behaviour is also affected by the parameterisation used, showing perhaps a greater dependency upon the shape anisotropy, κ, than the well-depth ratio, κ'. Whereas isotropic wetting has been observed here with $\kappa = 2.0$, the parallel alignment simulations saw nematic wetting with more elongated particles, $\kappa = 3.0$. This is consistent with theoretical predictions [44] showing a crossover from isotropic to nematic wetting with increase in anisotropy and experimental observations of the cyanobiphenyls, which show an increase in nematic wetting ability with increasing molecular length.

Also, the influence of μ and ν on the interaction well-depths and, subsequently, the phase behaviour cannot be ignored. Unfortunately, systematic characterisation of the effects of μ and ν on the behaviour at the free interface is more difficult than would be first thought, since nematic-vapour coexistence is only observed for a very restricted range of GB parameterisations. A primary cause of this appears to be the relative depth of the side-side interaction: if this is made too deep (eg. due to high shape anisotropy, or inappropriate choice of the exponents μ and ν) the isotropic-nematic-smectic triple point temperature goes above that of the liquid crystal-isotropic-vapour triple point and the only liquid crystal-vapour coexistence possible is with the smectic phase. However, fine-tuning of the parameters, subject to careful control of this well-depth, should enable further nematic-vapour coexistence regions to be located and thus clarify the effects of the various parameters upon the surface phase behaviour.

Experimental systems (see Chapter 2) also show all possible types of alignment, with the technologically applicable cyanobiphenyls displaying homeotropic anchoring [25], and the historically important compound, PAA, planar [23]. MBBA shows even more complex behaviour, undergoing a transition from homeotropic to oblique anchoring at a temperature slightly below the triple point [24]. The majority of experimental free surfaces display nematic wetting. However, some inference of isotropic wetting can be made from the surface tension behaviour of p-anisaldazine and MBBA.

Clearly, a wide range of behaviour can be seen in these types of experimental systems, and theoretical predictions have proven to be able to capture this behaviour

given a judicious choice of model system and method of solution. With sufficient simulation time, all these sorts of behaviour could be probably be seen. However, the challenge is to link the molecular details of the model in question to the behaviour displayed, and thus eventually aid in some way the design of these molecules and the applications they are to be used in.

It is proposed that the work presented in this chapter has contributed to this, in that it has added to the understanding of the GB model and shown an interesting region of phase space which is worthy of further investigation. The direct technological relevance of the work is probably not so obvious, but this simulation of a free surface serves as essentially a reference to the wall-substrate systems so important in display devices. The orientational correlation analysis presented has also been particularly thorough, and should be useful to gain some idea of the time and length scales associated with simulations of switching of orientational domains, again an important consideration in display technology.

How this work relates to the two-component mixture study presented previously, and considerations of future work, are presented next in the final chapter.

Chapter 6

Conclusions and Future Work

In this chapter, the principal results of this thesis are summarised, and suggestions for future work are made.

The main aim of this work, as specified in the introduction, was to use computer simulations of the GB model, to achieve greater understanding of the effects of polydispersity and interfacial symmetry breaking upon liquid crystal phase behaviour. These two effects are of significant technological importance because of their relevance to liquid crystal displays. However, the validity of this work from a purely scientific aspect will be considered as well as the question of applicability.

Since the work was composed of two quite different sets of simulations, each is summarised and suggestions made for future work separately. Conclusions from the two lines of work, and how they relate to each other, are then presented and the possibility of incorporating both types of simulation into future studies considered.

6.1 Bulk Coexistence

In this chapter the phase coexistence behaviour of a relatively short, strongly attracting GB particle, both in a pure system and in a mixture with a similar, slightly longer particle, was studied and shown to display a number of interesting properties.

The one component system studied in Chapter 4 showed the expected isotropic liquid-vapour coexistence, the existence of which was explained due to the competing effects of the relative well-depths. These results compared well with previous studies of GB isotropic-vapour coexistence, showing similar coexistence densities and the same ease of application of the Gibbs ensemble. The further discovery of nematic-vapour coexistence, albeit only in a narrow temperature range where equilibrium could be definitely achieved, was an exciting result, and was exploited further in the thin film work.

Parameterisation of the two component system was achieved without excessive computation, and could easily be applied to other generalised GB pairs. Simulation of this system proved to be rather difficult, as had been expected from previous work in the literature, indicating the Gibbs ensemble to have particular problems at high densities. However, reasonably satisfactory indications of equilibrium were achieved. This is attributed to the relative small degree of shape anisotropy of the particles used making insertion of the smaller particles a tractable operation. The resulting phase diagram shows significant deviation from that expected for the infinite system, but arguments have been presented explaining this in terms of finite size effects.

In terms of future work, a more in depth analysis of this finite size effect would

be the first obvious step. This could be done by simulating different system sizes, however, systems significantly larger than the one studied here would be beyond the bounds of computational practicability with present computers. An alternative method of analysing this effect would be to use the same system size but simulate a large number of different initial concentrations, such that the area of the coexistence envelope explored by each would be overlapped, to a reasonable extent, by those of neighbouring runs. This would give a complicated series of finite size curves, which, due to the Lever rule, would be shifted by different amounts due to the different starting concentrations of each one. Through a complicated numerical analysis it might be possible to then extrapolate to the thermodynamic limit, although the inherent error in these studies would make this a considerable task.

Less daunting would be the simulation of different GB mixtures, by varying the parameterisation of either one or both the components used here. Care would, however, need to be taken to ensure that particle insertion could still be achieved, and that the area of the phase diagram targeted was not too close to a smectic phase.

In conclusion, an intriguing parameterisation for the GB has been studied, which has shown a rich phase behaviour and is worthy of further investigation. An important application of the Gibbs ensemble to liquid crystal phenomena has also been made, which will pave the way for future such studies using judiciously chosen GB mixtures.

6.2 Thin Film System

This work was again based upon the results of the one-component bulk coexistence observed with the Gibbs ensemble, only in this case the system was perturbed not by the addition of another particle type, but rather the reproduction of this coexistence within one simulation box. The establishment of an interfacial region and its effect upon the system were the principal areas of interest.

Firstly, the interfaces were observed to have a disordering effect, with orientational ordering starting in the centre of the film and then slowly growing out to the interfaces as the temperature was lowered. This was accompanied by a shift in the transition to lower temperatures, due to this surface disordering, the relative effect of which increased with decreasing film width, leading to a larger shift in temperature.

Once ordering had reached the interfaces, normal alignment or homeotropic anchoring was seen at the free surface. This alignment can be readily explained in terms of the relative energies for various cleavage planes of the close-packed structures.

At the intermediate temperatures between transverse nematic ordering developing in the centre of the film and the formation of a nematic monodomain, orientational fluctuations were observed to occur across the width of film, with differently orientated nematic domains forming and propagating through the film, before, generally, dispersing at the edges. As the temperature was lowered, the lifetime and size of these domains increased, along with the orientational correlations between them.

These fluctuations have been extensively analysed for the medium and large systems, using a variety of different correlation functions. In both systems, a marked

decoupling of the *normal* and *transverse* correlations was observed, nematic ordering being established in the *transverse* direction first and a long range decay in correlations, quite unlike that seen in bulk systems, occuring in the *normal* direction. Only at much lower temperatures did the *normal* ordering match up with the *transverse*, at which point a nematic monodomain was established.

A system size analysis showed a definite increase in the range of decay of orientational correlations with increasing system size, although this was expected since the correlations are bounded by the width of the film. The decreasing size of the temperature range over which the orientational fluctuations occurred was also predictable, since as the system becomes more bulk-like the nature of the *normal* and *transverse* correlations must converge.

Further elucidation of the decoupling effect could be achieved using a much more comprehensive system size study. This would need to incorporate different cross-sectional areas and lengths of film, as well as comparisons with bulk one phase simulations in anisotropic boxes, to distinguish between the degree of decoupling due simply to periodicity and that from the interfaces. Attempts to see this effect experimentally could also be made, using some form of structural spectroscopy (eg. XRD) and Fourier analysis to resolve the data into the appropriate component directions.

In conclusion, an important example of GB behaviour at a free surface has been presented, the first to show homeotropic ordering at the nematic-vapour interface. Essentially, studies of the free surfaces of liquid crystals, as well as being of scientific validity in their own right, can be regarded as reference systems for the more techno-

logically important liquid crystal substrate interface. It has been demonstrated here that even using a relatively simple mesogenic model, some of the important physics of liquid crystals at interfaces can be captured, and thus this potential should continue to have a role in modelling this behaviour.

6.3 Conclusions

When considering this thesis as a whole, it is particularly encouraging to note the degree of internal consistency in a number of the values reported. Firstly, the isotropic-nematic transition temperature seen in the Gibbs results is in excellent agreement with those reported in the film simulations, which are themselves consistent with the expected system size trend. In the bidisperse simulations, the transition temperatures of the pure systems give an excellent estimate of the transition temperature for the mixed system, if a linear trend across the concentration diagram is assumed. The preliminary one-box mixture simulations also quite nicely tie in with the Gibbs results.

The simulations attempted here, both the two-component coexistence and the film simulations, have been relatively ambitious in the degree of complexity inherent in the system, and thus the run times required to ensure confidence in the results were difficult to achieve. However, it is felt that a sufficient degree of internal consistency between the observables has been shown for each of the systems such that, when coupled with the agreement between the different studies and with previous work, the results here can be regarded with credence.

When considering the question of future work, the two separate studies presented could be immediately extended by the consideration of larger systems, as is always the case in computer simulations. This would shed some light on the system size effects seen in the Gibbs simulations, and also enable the fluctuations seen in the film work to be more accurately quantified. Unfortunately this would take a considerable amount of computational power, and at present any meaningful simulation of larger systems, at least larger Gibbs simulations or wider films, are probably just out of reach.

However, it would be possible to investigate a film with a larger cross-sectional area and the same width as the medium system, using the same parallel code as for the large system. This should provide some information on the disordering strength of the interfaces and how the decoupling depends upon them and the periodicity of the system.

There also, of course, remains the possibility of modifying the models used here and seeing the effect this has upon the observed behaviour. Firstly, changing the degree of bi-dispersity in the Gibbs simulations, either by using a concentration ratio other than 50:50 or a different mixture of GB types, could yield interesting results. An increase in the degree of difference between the two particles has been theoretically predicted to result in a wider coexistence envelope, which it should be possible to see in a simulation study. Secondly, the use of different GB particle types in free interface systems could show a wide variety of both alignment and wetting behaviours, although care would have to be taken to tune the well depths so that stable nematic vapour coexistence could be simulated. The GB parameterisations

used here have corresponded to relatively short particles with a strong anisotropy in their well-depth functions, which, along with the strong exponents (μ, ν) have helped stabilise the liquid-crystal phases observed. Although this disparity between the shape and well-depth anisotropies could be regarded as slightly unrealistic, it has been important in enabling the Gibbs simulations, upon which the film study was based, to be carried out.

This work has successfully shown how a relatively simple liquid crystal model can exhibit a variety of complex and interesting behaviour, all of it in some way relevant to device applications in liquid crystal displays. The next step is the incorporation these two perturbations of the pure system into a single study ie. interfacial mixtures. The computational simplicity of the GB model and its generalised form mean that a relatively large system could eventually be simulated, in what would amount to a markedly more realistic simulation of a display device. The use of parallel processing, as in the large film system here, would be important in allowing much larger time and length-scales to be accessed, and the parallel GB codes already in the public domain would be easily convertible to a generalised form.

Obviously though, the first step would have to be a series of simulations of relatively small two-component interfacial systems, with the aim of getting an idea of the sorts of phase behaviour to be expected with such systems. There is a strong argument for starting these with free surfaces, in order to avoid the extra complexity of a wall-particle interaction. The effect of preferential adsorption at the interfaces may well enable nematic wetting to be seen with homeotropic alignment, which has not been seen with single component GB systems.

Whatever new studies are conducted in this area, this work has provided a tentative reference for both the phase separation and free surface (interfacial) aspects of the Gay-Berne model and its generalised form. Probably the most encouraging point to be demonstrated by this work is that these systems, even though they can seem highly idealised and are based upon a simple potential, are capable of showing a wide variety of fascinating phenomena. However, the downside of this is that it can be easy to be too ambitious too soon by assuming a relatively simple model will be easy to simulate, whereas in fact the long time scales associated with liquid-crystalline phenomena can make successful equilibration difficult to achieve. A cautious, considered approach should, therefore, always be adopted.

Bibliography

[1] O.Z. Lehmann, *Physikal Chem.* 4, 462 (1889) L. Gattermann, A. Ritschke, *Ber. Deut. Chem. Ges.* 23, 1738 (1890).

[2] P.G. de Gennes, J. Prost, *The Physics of Liquid Crystals* (Clarendon, Oxford, 1993).

[3] S. Chandrasekhar, *Liquid Crystals* (Cambridge University Press, 1992).

[4] P.J. Collings, M. Hird, *Introduction to Liquid Crystals* (Taylor and Francis, 1997).

[5] M.P. Allen, D.J. Tildesley, *Computer Simulation of Liquids* (Clarendon, Oxford, 1987).

[6] D. Frenkel, B. Smit, *Understanding Molecular Simulation* (Addison-Wesley, 1996).

[7] J.G. Gay, B.J. Berne, *J. Chem. Phys.* 74, 3316 (1981).

[8] H.N.W. Lekkerkerker *et al*, *J. Chem. Phys.* 80,7,3427 (1984).

[9] P.J. Camp, M.P. Allen, P.G. Bolhuis, D. Frenkel, *J. Chem. Phys.* 106, 9270 (1997).

[10] S. Chandrasekhar *et al*, *Pramana* **9**, 47 (1977) For review see Hinov HP, *Mol. Cryst. Liq. Cryst.* **136**, 221 (1986).

[11] K. Ema *et al*, *Phys. Rev. Lett.* **73**, 565 (1994).

[12] C. Casagrande *et al*, *J. de Phys. Lett.* **43**, L-671 (1982).

[13] R. Pratibha, N.V. Madhusudana , *Mol. Cryst. Liq. Cryst. Lett.* **1**, 111 (1985).

[14] G.R. Luckhurst, *Quart Rev* **22**, 179 (1968), *Mol. Cryst. Liq. Cryst.* **21**, 125 (1973).

[15] K. Ema *et al*, *Phys. Rev. A* **39**, 2599 (1988).

[16] J.S. Foster, J.E. Frommer, *Nature (London)* **333**, 542 (1988), J.K. Spong, H.A. Mizes, L.J. LaComb Jr, M.M. Dovek, J.E. Frommer, J.S. Foster, *ibid.* **338**, 137 (1989).

[17] M. Rivera Hernandez, M.J. Miles, *Scanning Microsc., submitted* (1996).

[18] M. Cagnon, G. Durand, *Phys. Rev. Lett.* **70**, 2742 (1990).

[19] D.J. Cleaver, D.J. Tildesley, *Mol. Phys.* **81**, 781 (1994); D.J.Cleaver, M.J. Callaway, T. Forester, W. Smith, D.J. Tildesley, *ibid.* **86**, 613 (1995).

[20] B. Jérôme, J. O'Brian, Y. Ouchi, C. Stanners, Y.R. Shen, *Phys. Rev. Lett.* **71**, 758 (1993); B. Jerome, Y.R. Shen, *Phys. Rev. E* **48**, 4556 (1993).

[21] B. Jérôme, *Rep. Prog. Phys.* **54**, 391 (1991).

[22] M.A. Bouchiat, D. Langevin-Cruchin, *Phys. Lett. A* **34**, 331 (1971).

[23] P. Chiarelli, S. Faetti, L. Fronzoni, *J. Phys. (Paris)* **44**, 1061 (1983).

[24] P. Chiarelli, S. Faetti, L. Fronzoni, *Phys. Lett.* **101A**, 31 (1984).

[25] H. Kasten, G. Strobl, *J. Chem. Phys.* **103**, 6768 (1995).

[26] J. Als-Nielsen, F. Christensen, P.S. Pershan PS, *Phys. Rev. Lett.* **48** 1107 (1982).

[27] V.A. Korjenevsky, M.G. Tomilin, *Liq. Cryst.* **15**, 5, 643 (1993).

[28] R. Lucht and Ch. Bahr, *Phys. Rev. Letts.* **78** 3487 (1997); **80** 3783 (1998); R. Lucht *et al*, *J. Chem. Phys.* **108** 3716 (1998).

[29] S. Faetti, V. Palleschi, *J. Chem. Phys.* **81**, 12 (1984)

[30] Y. Martinez-Raton, E. Velasco, A.M. Somoza, L. Mederos, T.J. Sluckin, *J. Chem. Phys.* **108**, 2583 (1998).

[31] S. Krishnaswamy, R. Shashidhar, *Mol. Cryst. Liq. Cryst.* **35**, 253 (1976).

[32] M.M. Telo da Gama, *Physica. A.* **244**, 389 (1997).

[33] A. Böttger, D. Frenkel, J.G.H. Joosten, G. Krooshof, *Phys. Rev. A.* **38**, 6316 (1988).

[34] L. Onsager, *Ann. N.Y. Acad. Sci.* **51**, 627 (1949).

[35] W. Maier, A. Saupe, *Z Naturf. (a)* **13**, 564 (1958).

[36] U. Fabbri, C. Zannoni, *Mol. Phys.* **58**, 763 (1986).

[37] Z.P. Zhang, O.G. Mouritsen, M.J. Zuckermann, *Phys. Rev. Lett.* **69**, 2803 (1992).

[38] T. Odijk, H.N.W. Lekkerkerker, *J. Phys. Chem.* **89**, 2090 (1985), G.J. Vroege, H.N.W. Lekkerkerker, *J. Phys. Chem.* **87**, 3601 (1993).

[39] P. Sheng, *Phys. Rev. A.* **26**, 1610 (1982).

[40] A. Poniewierski, T.J. Sluckin, *Liq. Cryst.* **2**, 281 (1987).

[41] M.M. Telo da Gama, P. Tarazona, *Phys. Rev. A.* **41**, 1149 (1990).

[42] M.M. Telo da Gama, *Mol. Phys.* **52**, 585 (1984); J.M. Thurtell, M.M. Telo da Gama, K.E. Gubbins, *Mol. Phys.* **54**, 321 (1984).

[43] B. Tjipto-Margo, A.K. Sen, L. Mederos, D.E. Sullivan, *Mol. Phys.* **67**, 601 (1989).

[44] E. Martin del Rio, M.M. Telo da Gama, E. de Miguel, L.F. Rull, *Phys. Rev. E.* **52**, 5028 (1995).

[45] M.M. Telo da Gama, in *Observation, Prediction and Simulation of Phase Transitions in Complex Fluids*, Vol 460 of *NATO Series C* ed. M. Baus, L.F. Rull, J.P. Ryckaert (Kluwer, Dordrecht, 1995), pp 243-292.

[46] B. Tjipto-Margo, D.E. Sullivan, *J. Chem. Phys.* **88**, 6620 (1988).

[47] G.R. Luckhurst, P.S.J. Simmonds, *Mol. Phys.* **80**, 233 (1993).

[48] J.D. Parsons, *Mol. Phys.* **42**, 951 (1980); P Harrowell, D.W. Oxtoby, *Mol. Phys.* **54**, 1325 (1985).

[49] B.J. Berne, P. Pechukas, *J. Chem. Phys.* **56**, 4213 (1972).

[50] E. Martin del Rio, M.M. Telo Da Gama, E. De Miguel, L.F. Rull, *Europhysics Lett.* **35**, 189 (1996).

[51] C. Croxton, *Introduction to Liquid State Physics* (Wiley, 1975).

[52] N. Metropolis, A.W. Rosenbluth, M.N. Rosenbluth, A.H. Teller, E. Teller, *J. Chem. Phys.* **21**, 1087 (1953).

[53] J.A. Barker, R.O. Watts, *Chem. Phys. Lett.* **3**, 144 (1969).

[54] B. Smit, in *Computer Simulation in Chemical Physics*, Vol 397 of *NATO Series C* ed. M.P. Allen, D.J. Tildesley (Kluwar, Dordrecht, 1993).

[55] J.M. Prausnitz *et al*, *Molecular Thermodynamics of Fluid-Phase Equilibria* (Prentice-Hall, Englewood Cliffs NJ, 1986).

[56] B. Widom, *J. Chem. Phys.* **39**, 2802 (1963).

[57] A.Z. Panagiotopoulos, *Mol. Phys.* **61**, 813 (1987).

[58] A.Z. Panagiotopoulos *et al*, *Mol. Phys.* **63**, 527 (1988).

[59] A.Z. Panagiotopoulos, *Int. J. Thermophys.* **10**, 447 (1989).

[60] H. Goldstein, *Classical Mechanics* (Addison-Wesley, 1980).

[61] S.L. Price, A.J. Stone and M. Alderton, *Mol. Phys.* **52**, 987 (1984).

[62] L. Verlet, *Phys. Rev.* **159**, 98 (1967).

[63] R.W. Hickney, *Methods Comput. Phys.* **9**, 136 (1970).

[64] K. Singer, A. Taylor and J.V.L. Singer, *Mol. Phys.* **33**, 1757 (1977).

[65] D. Fincham, *CCP5 Quarterly* **8**, 47 (1984).

[66] W.G. Hoover, A.J.C. Ladd and B. Moran, *Phys. Rev. Lett.* **48**, 1818 (1982).

[67] D. Brown and J.H.R. Clarke, *Mol. Phys.* **51**, 1243 (1984).

[68] D. Fincham, N. Quirke and D.J. Tildesley, *J. Chem. Phys.* **84**, 4535 (1986).

[69] J.A. Barker, R.A. Fisher, R.O. Watts, *Mol. Phys.* **21**, 657 (1971).

[70] P.A. Lebwohl, *Phys. Rev.* **6** 426 (1972), P.A. Lebwohl, *Phys. Rev. A.* **7**, 2222 (1973).

[71] D. Frenkel, R. Eppenga, *Phys. Rev. Lett.* **49**, 1089 (1982).

[72] D. Frenkel, B.M. Mulder, J.P. Mctague, *Phys. Rev. Lett.* **52**, 287 (1984), D. Frenkel, B.M. Mulder, *Mol. Phys.* **55**, 1171 (1985), D. Frenkel, *Mol. Phys.* **60**, 1 (1987).

[73] M.P. Allen, M.R. Wilson, *J. Comp. Aided Mol. Des.* **3**, 335 (1989).

[74] P.J. Camp, C.P. Mason, M.P. Allen, A.A. Khare, D.A. Kofke, *J. Chem. Phys.* **105**, 2836 (1996).

[75] A. Stroobants, H.N.W. Lekkerkerker, D. Frenkel, *Phys. Rev. Lett.* **57**, 1452 (1986).

[76] A. Stroobants, H.N.W. Lekkerkerker, D. Frenkel, *Phys. Rev. A.* **36**, 2929 (1987).

[77] D. Frenkel, *J. Phys. Chem.* **92**, 11,3280 (1988).

[78] J.A.C. Veerman, D. Frenkel, *Phys. Rev. A.* **41**, 6,3237 (1990).

[79] P. Bolhuis, D. Frenkel, *J. Chem. Phys.* **106**, 666 (1997).

[80] A. Stroobants, *Phys. Rev. Lett.* **69**, 16,2388 (1992).

[81] C. McBride, M.R. Wilson, J.A.K. Howard, *Mol. Phys.* **93**, 955 (1998).

[82] J. Corner, *Proc. Roy. Soc. Lond. A.* 275 (1948).

[83] T. Kihara, *Rev. Mod. Phys.* **25**, 831 (1953), S.H. Walmsley, *Chem. Phys. Lett.* **49**, 320 (1977).

[84] J. Kushick, B.J. Berne, *J. Chem. Phys.* **64**, 1362 (1976).

[85] A.J. Stone, in *The Molecular Physics of Liquid Crystals* ed. G.R. Luckhurst, G.W. Gray (Academic Press, 1979), Chap. 2.

[86] D.J. Adams, G.R. Luckhurst, R.W. Phippen , *Mol. Phys.* **61**, 1575 (1987).

[87] G.R. Luckhurst, R.A. Stephens, R.W. Phippen, *Liq. Cryst.* **8**, 451 (1990).

[88] E. de Miguel, L.F. Rull, M.K. Chalam, K.E. Gubbins, *Mol. Phys.* **71**, 1223 (1990).

[89] E. de Miguel, L.F. Rull, M.K. Chalam, K.E. Gubbins, *Mol. Phys.* **72**, 593 (1991).

[90] M.K. Chalam, K.E. Gubbins, E. de Miguel, L.F. Rull, *Mol. Sims.* **7**, 357 (1991).

[91] L.F. Rull, *Physica A.* **220**, 113 (1995).

[92] R. Berardi, A.P.J. Emerson, C. Zannoni, *J. Chem. Soc. Faraday Trans.* **89**, 4069 (1993).

[93] J.T. Brown, M.P. Allen, E. Martin del Rio, E. de Miguel, *Phys. Rev. E.* **57**, 6685 (1998).

[94] E. de Miguel, E. Martin del Rio, J.T. Brown, M.P. Allen, *J. Chem. Phys.* **105**, 1 (1996).

[95] R. Hashim, G.R. Luckhurst, S. Romano, *Liq. Cryst.* **1**, 133 (1986).

[96] R.L. Humphries, P.G. James, G.R. Luckhurst, *Symp. Faraday Soc.* **5**, 107.

[97] R. Lukac, F.J. Vesely, *Mol. Cryst. Liq. Cryst.* **262**, 533 (1995).

[98] D.J. Cleaver, C.M. Care, M.P. Allen, M.P. Neal, *Phys. Rev. E.* **54**, 1 (1996).

[99] R.A. Bemrose, C.M. Care, D.J. Cleaver, M.P. Neal, *Mol. Phys.* **90**, 625 (1997).

[100] C.D. Holcomb, P. Clancy, J.A. Zollweg, *Mol. Phys.* **78**, 437 (1993).

[101] J. Alejandre, D.J. Tildesley, G.A. Chapela, *Mol. Phys.* **85**, 651 (1995).

[102] G.R. Luckhurst, T.J. Sluckin, H.B. Zewdie, *Mol. Phys.* **59**, 657 (1986).

[103] D.J. Cleaver, M.P. Allen, *Mol. Phys.* **80**, 253 (1993).

[104] E. Martin del Rio, E. De Miguel, L.F. Rull, *Physica A.* **213**, 138 (1995).

[105] E. Martin del Rio, E. De Miguel, *Phys. Rev. E.* **55**, 2916 (1997).

[106] A.P.J. Emerson, S. Faetti, C. Zannoni, *Chem. Phys. Lett.* **271**, 241 (1997).

[107] M.A. Bates, C. Zannoni, *Chem. Phys. Lett.* **280**, 40 (1997).

[108] M.A. Bates, *Chem. Phys. Lett.* **288**, 209 (1998).

[109] Z. Zhang, A. Chakrabarti, O.G. Mouritsen, M.J. Zuckermann, *Phys. Rev. E.* **53** 2461 (1996).

[110] P.I.C. Teixeira and T.J. Sluckin, *J. Chem. Phys.* **97** 1498 (1992); *ibid* 1510.

[111] J. Stelzer, P. Galatola, G. Barbero, L. Longa, *Phys. Rev. E.* **55** 477 (1997).

[112] G.D. Wall, D.J. Cleaver, *Phys. Rev. E.* **56**, 4306 (1997).

[113] V. Palermo, F. Biscarini, C. Zannoni, *Phys. Rev. E.* **57**, 2519 (1998).

[114] T. Gruhn, M. Schoen, *Mol. Phys.* **93** 681 (1998).

[115] T. Miyazaki, K. Shigematsu, M. Yamashita, *J. Phys. Soc. Japan.* **67**, 85 (1998).

[116] B. Smit, D. Frenkel, *Mol Phys* **68**, 951 (1989).

[117] M.P. Allen, Simulation and Phase Diagrams, Ch 10, in *Monte Carlo and molecular dynamics of condensed matter systems*, ed. K. Binder, G. Ciccotti (Italian Physical Society, Bologna, 1996).

[118] R. Eppenga and D. Frenkel, *Mol. Phys.* **53**, 1303 (1984).

[119] A. Harasima, *Adv. Chem. Phys.* **1**, 203 (1958).

[120] J.S. Rowlinson, B. Widom *Molecular Theory of Capillarity* (Clarendon, Oxford, 1982).

[121] M.R. Wilson, M.P. Allen, M.A. Warren, A. Sauron, W. Smith, *J. Comput. Chem.* **18**, 478 (1997).

Appendix A

Chemical Potential Calculations

In general, the chemical potential of a particle A in the NVT ensemble can be split into a sum of its ideal(kinetic) and excess(configurational) parts [5]

$$\mu_A = \mu_A^{id}(\rho) + \mu_A^{ex} \tag{A.1}$$

The density dependent ideal part can calculated analytically,

$$\mu_A^{id}(\rho) = -k_B T \, ln\frac{V}{(n+1)\Lambda^3} \tag{A.2}$$

Λ being the thermal de Broglie wavelength. The excess part is usually estimated using the classic Widom particle insertion method [6, 56],

$$\mu_A^{ex} = -k_B T \, ln\left\langle \exp\left[-\frac{U_A^*}{k_B T}\right]\right\rangle \tag{A.3}$$

where U_A^* is the energy associated with inserting a test particle into the system. In practice Λ is usually assumed to be equal to one, and n to be large, so that the ideal part is given by $k_B T \ ln(\rho)$. When added to the excess part this gives the reduced chemical potential

$$\mu_A^r = k_B T \ ln(\rho) - k_B T \ ln \left\langle \exp\left[-\frac{U_A^*}{k_B T}\right] \right\rangle \qquad (A.4)$$

which is usually quoted in computer simulation studies.

The reduced chemical potential of a particle in the Gibbs ensemble can be calculated using a minor modification of the Widom expression [116], being

$$\mu_A^r = -k_B T \ ln \left\langle \frac{V_1}{n_1 + 1} exp\left[-\frac{U_1^*}{k_B T}\right] \right\rangle_{box\ 1} . \qquad (A.5)$$

where V_1 and n_1 are the volume and number of particles of type A, respectively, in the box of interest. This still incorporates ideal(kinetic) and excess(configurational) contributions as in the Widom expression for the NVT ensemble, only the Gibbs expression takes account of fluctuations in the volume and number of particles, and is only identical to the NVT version when these are negligible and the number of particles is large.

As well as particle insertion, it is also theoretically possible to calculate the chemical potential by particle deletion, using an analogous equation,

$$\mu = \mu_A^{id}(\rho) + k_B T \; ln \left\langle \exp\left[+\frac{U_A^*}{k_B T}\right]\right\rangle \qquad (A.6)$$

where U_A^* is now the energy associated with removing a particle from the system. However, in practice this method does not not work particularly well, since significant contributions to the average, arising from configurations which involve particle overlap, are not sampled effectively [6]. This is because the deletion move involves removing a test particle from an already relaxed equilibrium distribution where significant overlaps are highly unlikely.

The difference in the excess chemical potentials of two species can be calculated using test moves which involve a change in identity of a particle [6, 117], the energy difference upon this change, U_{AB}^*, being used in the analogous equation

$$\Delta\mu_{AB}^{ex} = \mu_B^{ex} - \mu_A^{ex} = -k_B T \; ln \left\langle \frac{N^A}{N^B + 1} exp \left[-\frac{U_{AB}^*}{k_B T}\right]\right\rangle_{box1}. \qquad (A.7)$$

This can obviously be done by converting either species A into B, or B into A, which gives two different methods for calculating this difference (ie contraction and inflation respectively, assuming species A is bigger than B). Simply by inverting the two species types in the above equation, the following corollary is obtained

$$\Delta\mu_{AB}^{ex} = -\Delta\mu_{BA}^{ex}. \qquad (A.8)$$

Therefore calculations of the chemical potential using both inflation and contraction

trial moves should yield equal and opposite results. However, this was not observed in chapter 4.

To investigate this chemical potential behaviour, a series of simulations have been performed on the 50:50 mixture considered in Chapter 4, using simple NVT-MC at the same pressure, $P^* = 1.0$, and in the temperature range $10.0 \geq T^* \geq 1.0$. Relatively short runs (10,000 MC sweeps) were used, the system observables equilibrating after only a few hundred timesteps. During the latter half of each run, test particle insertions were made of both species, to calculate μ_i^r (long particles) and μ_j^r (short particles), as well as trial inflations and deflations, to measure the difference between the reduced values via Eqn A.7. As shown in Fig A.1, although
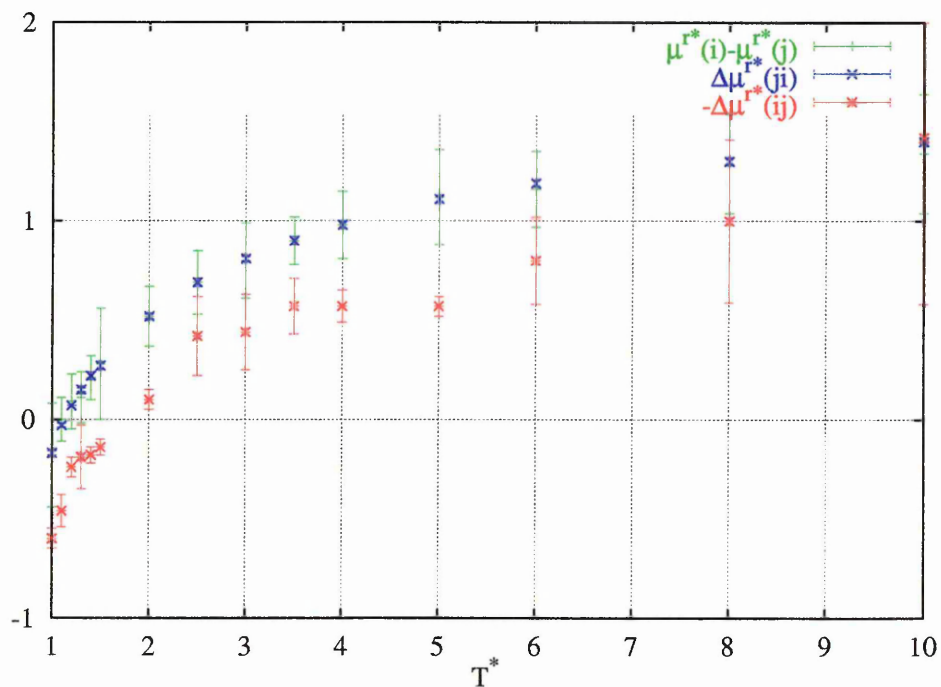

Figure A.1: Chemical potential values.

the identity change moves involving changing species j to i (inflation) gave values for the chemical potential difference in excellent agreement with that obtained from

204

the two insertion moves, the reverse (deflation) move systematically underestimated the value by around 0.5. Only at higher temperatures was better agreement seen, though we note that this is a significant temperature away from that at which the isotropic nematic simulations were performed.

It is concluded that the deflation moves result in an erroneous estimate for similar reasons to those that cause particle deletion to be inefficient in calculating the reduced chemical potential for one species, μ^r - the initial states considered do not sample configurations with a significant degree of overlap. Such configurations imply high initial energy, which after contraction would decrease quite significantly and lead to large negative U_{AB}^*, which would make a significant contribution to the average in Eqn A.7. This would result in a higher value for the logarithm, which, in turn, would yield a more negative $\Delta\mu_{ij}^r$, in better agreement with the other points on the graph from $\Delta\mu_{ji}^{ex}$ and $\mu_i^r - \mu_j^r$. We consider that this effect accounts for the inconsistency in the chemical potential differences as measured in chapter 4, and that, therefore, the values resulting from inflation moves are the correct ones.

Finally, it should be noted from Fig A.1, that the difference becomes negative as the density is increased. This suggests, rather counter-intuitively, that at high enough densities particle inflation leads to an overall gain in attractive energy, despite the increased risk of overlap. It is proposed that at these densities the local orientational order is sufficient that the risk of overlap upon such a modest inflation (2 to 2.5 in length) is out-weighed by the gain in attractive energy in the parallel interactions. This suggestion is made more plausible when it is remembered that inflation only occurs along the length of the molecule, and the width remains the same, mean-

ing the only overlap that can occur upon inflation is at the ends of the molecule. Furthermore, the attractive well-depth for two 2.5 : 1 particles in the side-side configuration is 1.36 times that for a 2 : 1 and a 2.5 : 1. This figure is arrived at by taking into account ϵ_{ii}, ϵ_{ij}, and the difference in strength of the side-side interaction relative to the cross well-depth reference for both particle pairs.

A.1 Summary

The inconsistency in the chemical potential difference calculation in chapter 4 has been shown not to be due to poor equilibration at the isotropic-nematic transition, but rather a problem with the algorithm used to calculate this difference using particle contractions. A systematic error of approximately 0.5 in these values is seen here, and this is consistent with the values reported in chapter 4. It has also been demonstrated that the negative values observed for particle inflation are not incorrect as would intuitively be expected, but due to the attractive interactions gained upon inflation and part of a definite trend seen upon cooling from high temperatures.